The Dissertation Committee for Joseph Michael Imhof Certifies that this is the approved version of the following dissertation:

Employing Near-field Scanning Optical Microscopy (NSOM) as a Tool for Interrogating a New Conjugated Polymer Material, Di-Dodecyl Poly(Phenylene Ethynylene)

Committee:

David A. Vanden Bout, Supervisor

Stephen E. Webber

Keith J. Stevenson

Jason B. Shear

Ananth J. Dodabalapur

Employing Near-field Scanning Optical Microscopy (NSOM) as a Tool for Interrogating a New Conjugated Polymer Material, Di-Dodecyl Poly(Phenylene Ethynylene)

by

Joseph Michael Imhof, B. S.

Dissertation

Presented to the Faculty of the Graduate School of

The University of Texas at Austin

in Partial Fulfillment

of the Requirements

for the Degree of

Doctor of Philosophy

The University of Texas at Austin

August, 2004

Dedication

For Mark D. Morrow.

A kind man who has always taken an active role in my education. He made me see that a man's life is measured by more than the money he makes or the things that he owns. It is measured by the things that he reads, the places where he travels, and by the people that he cares for.

Thanks, Dad

Acknowledgements

This work is the literal culmination of decades of school and the work of numerous people to provide me with the support and environment necessary to thrive academically. First of all, I wish to thank the two strongest female personalities in my life. Without the support of my mother and my wife I would not have made it to graduate school nor stuck around to complete it. Thank you, Lynn and LeLe, for you reassurance, confidence, and unconditional love. To my Grandmother, Mrs. Patricia Imhof, I also extend infinite gratitude for both financial and spiritual support. Her faith in both God and Catholic education enabled me opportunities to grow as a student and as a person. My grandparents, George and Eva Elliott, should also be thanked for always supporting my academic progress and having faith that I could always succeed. To my sister, Molly Morrow, I extend a thank you for always being my biggest fan and for showing me why people draw, write, paint, and dance. I am further indebted to my graduate mentor, Dr. David A. Vanden Bout, for keeping me focused during frustrating times in my graduate career and providing an excellent role model- he showed me that you can be a great scientist and a genuinely nice guy. Along with acknowledging all of the current and past members of the Vanden Bout research group, I would like to especially thank Laura Deschenes and Eun-Soo Kwak for friendship and guidance in the laboratory. I also want to express my thanks to Bird and Alice for allowing me to marry their youngest daughter and also for adopting me as their northern mascot. In conclusion, I want to thank the Jesuit Order for providing me a superior undergraduate education concerning chemistry, philosophy, humanity, and college basketball.

Employing Near-field Scanning Optical Microscopy (NSOM) as a Tool for Interrogating a New Conjugated Polymer Material, Di-Dodecyl Poly(Phenylene Ethynylene)

Publication No._____

Joseph Michael Imhof, Ph. D.

The University of Texas at Austin, 2004

Supervisor: David A. Vanden Bout

A variety of optical and scanning probe techniques have been employed to gain understanding concerning the chemical species responsible for light emission in condensed phase films of di-dodecyl poly(phenylene ethynylene) (DPPE) thin films. Thermal treatment of DPPE has been found to substantially change polymer film morphology even at temperatures below the polymer glass transition (Tg). Significant changes in sample fluorescence accompany these changes in morphology. Polarization near-field scanning optical microscopy (NSOM) has been used to make quantitative measurements of polymer film order within films having undergone various thermal processing histories. Fluorescence signatures from these films follow a trend from low-energy excimer-dominated emission in disordered films to a singlet dominated exciton emission as polymer order increases. This trend has been attributed to the breaking of polymer close-associations in a high-energy glass under thermal relaxation.

Fluorescence quenching at a polymer/metal interface has been measured using fluorescence lifetime imaging (FLI) NSOM. Results indicate that nonradiative excited state quenching occurs over a very small distance scale. The technique prevents errors in measuring quenching associated with variations in total fluorescence intensity or scanning artifacts. Results indicate that fluorescence quenching may be consequential in sandwich type polymer thin films, but will have little effect on device efficiency in planar light emitting devices with line gaps on the scale of 1 micron.

Sandwich and planar devices were fabricated using DPPE. Measurements of electroluminescent spectra acquired from sandwich devices fabricated from pristine and annealed films of DPPE were compared. Electroluminescent spectra from the two sets of devices are similar, indicating that device light emission is mediated by the presence of excimer sites in both types of films. Two sets of devices with planar geometries were also fabricated using pristine and annealed DPPE films. In these samples direct high-resolution imaging of polymer light emission in fictional light emitting devices was achieved. Photoconductive response could be elicited in biased devices under conventional epi-illumination. These results were expanded to test the viability of making high-resolution measurements on planar gap devices using NSOM as a localized illumination source.

Standard samples for NSOM probe aperture characterization were fabricated using nanosphere lithography. Small, spatially dispersed perforations in a metal film have been used to calculate the size and shape of NSOM tip apertures. Transmission NSOM images are a convolution of the perforation being imaged, and the NSOM instrument response function. By deconvolving the size of the perforation from the image, it is possible to calculate the size and shape of the NSOM tip aperture.

Table of Contents

List of Figures

Chapter 1: Dissertation Overview

INTRODUCTION

The current research has focused on the characterization of a new conjugated polymer material, di-dodecyl poly(phenylene ethynylene) (DPPE). Specifically, issues concerning photoluminescence, electroluminescence, and the correlation between sample spectroscopy and physical morphology have been addressed in detail. Varying degrees of order within thin film samples have been induced via thermal processing routes. Significant polymer chain ordering is especially pronounced in thermally annealed thin film samples. Correlations between polymer film morphology and spectroscopic behavior have been explored using bulk conventional far field spectroscopic methods as well as high-resolution atomic force microscopy (AFM) and near-field scanning optical microscopy (NSOM) scanning probe techniques. NSOM has also been employed to examine fluorescence quenching behavior near a conductive metal interface with high spatial resolution. This interface was chosen as a means of modeling the polymer/electrode interfaces often found in polymer thin film optoelectronic devices. Detailed studies examining thermally processed condensed phase films in organic light emitting device applications, as well as in other model devices used to investigate film photoconductivity properties have also been completed. Finally, standard samples fabricated in-house have been employed to characterize the size and shape of NSOM tip apertures used in high-resolution imaging.

CHAPTER 2: CONJUGATED POLYMERS

Chapter 2 provides an overview of conjugated polymer materials in general. Background information concerning basic polymer semiconductor functionality, and the processing advantages that make these systems attractive in technological optoelectronic device applications are presented. Experimental issues still needing attention and complications preventing wide-scale conjugated polymer technological implementation are also discussed. In particular, high-resolution optical interrogation is proposed as a method for characterizing small-scale photophysical activity. Recent work in the literature examining correlations between sample morphology and thin-film optical properties is presented along with a general description of spectroscopic terms needed to describe important molecular species found within conjugated systems. The common excited state species responsible for the unique spectral behavior of conjugated systems are particularly highlighted and described using molecular terminology. Current controversies found in the literature surrounding the photophysical behavior of processed conjugated polymer films is also briefly presented before finally discussing the specifics of DPPE. The remainder of the current work will focus on this one conjugated polymer system.

CHAPTER 3: NEAR-FIELD SCANNING OPTICAL MICROSCOPY (NSOM) AS A TOOL FOR INVESTIGATING ORGANIC THIN FILMS

Chapter 3 discusses both the advantages and limitations associated with conventional optical microscopy. Specifically, the boundaries of optical resolution using conventional wave optics will be addressed. Both the analytical advantages and the practical drawbacks of other high-resolution non-optical

analytical techniques are described in terms of their application to organic thin film analysis before presenting a theoretical description of optical imaging beyond the diffraction limit. An introduction to modern NSOM is presented, and the practical elements typical to common NSOM experiments are described in detail. NSOM probe fabrication is outlined, as well as the practical scanning considerations surrounding the most commonly adapted NSOM methods used in our laboratory.

CHAPTER 4: BULK FLUORESCENCE CHARACTERIZATION OF DI-DODECYL POLY(PHENYLENE ETHYNYLENE) THIN FILMS UNDER THERMAL PROCESSING

With the use of an experimental polymer system in most of our work, it is of paramount importance to independently characterize the spectroscopy and physical characteristics of the new polymer. An investigation into polymer film ordering and effective processing routes used for sample preparation is also required. In Chapter 4, the results of bulk measurements of both sample absorption and fluorescence emission are presented from experiments conducted on separate thin-film and solution phase samples. Relationships between solution concentration and spectroscopic response are identified and confirmed with the available literature. Film studies are further used to uncover new information regarding the spectral evolution of the organic materials in condensed phase films with changes in thermal processing history. Conventional polarization optical microscopy is employed to examine films of DPPE, as the films rearrange substantially under thermal and solvent vapor annealing to create heterogeneous environments of well ordered polymer macromolecules. Accompanying the

morphological change, is witnessed a drastic spectral evolution from a system demonstrating low-energy emissive character to a blue-shifted fluorescence signature. The fluorescence behavior of DPPE pristine films indicate the presence of strong intermolecular interactions and exhibit responses indicative of excimer-type wavefunction associations. Thermally annealed samples, however, display steady state fluorescence properties and short lived fluorescence lifetimes typically associated with ground state aggregate species formation.

CHAPTER 5: ATOMIC FORCE MICROSCOPY (AFM) AND NEAR-FIELD SCANNING OPTICAL MICROSCOPY (NSOM) CHARACTERIZATION OF DI-DODECYL POLY(PHENYLENE ETHYNYLENE) THIN FILMS

In Chapter 5, AFM and NSOM methods are used to characterize film surface morphology and uncover continuing trends associating sample fluorescence behavior and molecular order within organic thin-film samples of DPPE. A basic description of contact mode AFM is followed by a presentation of data collected from films with varied thermal processing histories. Polarization NSOM is also described in detail and the theory behind fluorescence anisotropy measurements and the ability to make quantitative statements concerning film order are presented. Polarization NSOM is then extended to acquire high-resolution optical images of the same processed films examined using AFM. Since spatial averaging still occurs on the distance scales probed by NSOM, a simple simulation is also described in which the instrument response function can be accounted for in NSOM measurements and a more complete picture of polymer chain alignment within the thin films can be provided. By coupling results acquired in Chapters 4 with those from Chapter 5, it is possible to state

definitively that molecular relaxation within the glassy polymer system leads to a reduction in excimer type fluorescence behavior, and to a concomitant increase in overall aggregate emission and long range order.

CHAPTER 6: FLUORESCENCE LIFETIME IMAGING NSOM TO EXAMINE DI-DODECYL POLY(PHENYLENE ETHYNYLENE) QUENCHING NEAR A CONDUCTIVE METAL BOUNDARY

The coupling of time-correlated single-photon counting (TCSPC) with NSOM is employed to obtain fluorescence lifetime information at every pixel during high resolution near-field imaging. The resultant technique, fluorescence lifetime imaging (FLI)-NSOM is introduced and explained in Chapter 6. The adaptation of the technique to probe fluorescence quenching near a metal interface is also detailed. The method demonstrates, not surprisingly, that fluorescence quenching takes place over a very small distance scale. Quenching is observed to occur on a distance scale less than that which is resolvable, even with our current near-field technique, in conjugated polymer films of DPPE. The lack of nonradiative quenching over large distance scales provides encouraging evidence that electroluminescence from small line-gap planar electrode devices (examined in Chapter 7) will not suffer significant quenching, and that meaningful measurements can be made on prototype planar model light emitting devices (LEDs).

CHAPTER 7: OPTOELECTRONIC DEVICES FABRICATED USING DI-DODECYL POLY(PHENYLENE ETHYNYLENE) ACTIVE LAYERS

Chapter 7 presents data acquired from in-house fabricated conjugated polymer optoelectronic devices. Simple three-layer sandwich devices were

fabricated to obtain electroluminescent signatures of organic LEDs. Both pristine and annealed films of DPPE were employed as active recombination layers in separate sets of devices. Fabrication of micro-scale planar metal-polymer-metal junction devices is also accomplished so that high resolution optical analysis can be used to probe localized photoconductivity and charge transfer efficiencies in ordered thin films of DPPE. The planar devices are also employed under high bias and in a evacuated, low-temperature environment to directly examine localized DPPE electroluminescence. Photolithographic and focused ion beam milling techniques employed for the production of these microscale planar devices are detailed as well. Bulk measurements of photoconductivity from DPPE devices are collected and comparisons between disordered spin cast films and ordered annealed samples are made. Specifically, polarization studies examining planar device electroluminescence are conducted to search for correlations between polymer chain alignment and electroluminescent efficiency. Unfortunately it has proven difficult to identify definitive connections between polymer alignment and electroluminescent efficiency as the devices often prove dynamic/unstable in their light emitting character. The planar devices are also employed to examine spatial differences in electroluminescent behavior with reversals in device polarity and measure hysterisis effects caused by high operating fields within the small-gap polymer devices. In these studies, it has been possible to measure asymmetric I-V relations in electrically cycled devices and with exceptional optical resolution identify asymmetry associated with light emission from the DPPE in the interelectrode gap.

CHAPTER 8: STANDARD SAMPLE CHARACTERIZATION OF NEAR-FIELD SCANNING OPTICAL MICROSCOPY (NSOM) PROBE APERTURES

Chapter 8 is a stand alone section of the dissertation. Work unrelated to conjugated polymers is presented demonstrating the use of in-house fabricated metal standard sample films for inexpensive, straight forward NSOM probe aperture characterization. Direct measurement of probe aperture sizes via high resolution scanning electron microscopy was accomplished and compared with data acquired from transmission NSOM scans of nanoperforated metal standard samples. Reasonable agreement between the sets of measurements indicate the ability to accurately quantify tip aperture diameters above 90 nm using the standard sample. This method also offers a convenient means of identifying sub-diffraction limited probes useful for effective near-field imaging and further data simulations.

Chapter 2: Conjugated Polymers

CHAPTER SUMMARY

Basic background concerning conjugated polymer materials is presented. The principles behind conjugated polymer semiconduction are described and the advantages that these polymer materials exercise over inorganic semiconductors are also presented. New technological device applications employing organic polymer film active layers are briefly described, as well as the practical drawbacks that have slowed organic device development. This chapter will examine fundamental scientific questions that have frustrated the conjugated polymer community, focusing on the link between different polymer processing techniques, organic thin film morphology, and sample spectroscopic behavior. This discussion will utilize molecular spectroscopy to explain the various spectroscopic signatures and roles of interchain species. A number of experiments examining conjugated polymers, in general, are chronicled before looking in detail at di-dodecyl(poly phenylene ethynylene) (DPPE), the specific polymer material to be employed for the rest of the current work. High resolution optical interrogation is proposed as a method for further development of a sound understanding concerning small-scale conjugated polymer photophysical activity.

INTRODUCTION

Conjugated polymers are of current scientific interest as these materials present great promise in new technological device applications.[1-14] Their recent exposure in the literature stems from the repeated demonstration that these novel

systems can be made to function similarly to direct band gap molecular semiconductors. These polymer materials present a seemingly perfect situation where the functional attributes of both polymer and semiconductor materials are unified in a single, easily processed system. The optical and electronic properties that have been so well exploited to make advances involving inorganic semiconductor technologies, are coupled with the numerous processing advantages common to organic polymers in conjugated polymer media. Condensed phase processing of thin films from organic solution has proven especially powerful in the production of large area, light weight thin film optoelectronics.[11-13,15,16]

Although conjugated materials present a unique avenue by which thin film semiconductor devices can be fabricated; and extensive empirical studies have greatly enhanced the state of the art concerning overall device fabrication, a number of major scientific questions remain unanswered. These issues have hindered technological progress of commercial systems.

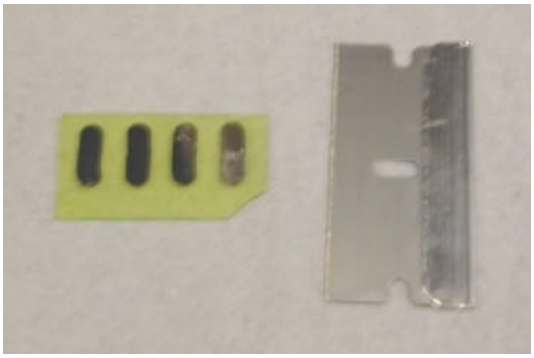

Figure 2.1 Four thin-film LEDs fabricated using ITO coated glass as a device substrate and a 70 nm thick film of spin deposited di-dodecyl poly(phenylene ethynylene) (DPPE) as the device active layer. The sandwich structure is completed using vapor deposited aluminum as a cathode material. The four devices share the same ITO cathode material but possess independent aluminum cathodes.

In particular, much of the fundamental photophysics responsible for light emission and carrier transport in the conjugated materials remains poorly understood. Basic issues also remain unresolved concerning the most efficient processing routes and the extent and types of molecular interactions necessary in these organic systems to promote efficient optoelectronic device operation. A number of interesting studies have been conducted in order to clarify these questions in different conjugated polymer systems.[17-23]

CONJUGATED POLYMER FUNCTIONALITY

In the late 1970s it was discovered that doped polymeric materials could be used to carry charge in much the same way as other conductive media[24]. Until this point, the resistivity of polymers had always been found to be extremely high, and they were routinely classified as insulators. Highly conductive doped acetylene samples, however, changed the general way in which polymers were

perceived by providing strong preliminary evidence that new classes of materials could be synthesized that combined electrical conductivity with the numerous processing benefits associated with plastics. A number of polymeric media were synthesized over the next decade exhibiting varying degrees of electrical conductivity.[25] Rapid progress in the areas of both conductive polymer synthesis and concerning the photophysical characterization of these new materials was made within a rather short time window. These developments quickly led to the design and synthesis of materials with enhanced solubilities in organic solvents and a wide variety of other optical and electrical properties.[22,26-28]

Conjugated polymers are one class of unique organic molecules demonstrating interesting optical and electronic properties. In order for a material to be useful as an active component in a device (and not just a wire or interconnect), it is necessary for it to possess semiconductor character. Conjugated polymers provide access to this valuable semiconducting behavior. The polymer materials exhibit a classic nonlinear current response with an increase in an externally applied electric field.[6,9,29,30] As an added feature of these conjugated molecules, many of the polymers possess excited state species that emit efficiently in the visible portion of the spectrum upon radiative relaxation. The electrical and spectral signatures of these polymer materials are both capitalized upon to produce functional optoelectronic devices. In the course of only a few years following their discovery, important practical developments coming in the form of functional LEDs were fully realized.[31] The semiconducting

nature of the polymer films were also extended into other applications concerning prototype thin film transistors and other photoconductive device elements.[2, 14, 32-35]

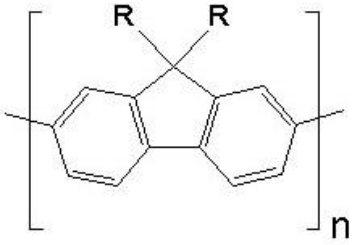

Poly(fluorenes)

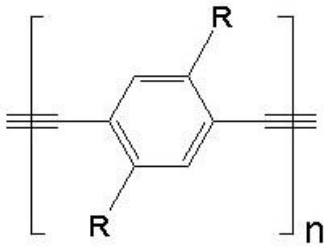

Poly(phenylene ethynylenes)

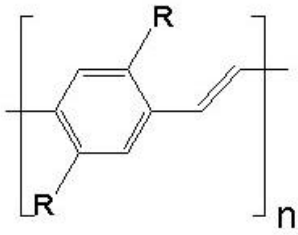

Poly(phenylene vinylenes)

Figure 2.2 Examples of conjugated polymer systems. Electron delocalization along the length of the conjugated pi systems are possible through the alternating pi bonds.

Initial device power efficiencies remained low, however, and spurred further empirical research.[12,31,33,36,37] As device efficiency was enhanced, the materials were employed in devices ranging from simple diodes and transistors to more complex light emitting displays and photo sensors. Because of the vast array of new and current technologies where active semiconductor elements are

needed, conjugated semiconducting polymer systems have emerged as an area of intense scientific focus.

PRINCIPLES OF BASIC SEMICONDUCTION

The phenomenon of semiconduction is most easily described by borrowing the principles and terminology of inorganic solid state physics. In a periodic system of interacting atoms, the overlap of individual atomic orbitals results in the presence of a delocalized band structure. The formation of these bands result in high electron densities at certain allowable band energies (related to the energy of the noninteracting atomic orbitals). When an energy separation occurs between bands it is defined as the material band gap. Within condensed phase crystalline materials there are three basic states based upon the electrical conductivity that a substance can adopt. In order to discuss this dependence, it is necessary to define two terms: the valence band, and the conduction band. The valence band is defined as the energy band resulting from the overlap of individual molecular orbitals filled with valence electrons to form a periodic lattice. In a system comprised of atoms with full outer valence shells, this band will be completely filled (Figure 2.3 right). The conduction band is similarly defined as the overlapping atomic orbitals in a periodic lattice located at higher energies than those of the valence band. The classification of the material depends entirely upon the band gap associated with electronic transitions between the valence and conduction bands of the material. In general, substances are characterized by the magnitude of the band gap, which relates directly to the ability of the material to conduct electricity. When a large gap exists (>3eV), the

material can be classically described as an insulating substance. If the gap is fairly small (typically <3 eV), the conduction band can often be populated by thermally excited electrons and the material is classified as a semiconductor since electrons can be easily promoted to the conduction band. In a third case, where a material possesses a partially filled valence band, the electron sea description is most applicable. In this situation, electrons have numerous available routes for conduction throughout the material and the unfilled energy band (Figure 2.3 left). This situation results in the classical definition of an electrical conductor; having essentially no band gap or other barrier to charge carrier mobility.[38]

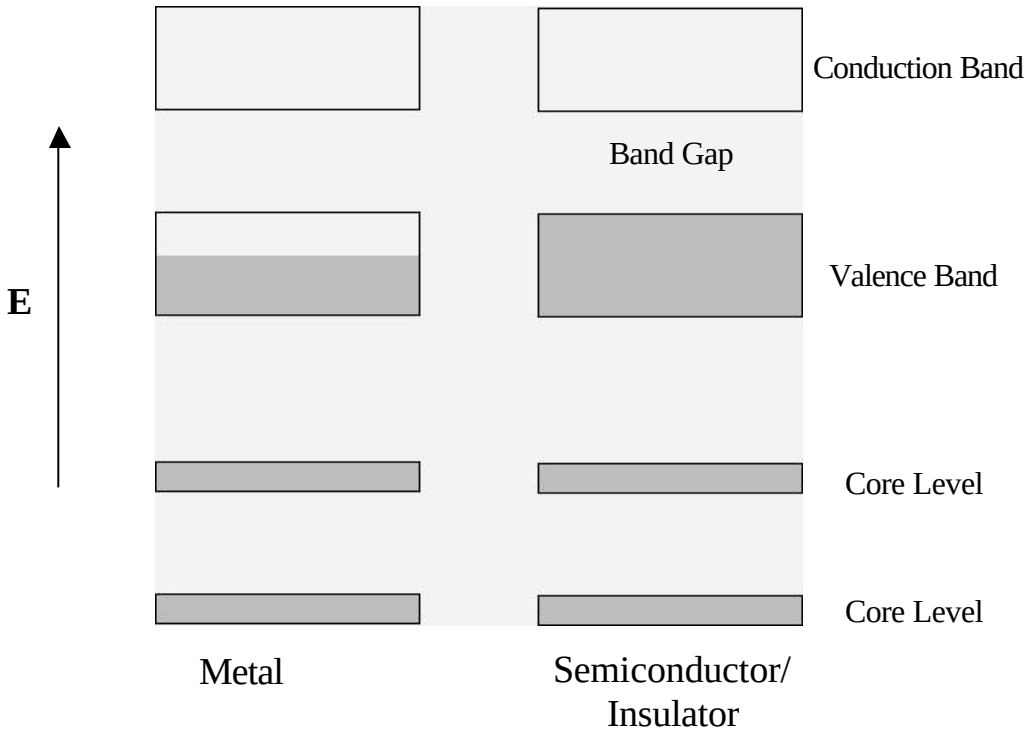

Figure 2.3 Schematic representation of metals and nonmetals using band theory. A partially filled valence band is represented in the case of the metal and a band gap between the valence and conduction band is illustrated for the semiconductor/insulator example.

Since individual polymer molecules are fairly dissimilar to a periodic inorganic lattice, semiconduction in molecular systems must be approached from a slightly different vantage.[39] However, the materials can still be described employing the same general principles. The electrical activity and unique optoelectronic properties of organic conjugated polymer semiconductors can be attributed to their planar macromolecular structure.[8,40,41] These ladder-type, rigid rod polymers possess unique molecular systems of overlapping p-orbitals. The extended pi systems created through the overlapping molecular orbitals from

constituent aromatic rings and properly oriented pi bonds results in the formation of a delocalized pi electron cloud along the rigid polymer backbone. The resulting, extended orbitals create an energetic situation strongly analogous to the typical band description used to explain carrier transport in conventional inorganic semiconductors. The conjugation length is usually accepted as 7-10 monomer units in length- far from a large periodic lattice system.[42]

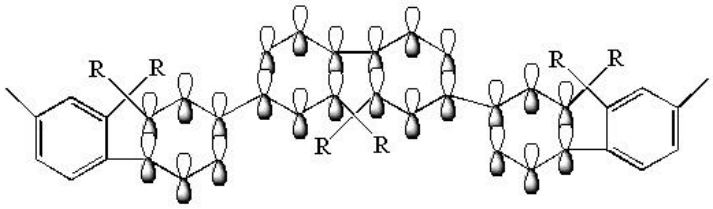

Figure 2.4 Schematic of conjugated p-orbital overlap and electron delocalization illustrated along a dialkyl poly(fluorene) polymer backbone.

The highest occupied and the lowest unoccupied molecular orbitals (HOMO and LUMO) of the linear organic molecules mimic the valence and conduction bands of their more traditional inorganic counterparts. Because of the small bandgap associated with the polymer, the rigid rod structure yields a one dimensional molecular system conducive to semiconduction along the length of the polymer backbone. When a series of these rigid polymers are packed together in a closely associated condensed phase film environment, semiconduction can also be induced in multiple dimensions through increased inter and intra molecular interactions.[21,43-45]

THE POLYMER ADVANTAGE

The intensity with which advances in conjugated polymer materials have been pursued is directly correlated to their projected impact on industry and commerce. Conjugated polymers have become much more prevalent in the literature, in part because of the advantages that they can offer over their inorganic cousins. A number of the phenomena that lead to the diverse optoelectronic properties found in conjugated polymer materials also result in the reduction of overall semiconductor device production costs, thus creating substantial industrial demand for the new materials in the high volume, high dollar semiconductor sector.[46]

Perhaps the single greatest advantage offered by organic semiconductors over single crystal inorganics lies in the fact that the materials need not adopt a stringent crystalline packing structure in order to achieve semiconductor functionality. The typical requirement that inorganic semiconductors be rigorously crystalline and lacking of structural/molecular defect sites to operate effectively, ultimately results in increased production costs. In common p- and n-doped inorganic semiconductor samples, crystal growth methods are further complicated as it becomes necessary to maintain uniform dopant concentrations and produce the dopant boundary junctions that prove vital for many diode applications.[38] Since the probability that a defect will occur increases substantially with increased crystal dimensions, inorganic approaches often become prohibitive in large area semiconductor applications as costs increases exponentially with overall crystal size.[38] High temperatures are also required for

inorganic crystal growth processing so basic energy requirements become quite expensive with increases in the fabrication scale as well.[30] Conjugated polymers, on the other hand, demonstrate varying degrees of semiconduction depending upon overall structure and variations in local chemical environment.[47] Although impurities do indeed remain a consideration with these organic systems, the materials are not vitally dependent upon periodic intermolecular ordering, as periodicity is always maintained by the alternating intramolecular covalent linkages. Charge transfer phenomena and photoluminescent behavior can be measured in a vast array of samples ranging from bulk solutions to single molecule preparations and even in large area condensed phase films.[47-50] From a practical standpoint, solid conjugated polymer thin films are more important than their solution phase couterparts as films possess greater utility in practical device fabrication. Film morphology and molecular order have been intimately linked to polymer luminescence and carrier transport activity although direct measurements correlating electrical phenomena with surface morphology remain preliminary.[9,29,51,52] The eased restrictions on molecular geometry in conjugated polymer samples results in effective semiconduction over a wide array of sample conformations.[53-56]

Yet another benefit accessible when using polymer semiconductors is the ability to fabricate thin film plastic devices with considerably lighter weights than those produced from similar inorganic substrates. This tremendous weight advantage posed by plastic materials is especially attractive for increased device applications in aerospace, automotive, and personal electronics realms where

every ounce of device weight is of utmost importance in maintaining fuel economy and portable convenience. Efficient optoelectronics can be produced with polymer active layers of only a few tens of nanometers in thickness. Light-weight conductive substrates and thin metal electrodes also help reduce the weight considerations of polymer optoelectronics. The production of thinner and lighter organic flat panel light-emitting displays and portable polymer active layer solar cells are quickly becoming a technological reality.[27]

Mechanical flexibility is yet another area in which conjugated polymers far out perform brittle inorganic semiconductors. Flexibility is an issue that cannot be adequately addressed when considering traditional lattice-type semiconductors. The structural rigidity required for inorganic materials to function makes devices from these substances prone to cracking along defect boundaries and prevents any appreciable bending or rolling.[38] The plasticity of high polymer films, however, provides an avenue by which whole new classes of optoelectronic devices can be designed. Recent proposals envisioning light emitting displays that can be easily rolled up for transport as well as light weight portable solar collectors that could be unzipped and deployed under emergency conditions are both viable ideas when employing polymeric materials in conjunction with flexible electrode materials.[30]

The ability to dissolve conjugated polymer molecules in common organic solvents provides probably the most important fundamental processing advantage over inorganic semiconductors. As stated earlier, condensed phase films are technologically more interesting than solution phase samples as they can offer

convenient active layers in device applications. Polymer solutions, however, present the processing avenues by which large area panels as well as devices employing unique geometries can be successfully and efficiently produced.[30, 57, 58] Uniform homogeneous thin films can be made under ambient conditions via solution drop casting, spin casting, stamping, and ink jet printing techniques.[58] As opposed to high temperature inorganic crystal growth methods that possess relatively low likelyhoods of yielding usable large area semiconductor crystals, polymer solutions offer an opportunity to cast high surface area semiconductor films for use in optoelectronic panels.[30] Upper limits on device size subsequently become confined only by the dimensions of the electrode support structure employed during solution deposition. In this manner large scale semiconductor panels can be envisioned that could be employed in solar collection or in colorful self illuminating billboards. Ink jet and stamp printing deposition methods are especially attractive concerning low cost novelties such as luminescent business and greeting cards that can be stamped with a company logo or brand name. These items can be manufactured with a small battery and made to luminesce for a short promotional period.[59]

SIMPLE OPTOELECTRONIC DEVICES

Polymer LEDs are conceptually the simplest conjugated polymer devices and are typically constructed in a sandwich structure containing three basic layers. A transparent electrode, usually indium tin oxide (ITO), is initially deposited on a freestanding transparent substrate. A thin film of a conjugated polymer material is then deposited via spin casting from organic solution to create a uniform ~100

nm thick polymer active layer. To complete the sandwich structure, a second electrode is subsequently deposited in the form of a layer of a low work function metal layer via thermal vapor deposition. When a bias is placed across the polymer active layer, electrons are injected from the metal cathode and holes are injected from the ITO anode.[35,60] Upon recombination of these charge carriers within the polymer active layer, an excited state molecular species is created that, upon further radiative relaxation, emits a photon of light energetically identical to the gap between the HOMO and LUMO of the conjugated system.[60]

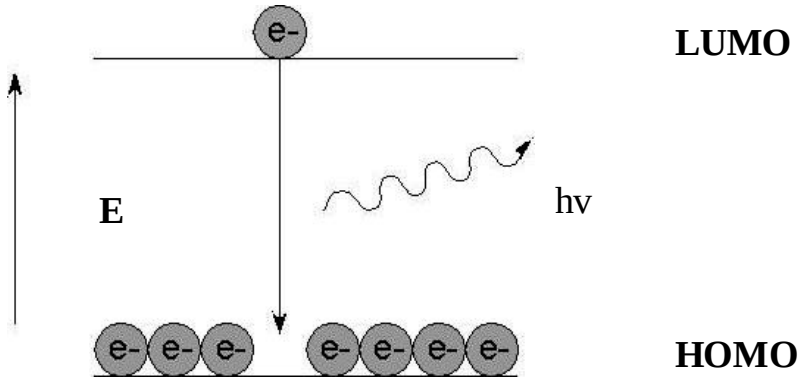

Figure 2.5 Electron and hole recombination in a molecular system. The resulting recombination results in radiative emission. Electrons are injected from the device cathode and holes are injected from the anode.

If, instead, the device is operated in the reverse manner, where photoexcitation of excited state polymer species occurs in the active layer, followed by efficient charge carrier separation, current can be made to flow. This is how the device can be made to function as a photodetector or solar panel. In order to have efficient transduction of light energy to electrical energy, however, it is important to have effective separation of the charge carriers created by

photoexcitation. Without charge separation, the excited state chromophore simply recombines and relaxes, often emitting a fluorescence photon, and resulting in no net current flow. For this reason, different device constructions are required to optimize either light emission or carrier separation.

Actual light emitting device structures usually possess five separate regions where other layers of electron and hole transporting polymers are introduced adjacent to the active semiconductor region. These extra carrier transporting layers are deposited to balance charge injection at the polymer interface and enhance luminescence.[30,57,61] Extra layers beyond the active polymer are also added to devices used in photovoltaics.[2] In this case, materials are used to efficiently sink the charge carriers produced in the excited state, promoting electron flow toward the cathode and hole migration in the direction of the device anode. Approaches employing polymer mixtures and heterogeneous composites have also been used to promote efficient charge separation.

PROBLEMS ASSOCIATED WITH CONJUGATED POLYMER DEVICES

Even with the numerous processing advantages, and the demonstrated ability to fabricate functional optoelectronic devices, conjugated polymer materials have not yet proven to be a holy grail in all semiconductor device applications.[60,62-64] Lifetime limitations and questions surrounding basic photophysical operation of these new materials have substantially hindered their wide scale industrial implementation. Problems with device burnout as well as spectral instability with film aging and environmental stress have caused significant reservations when considering these materials for long life consumer

product applications. Only recently have the materials been applied to products in the marketplace that require only short overall lifetimes such as cellular phone and electric shaver displays. Increased film degradation and loss of spectral stability at elevated temperatures and even under ambient light exposure have so far relegated the use of organic semiconductors to a limited industrial position. However, promises of cheap processing and inexpensive devices have driven industrial research to improve overall device efficiencies. Synthesis of numerous conjugated polymer derivatives coupled with extensive empirical work examining device luminescence has led to these advances. Basic electrochemical relationships have also been employed to identify efficient passive electrode materials.[2,21,30,65] Unfortunately, a number of basic photophysical issues remain to be addressed. Three fundamental questions still loom over work addressing the photophysical operation of conjugated polymer materials. Questions surrounding aspects of carrier transport,[26,32] controversy surrounding conditions that optimize electroluminescence,[6,7,19,29] and arguments about the importance of intermolecular interaction in both of these processes are all strong evidence suggesting that organic conjugated polymer chemical properties are far from being well understood.

THE LINK BETWEEN MORPHOLOGY AND SPECTROSCOPIC BEHAVIOR

Direct optical observation of conjugated polymer samples has revealed the strong impact that processing history makes on polymer emission and spectral response.[49, 57, 66] A wide variety of emitting species can be identified ranging from singlet exciton emission, witnessed in dilute polymer solutions, to strongly

associated intermolecular species in condensed phase films.[11,12,20,67-69] All of these different emitting states are characterized by unique fluorescence signatures.

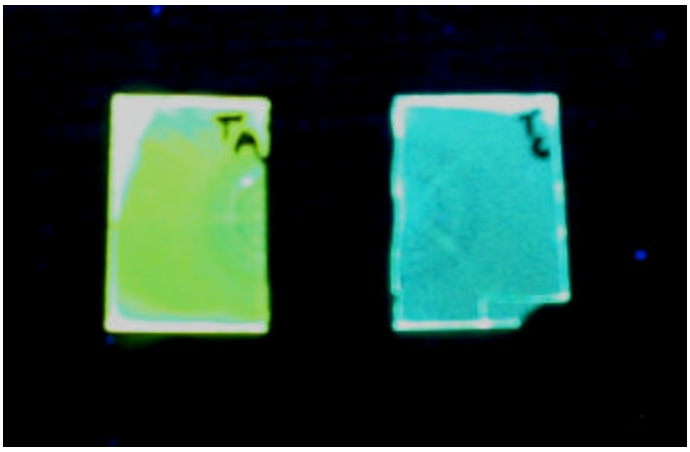

Figure 2.6 Bulk fluorescence witnessed from a pristine spin cast di-dodecyl poly(phenylene ethynylene) (DPPE) film and a film that has gone through a thermal annealing process (left).

Concerning the questions involving basic charge transport, conventional wisdom dictates that carrier transport in isolated one dimensional organic semiconductors should prove most efficient along the length of the delocalized pi system, and parallel to the direction of rigid polymer chain backbone alignment.[9,29,51,70] Since conjugated polymer systems are complicated and numerous interchain associations are present in solid films, arguments exist that this type of parallel transport may not necessarily always be the case in condensed phase polymer media. Arguments have been made citing strong interpolymer interaction as a viable option for enhanced conduction across the axis of aligned polymer chain backbones. This effect may be attributed to polymer chain straightening and the strong association of neighboring moieties, as confirmed by

spectral data indicating the substantial presence of intermolecular species. This type of perpendicular charge transport behavior has not, however, been characterized to date.

When addressing efficient electroluminescence from polymer semiconductor devices, the phenomenon has been thought to occur most efficiently when undergoing a simple radiative relaxation from an isolated singlet exciton species.[6,44,55,68,71] The relaxation of a singlet exciton involves no additional carrier transport and helps to improve efficiency by preventing non radiative losses due to aggregate formation and trapping to low energy defect sites in the polymer matrix. Certain samples have, however, demonstrated efficient electroluminescent behavior even while displaying spectroscopy typical of low energy aggregate formation.[72,73] The electrical properties of these aggregated systems have been shown to change dramatically with sample morphology, put trends have proven difficult to predict.[42,45,60,74]

THE ROLE OF INTERCHAIN SPECIES

The ability of conjugated polymers to exhibit strong semiconducting behavior without possessing a rigorously crystalline structure leads to a unique situation found only within these organic macromolecular materials. In contrast to traditional inorganic semiconductors or small molecule organics, material morphology becomes a fully adjustable parameter, allowing for processing control of the optoelectronic properties exhibited by polymer thin films. Overall processing history has an obvious and significant effect upon polymer film structure and causes the optoelectronic behavior of the films to change

dramatically. Solvent identity, spin casting conditions, thermal environment, and solution drying time all become important experimental parameters to control during conjugated polymer deposition from organic solvent.[35,45] Direct observation of films produced through varying film histories has lead to correlations between sample treatment, film morphology, and luminescent behavior.[21,60] As a result of these observations, numerous morphology/emission studies have been undertaken.[47]

A great deal of controversy has been generated concerning the functional role of interchain electronic species in these films and to what extent interchain moieties actively participate in both photo and electroluminescent processes. Nguyen et al. have presented a comprehensive review of the experimental measurements and common disagreements concerning interchain species in conjugated PPV systems over the past few years.[75] There are three main types of molecular species that need to be defined when discussing the spectral properties and the formation of excited state species in macromolecular conjugated systems.

In the conceptually most simple case, a singlet exciton state derives from the electronic excitation of a single molecule or isolated polymer chromophore unit. This excited state involves the simple promotion of an electron to a higher energy level in the isolated molecular system. Once excited, the species can relax either radiatively or through a non radiative route back to the electronic ground state. In solution, the excited state species typically undergoes a reorientation in the solvent environment and produces a characteristic Stoke's shift, leaving the emission red shifted from the initial absorption profile. When considering

conjugated systems of high polymers, the relaxation of the excited state unit is often through an efficient radiative pathway and is accompanied by characteristic emission in the visible portion of the spectrum.

In contrast to an isolated chromophore system, a group of molecules may have significant interchain associations within the ground state. The interaction of component dipoles in the ground state presents a situation where an aggregated species posses distinct absorption and emission signatures. An aggregated species often possesses a distinct absorption band from that of the chromophore in an isolated, non interacting environment. The formation of this new absorption band is typically nonlinear with concentration of fluorophore in the system. A classic example of this behavior is observed in the pseudoisocyanine dye family.[76] Following a photon absorption event, the excited state aggregate also has unique relaxation characteristics as compared with that of an isolated molecule and exhibits a distinct aggregate fluorescence emission. Depending upon the separation distance between constituent molecules and the orientation of the transition dipoles within the aggregate, either a pronounced narrow red or blue shifted emission can be observed. Aggregate species are also characterized by short lived fluorescence lifetimes and a non Beer's Law dependence upon sample absorption.

In a further complicated system, a third type of molecular species arises when chromophore molecules interact only in the excited state and not in the ground state. Unlike aggregate species, these hybrid systems do not posses a characteristic absorption. In this situation, an excited state singlet species

associates with a ground state molecule to create a bimolecular unit with a unique fluorescence emission. These excimer species do not possess a characteristic absorption because they only exist in the excited state, leaving the absorption spectrum of the system unchanged from that of the isolated chromophores. Their emission signature is unique, however. A broad, red-shifted emission is accompanied by a long fluorescence lifetime that resulting from the poor overlap of the excited state and ground state electronic wavefunctions of the excimer and the isolated molecules.[77]

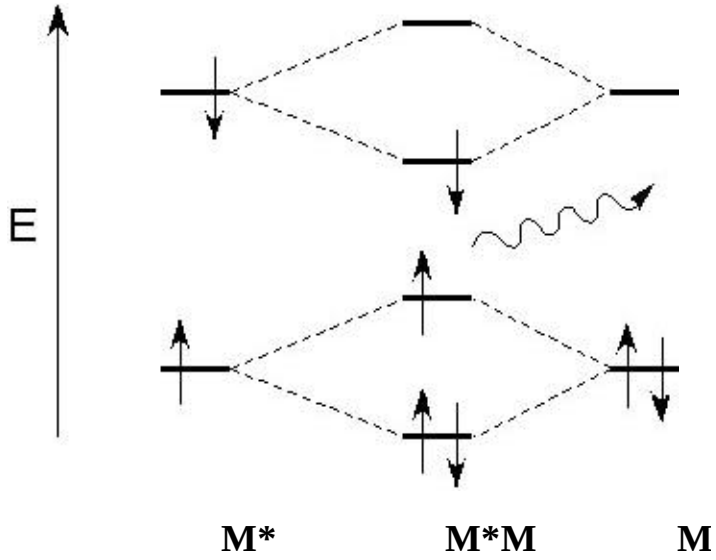

Figure 2.7 Schematic diagram demonstrating wavefunction overlap to yield excimer formation between an excited state molecule and a ground state species.

A broad structureless steady state emission band arises from the dissociative nature of the excimeric species as it relaxes back to the ground state.

A number of excimer species with a distribution of vibrational energies yields this broad signature. In a general case, the excited state species can be referred to as an exciplex. This term is used generally to describe a excimer-type species comprised of two different molecular units.

It is important to understand these three basic spectral entities, the characteristic spectroscopy of each, and the conditions under which they are likely to form. It is also of consequence to realize that in a complex system, such as that presented by a condensed phase polymer film, that none of these species will be found exclusively. It is much more likely, and well documented, that to describe condensed phase polymer photophysics one has to think in terms of distributions and an equilibrium involving a variety of interacting and isolated molecular systems. Indeed, it often proves advantageous to describe condensed phase polymers using terminology borrowed from solution phase spectroscopy and molecular concepts.

PREVIOUS CONJUGATED POLYMER STUDIES

A number of interesting studies have been undertaken in the hopes of making a concrete statement about conjugated polymer chain alignment in thin films and how it correlates to charge transfer, light emission, or intermolecular species formation. Due to the complexity of the polymer systems involved and the difficulties associated with comparing results from different experimental approaches, however, it has proven difficult to reach a consensus concerning the extent to which intermolecular species participate in polymer luminescence, or even to state clearly that charge carriers flow more efficiently in ordered polymer

systems than those which are isotropic.[9,21,51,60] Certain solution phase studies conducted on solvated conjugated polymer systems have indicated that well solvated solutions, upon spin deposition, increased intermolecular interaction as compared with solutions deposited from poorly solvated polymers.[9] Another examination yielded results indicating that interpolymer interaction increases with increased spin speed during spin deposition and that differences in spectroscopy could be attributed to chain straightening and enhanced conjugation length.[21]

A number of other studies have indicated that well ordered polymer systems lead to an increase in intermolecular species formation and often reveal a more excimeric spectral siganture.[48,49] Still, yet other work has been published indicating that the formation of excimer-like emission properties is simply the result of energy funneling to structural impurities and does not indicate interchain interaction at all.[61]

In still other sets of experiments, researchers have attempted to make measurements of net current flow and probe light emission efficiency in simple well aligned conjugated polymer thin film devices. The results of these experiments, however, have yielded little conclusive information concerning areas of enhanced photoconduction or light emission.[29]

SPECIFIC POLYMER MATERIALS

The group of studies found within the following chapters will focus on the characterization of solution and condensed phase samples of di-dodecyl poly(phenylene ethynylene) DPPE. This is a new material recently gaining attention as a blue-emitting conjugated polymer, with promise in further device

applications.[42,72,78] Methoxy ethyl hexyloxy poly(phenylene vinylene) MEH-PPV is yet another conjugated polymer material of specific interest in the following set of studies. Indeed much of the controversy mentioned in the above paragraphs surrounding conjugated polymer photophysics has focused on this specific polymer system or its related derivatives. MEH-PPV, however, was used mainly in the following work as a test of experimental methods. The polymer was used employed in the fabrication of preliminary optoelectronic devices as this material has been well studied in LED and other device applications. For this reason, in-house optoelectronic devices were first produced using MEH-PPV, with comparisons being made to available literature, before extending the methods/protocols to examine the other less studied conjugated system, DPPE.

HIGH RESOLUTION OPTICAL SPECTROSCOPY

The pronounced optical activity associated with conjugated polymer materials provides a unique analytical route by which to characterize these complex systems. Unfortunately, many of the processes responsible for light emission and charge transfer in these macromolecular systems occur on a distance scale beyond what is able to be resolved with conventional optical microscopy. Bulk measurements have yielded useful information concerning overall sample spectroscopy and morphology but have failed to provide information on the scale of optoelectronic activity in condensed phase samples or in functional LEDs. In the next chapter, near-field scanning optical microscopy (NSOM) will be discussed as a high resolution tool enabling the characterization of conjugated polymer films and the ability to profile sample films on distances scales

approaching 50 nm, or a scale approaching conjugated polymer optoelectronic activity.

CONCLUSION

Conjugated polymer photophysics is a complex area where many questions still remain unanswered. Fundamental issues regarding the photophysical processes responsible for effective light emission, efficient charge separation, and optimal optoelectronic device operation all remain unclear and prove to limit technological advances. Controversy has arisen relating to the amounts of interchain interaction present in thin film samples and the best routes by which to promote film morphologies efficient for light emission or other technologically important processes. The following body of work will seek to use high-resolution optical techniques to image and characterize DPPE emission while, at the same time, correlating these spectral properties with physical changes in polymer film morphology.

REFERENCES

1. Adams, D. M.; Kerimo, J.; Liu, C.-Y.; Bard, A. J.; Barbara, P. F. *J. Phys. Chem. B* **2000**, *104*, 6728.

2. Granstrom, M.; Petritsch, K.; Arias, A. C.; Lux, A.; Andersson, M. R.; Friend, R. H. *Nature (London)* **1998**, *395*, 257.

3. McNeill, J. D.; O'Connor, D. B.; Barbara, P. F. *J. Chem. Phys.* **2000**, *112*, 7811.

4. Liu, J.; Yijian, S.; Liping, M.; Yang, Y. *J. Appl. Phys.* **2000**, *88*, 605.

5. Martin, S. J.; Bradley, D. D. C.; Lane, P. A.; Mellor, H.; Burn, P. L. *Phys. Rev. B: Condens. Matter Mater. Phys.* **1999**, *59*, *15133*.

6. Choo, D. J.; Talai, A.; Lee, Y. K.; Jang, J.; Park, S. H.; Huh, G.; Yoo, K. H.; Lee, Y. J. *Thin Solid Films*, **2000**, *363*, 37.

7. Friend, R. H.; Gymer, R. W.; Holmes, A. B.; Burroughes, J. H.; Marks, R. N.; Taliani, C.; Bradley, D. D. C.; Dos Santos, D. A.; Bredas, J. L.; Logdlund, M.; Salaneck, W. R. *Nature (London)* **1999**, *397*, 121.

8. Brown, A. R.; Greenham, N. C.; Burroughes, J. H.; Bradley, D. D. C.; Friend, R. H.; Burn, P. L.; Kraft, A.; Holmes, A. B. *Chem. Phys. Lett.* **1992**, *200*, 46.

9. Yu, G.; Pei, Q.; Heeger, A. J. *Appl. Phys. Lett.* **1997**, *70*, 934.

10. Pschirer, N. G.; Miteva, T.; Evans, U; Roberst, R S.; Marshall, A. R.; Neher, D.; Myrick, M. L.; Bunz, U. H. F. *Chem. Mater.* **2001**, *13*, 2691.

11. Cao Y.; Yu G.; Heeger, A. J. *Adv. Mater.* **1998**, *10*, 917.

12. Greenham, N. C.; Moratti, S. C.; Bradley, D. D. C.; Friend, R. H.; Holmes, A. B. *Nature (London)* **1993**, *365*, 628.

13. Burroughes, J. H.; Bradley, D. D. C.; Brown, A. R.; Marks, R. N.; MacKay, K.; Friend, R. H.; Burns, P.L.; Holmes, A. B. *Nature (London)* **1990**, *347*, 539.

14. Friend, R. H. *Synthetic Metals* **1992**, *51*, 357.

15. Kim, J.; Swager, T. M. *Nature* **2001**, *411*, 1030.

16. Cleave, V.; Yahioglu, G.; Le Barney, P.; Friend, R. H.; Tessler, N. *Adv. Mater.* **1999**, *11*, 285.

17. Vacar, D.; Dogariu, A.; Heeger A. J. *Chem. Phys. Lett.* **1998**, *290*, 58.

18. Klimov, V. I.; McBranch, D. W.; Barashkov, N. N.; Ferraris, J. P. *Chem. Phys. Lett.* **1997**, *277*, 109.

19. Nguyen, T.-Q.; Martini, I. B.; Liu, J.; Schwartz, B. J. *J. Phys. Chem. B* **2000**, *104*, 237.

20. Greenham, N. C.; Samuel I. D. W.; Hayes, G. R.; Phillips, R. T.; Kessener, Y. A. R. R.; Moratti, S. C.; Holmes, A. B.; Friend, R. H. *Chem. Phys. Lett.* **1995**, *241*, 89.

21. Nguyen, T.-Q.; Kwong, R. C.; Thompson, M. E.; Schwartz, B. J. *Appl. Phys. Lett* **2000**, *76*, 2454.

22. Harrison, N.T.; Hayes, G. R; Phillips, R. T.; Friend, R. H. *Phys. Rev. Lett.* **1996**, *9*, 1881.

23. Nguyen, T.-C.; Schwartz, B. J.; Schaller, R. D.; Johnson, J. C.; Lee, L. F.; Haber, L. H.; Saykally, R. J. *J. Phys. Chem. B*, **2001**, *105*, 5153.

24. Chiang, C. K.; Fincher, C. R.; Park, Y. W.; Heeger, A. J.; Shirakawa, H.; Louis, E. J.; Gau, S. C.; MacDiramid, A. G. *Phys. Rev. Lett.* **1977**, *39*, 1098.

25. Kumar, D.; Sharma, R. C. *Eur. Polym. J.* **1998**, *34*, 1053.

26. Osterbacka, R., Genevicius, K.; Pivrikas; a.; Juska, G.; Arlauskas, K.; Kreouzis, T.; Bradley, D. D. C.; Stubb H. *Synthetic Metals* **2003**, *139*, 811.

27. Babel, A.; Jenekhe, S. A. *Macromolecules* **2003**, *36*, 7759.

28. Hoi-Sim Lee, N.; Chen, Z.-K.; Chua, S.-J.; Lai, Y.-H.; Huang, W. *Thin Solid Films* **2000**, *363*, 106.

29. Lemmer, U.; Vacar, D.; Moses, D.; Heeger, A. J.; Ohnishi, T.; Noguchi, T. *Appl. Phys. Lett*. **1996**, *21*, 3007.

30. Gross, M., Muller, D. C.; Nothofer, H. G.; Scherf, U.; Neher, D.; Brauchle; C.; Merrholz, K. *Nature (London)*, **2000**. *405*, 661.

31. Bradley, D.D.C. *Synthetic Metals* **1993**, *54*, 401.

32. Zhang, Y., Hu, Y.; Chen, J.; Zhou, Q.; Ma, D. *J. Phys. D: Appl. Phys* **2003**, 36, 2006.

33. Yu, G.; Zhang, C.; Heeger, A. J. *Appl. Phys. Lett.* **1994**, *64*, 1540.

34. Liu, M. S.; Jiang, X.; Herguth, P.; Jen, A. K.-Y. *Chem. Matter*. **2001**, *13*, 3820.

35. Liu, J.; Shi, Y.; Yang, Y. *Appl. Phys. Lett.* **2001**, 79, 578.

36. Vestweber, H.; Pommrtrhne, J.; Sander, R.; Mahrt, R. F.; Greiner, A.; Heitz.; Bassler, H. *Synthetic Metals* **1995**, *68*, 263.

37. Granstrom, M.; Berggren, M.; Inganas, O. *Science* **1995**, *267*, 1479.

38. Singh, J. Semiconductor Devices: Basic Principles **2001**.

39. Stallinga, P.; Gomes, H. L.; Rost, H.; Holmes, A. B.; Harrison, M. G.; Friend, R. H.; *Synthetic Metals* **2000**, *111-112*, 535.

40. Ivanov, G. R. *Chem. Phys. Lett.* **1992**, *193*, 323.

41. Kryukov, A. Y.; Saidov, A. C.; Vannikov, A. V. *Thin Solid Films* **1992**, *209*, 84.

42. Sluch, M. I.; Godt, A.; Bunz, U. H. F.; Berg, M. A. *J. Am. Chem. Soc.* **2001**, *123*, 6447.

43. He, L. *J. Vac. Sci. Technol. A* **1997**, *15*, 951.

44. Cadby, A. J.; Lane, P. A.; Mellor, H.; Martin, S. J.; Grell, M.; Giebler, C.; Bradley, D. D. C.; Wohlgenannt, M.; An, C.; Vardeny, Z. V. *Phys. Rev. B* **2000**, *62*, 15604.

45. Shi, Y.; Liu, J.; Yang, Y. *Poly. Preprints*, **2000**, *41*, 802.

46. Nguyen, T.-C.; Yee, R. Y.; Schwartz, B. J. *J. Photochem. Photobio. A* **2001**, *144*, 21.

47. Nguyen, T.-C., R.Y. Yee, and B.J. Schwartz *Journal of Photochemistry and Photobiology A: Chemistry* **2001**, 144, 21.

48. Teetsov, J.; Vanden Bout, D. A. *J. Phys. Chem. B* **2000**, *104*, 9378.

49. Teetsov, J.; Vanden Bout, D. A. *Langmuir*, **2002**, 18, 897.

50. Hu, D.; Yu, J.; Barbara, P. F. *J. Am. Chem. Soc.* **1999**, *121*, 6936.

51. DeAro, J. A.; Moses, D.; Buratto, S. K. *Appl. Phys. Lett.* **1999**, *24*, 3814.

52. DeAro, J. A.; Weston, K. D.; Buratto, S. K.; Lemmer, U. *Chem. Phys. Lett.* **1997**, *277*, 532.

53. Frolov, S. V.; Vardeny, Z. V. *Synthetic Metals* **2000**, *111-112*, 507.

54. Herz, L. M. Phillips, R. T. *Phys. Rev. B: Condens. Matter Mater. Phys.* **1999**, *61*, 13691.

55. Jakubiak, R.; Collison, C. J.; Wan, W. C.; Rothberg, L. J.; Hsieh, B. R. *J. Phys. Chem. A* **1999**, *103*, 2394.

56. Sheridan, A.K.; Lupton, J. M.; Samuel, I. D. W.; Bradley, D. D. C. *Chem. Phys. Lett*. **2000**, *322*, 51.

57. Lim, H.; Noh, J. Y.; Lee, G. H.; Lee, S. E.; Jeong, H.; Lee, K.; Cha, M., Suh, H.; Ha, C.-S. *Thin Solid Films***,** 363, 152.

58. Edelmann, K.; Janich, M.; Hoinkis, E.; Pyckhout-Hintzen, W.; Horing, S. *Macromol. Chem. Phys.* **2001**, *202*, 1638.

59. Liu, J.; Guo, T.-F.; Shih, Y.; Yang, Y. *J. Appl. Phys.* **2001**, *89*, 3668.

60. Liu, J.; Guo, T.-F., Yang *J. Appl. Phys.* **2002**, *91*, 1595.

61. Lee, J.-I., lee, V. Y., Miller, R. D. *ETRI Journal* **2002**, *24*, 409.

62. Tanase, C.; Merijer, E. J.; Blom, P. W. M.; de Leeuw, D. M. *Phys. Rev. Lett.* **2003**, *91*, 216601-1.

63. Luo, F.-T.; Tao, Y.-T.; Ko, S.-L.; Chuen, C.-H.; Chen, H. *J. Mater. Chem.* **2002**, *12*, 47.

64. Choi, B.; Rhee, J.; Lee, H. H. *Appl. Phys. Lett*. **2001**. *79*, 2109.

65. Liao, L. S.; Fung, M. K.; Cheng, L. F.; Lee, C. S.; Lee, S. T.; Inbasekaran, M.; Woo, E. P.; Wu, W. W. *Appl. Phys. Lett*. **2000**, *77*, 3191.

66. Zheng, M.; Sarker, A. M.; Gurel, E. E.; Lahti, P .M.; Karasz, F. E. *Macromolecules* **2000**, *33*, 7426.

67. Collison, C.J.; Rothberg, L. J.; Treemaneekarn, V.; Li, Y. *Macromolecules*, **2001**. *34*, 2352.

68. Dogariu, A.; Vacar, D.; Heeger, A. J. *Phys. Rev. B: Condens. Matter Mater. Phys.* **1998**, *58*, 10218.

69. Wang, P.; Collison, C. J.; Rothberg, L. J. *J. Photochem. Photobio. A* **2001**, *144*, 68.

70. Credo, G. M.; Winn, D. L.; Buratto, S. K. *Chem. Mater.* **2000**, *xx*,xx.

71. Grell, M.; Bradley, D. D. C.; Inbasekaran, M.; Ungar, G.; Whitehead, K. S.; Woo, E. P. *Synthetic Metals* **2000**, 111, 579.

72. Pschirer, N. G.; Miteva, T.; Evans, U; Roberst, R. S.; Marshall, A. R.; Neher, D.; Myrick, M. L.; Bunz, U. H. F. *Chem. Mater.* **2001**, *13*, 2691.

73. Kloppenburg, L.; Jones, D.; Claridge, J. B.; Loye, H.-C.; Bunz, U. H. F. *Macromolecules*, **1999**. *32*, 4460.

74. Bunz, U.H.F.; Enklemann, V.; Kloppenburg, L.; Jones, D.; Shimizu, K. D.; Claridge, J. B.; Loye, H.-C.; Lieser, G. *Chem. Matter*. **1999**, *11*, 1416.

75. Nguyen, T.-Q.; Doan, V.; Schwartz, B. J. *J. Chem. Phys.* **1999**, *110*, 4068.

76. Higgins, D.A.; Kerimo, J.; Vanden Bout, D. A.; Barbara, P. F. *J. Am. Chem. Soc*. **1996**, *118*, 4058.

77. Turro, Nicholas J., Modern Molecular Photochemistry **1978**.

78. Levitus, M.; Schmeider, K.; Ricks, H.; Shimizu, K. D.; Bunz, U. H. F.; Garcia-Garibay, M. A. *J. Am. Chem. Soc.* **2001**, *123*, 4259.

Chapter 3: Near-Field Scanning Optical Microscopy (NSOM) as a Tool For Investigating Organic Thin Films

CHAPTER SUMMARY

In this chapter the resolution limitations of conventional lens optics will be discussed. Other non optical high resolution methods for chemical analysis will be presented briefly and the advantages and disadvantages associated with using these techniques in organic film characterization will be described. To extend the power and analytical flexibility of optical microscopy, a method for achieving optical resolution beyond the diffraction limit will be presented and the evolution of this idea into the modern analytical tool know as near-field scanning optical microscopy (NSOM) will also be discussed. The practical aspects of NSOM probe fabrication will be detailed, and finally the flexibility of NSOM will be discussed in regards to the numerous ways in which the technique has been adapted to address specific materials problems.

INTRODUCTION

In order to investigate organic materials on the distance scales at which optoelectronic activity occurs, it is necessary to have an optical tool with high spatial resolution capabilities. NSOM provides a means to achieve optical resolution approaching 50 nm.[1-6] Since sandwich type devices fabricated using organic thin films as active media function on a distance scale of less than 100 nm, it is imperative to have access to an optical tool suited for probing organic thin films with superior resolution. By employing an oscillating electric field

confined to the aperture of a fiber optic probe as a localized illumination source, it is possible to gain powerful optical information on a size scale not attainable with conventional far-field approaches. Higher spatial resolution provides a tool to better examine macromolecular order, intermolecular interaction, and correlated morphological/spectral relationships using optical radiation. The theory presented by Synge,[14] refined by Bethe and Bouwkamp,[15] and improved upon by many to yield modern NSOM will be detailed and described as it applies to the characterization of conjugated polymer thin films.

DESCRIPTION OF THE DIFFRACTION LIMIT

When using conventional optical elements there becomes a practical limit beyond which optical resolution can no longer be improved. Higher quality lenses or improved illumination sources are unable, at this limiting point, to offer any gains concerning optical resolving power. Since the beginnings of light microscopy this barrier to increased resolution in optical microscopy has been observed, but was only adequately described in 1873 by Ernst Abbe.[7] The Abbe barrier is a direct result of the delocalized wave properties of optical radiation. As light waves begin to interact on a distance scale approaching that of a single optical wavelength, wave interference limits spatial resolution to no better than a few hundred nanometers. Abbe described the limit formally as $\lambda/(2n \sin \alpha)$, where λ is the wavelength of the source radiation, n represents the index of refraction of the medium, and α is the angle subtended by the lens system being employed.[7]

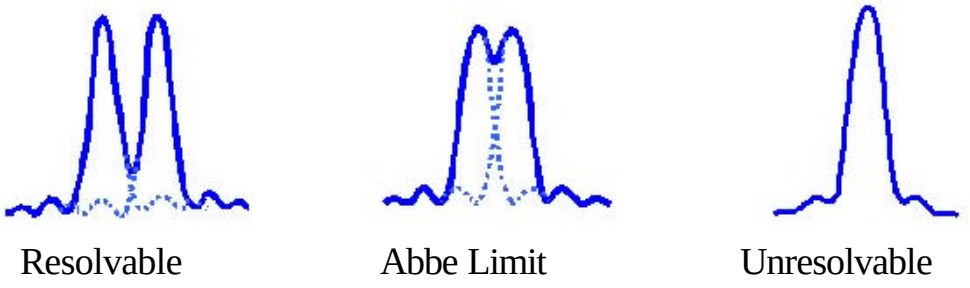

Figure 3.1 Abbe limit illustrated for the resolution of two diffraction limited objects.

Since the numerical aperture of any lens system can only practically be extended slightly beyond unity (because of the limiting behavior of n and α), the relation can be simplified to $\lambda/2$. The minimum distance between two small objects which may still be resolved using 500 nm green light is therefore approximated as 250 nm. When employing optical microscopy to observe small objects with length scales approaching that of the wavelength of the probe radiation, the wave properties of light responsible for the Abbe barrier become apparent. Airy disk patterns associated with each small object can be individually resolved at adequate separation distances, but complications arise as two objects are brought within close proximity to one another. Overlapping interference fringes around neighboring small objects create a situation where it becomes difficult to define the boundary between two or more separate objects. During the examination of these interacting Airy disk patterns, Abbe defined a working minimum limit of resolution for conventional optical microscopy. Abbe defined this limit as the distance at which the center of the airy disk associated with one object overlaps the first diffraction minima from the interference fringes of a

neighboring object.[7] His equations are a theoretical description of this rather arbitrary but useful limit.[7]

HIGH RESOLUTION CHEMICAL ANALYSIS

Numerous other higher resolution characterization techniques exist besides simple light microscopy. Electron microscopies, scanning probe configurations, and x-ray methods all hold significant resolution advantages over conventional optical approaches. The superior spatial resolution of electron imaging techniques derives from the fact that a beam of high energy, short wavelength electrons is used as a probing mechanism. The significantly smaller wavelength of electron radiation (as compared with optical sources) allows lens-based electron beam techniques to achieve imaging resolution approaching the nano scale even when confined by the restrictions associated with interacting waves. High resolution electron diffraction measurements can even be used to obtain chemical information.[8] The high energy electron beams employed in electron microscopy, however, are often too intense for organic materials and can lead to sample damage at high magnifications/large beam current densities. Increased beam current densities also result in the unwanted accumulation of static charge at the sample surface during sample observation. For this reason, both scanning and transmission electron microscopies fall victim to the fact that samples must be electrically conductive or coated with a conductive metal or carbon skin in order to prevent the detrimental effects associated with static charging of the sample. In poorly conductive samples, accumulated static charge at the sample surface interacts strongly with the electron probe beam and severely

reduces instrument resolution. The practical physics of employing an electron beam for analyses is also complicated by the need to maintain a high vacuum environment during sample analyses. This requirement limits the number and variety of samples that can be examined to those with stable structures under high vacuum and those without inner vesicles that may burst in an evacuated atmosphere.

Scanning probe microscopic (SPM) techniques present yet another viable avenue for the acquisition of morphological data on a highly spatially resolved scale. The conceptually most simple SPM tool to describe is the atomic force microscope (AFM). In AFM studies, a sharpened tip is scanned over the surface of a sample to map the surface topography. The surface resolution is, therefore, determined only by the nanoscale dimensions of the scanning probe tip.[9] The abilities to both grow single crystal probes and etch these crystals to a fine point allows for routine data acquisition with spatial resolution of only a few nanometers.[9] With high quality probes and the implementation of vibration isolation measures, microscope surface resolution can be further extended toward the molecular scale.[9] Even though AFM approaches to surface characterization provide a tool for excellent real-space sample surface mapping, little chemical information can be gleaned without the presence of some other contrast mechanism. It is for this reason that in many SPM techniques surface topography measurements are coupled with other more specific chemical data acquired from measurements of magnetic, pH, electrical conductivity, or surface hardness properties with specialized probes.[9] In this way correlated chemical data is

collected in parallel with high resolution topographic information. Drawbacks still remain even when employing these other contrast mechanisms to provide chemical information, however. Aside from the requirement for special probes, methods often require complicated sample preparation or involved experimental configurations.

X-ray analyses and high-energy neutron beam interrogation provide yet other routes to obtain high resolution chemical data. Substantial chemical information can be obtained often on distance scales approaching the atomic scale. The techniques, however, are costly and often require strict scheduling due to the scarcity of adequate radiation sources. The techniques lack the spatial resolution to effectively image a sample and do little to present information correlated to sample morphology. Both approaches also run the same hazards as electron imaging in that both high energy X-ray and neutron beams can be quite invasive and analysis may require a physically robust samples.[8] Crystalline samples are often required but since there are no consequences related to static charging, conductive and nonconductive samples alike can be analyzed.[8]

Although each of previously mentioned high resolution methods possess numerous analytical benefits, none provide the overall power and experimental flexibility associated with optical interrogation. Chemical specificity, sensitivity to molecular order, ease of data interpretation, and noninvasive nature make optical microscopy arguably the most powerful analytical tool available. One major drawback until recently, however, was the inability to employ optical techniques, especially in the visible range of the spectrum, to obtain information

on length scales smaller than ~250 nm. Progress made in the last decade extending optical resolution beyond the diffraction limit has provided a means of using optical methods on smaller length scales.[2,10-13] Fluorescence, transmission, polarization, and time resolved measurements can all now be made with spatial resolution approaching 50 nm.[4] The advantages of optical microscopy can now be employed where, previously, non optical techniques provided little chemical information or could not probe valuable optical properties with adequate spatial resolution.

BEYOND THE DIFFRACTION LIMIT

In 1928 Synge introduced a proposal to increase optical imaging resolution beyond the confines of the Abbe barrier.[14] His idea included the use of a single small sub-wavelength sized perforation in a thin opaque sheet to severely confine sample illumination to a tiny point. His proposal also suggested an approach to raster scan the point source over a sample surface and in this way produce an optical image in a pixel by pixel approach.

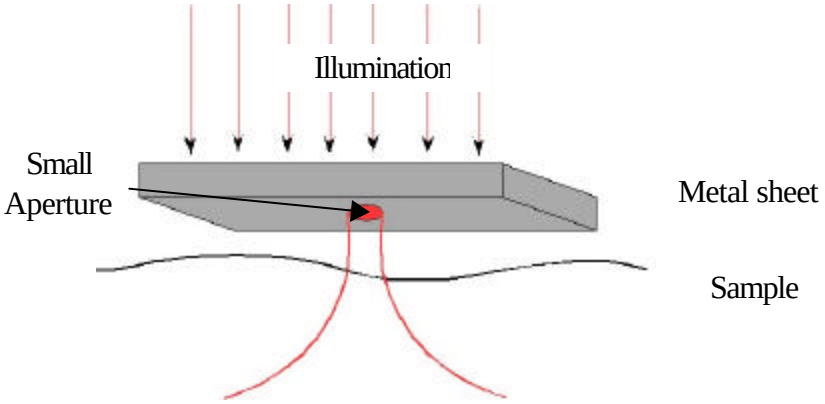

Figure 3.2 Using a sub wavelength sized aperture to confine the electric field of illuminating radiation.

Synge's original ideas concerning high-resolution optical point-source imaging were refined during the 1950s using calculations carried out by Bethe and Bouwkamp.[15] Their calculations modeled the situation that Synge had initially described, as a small hole in an infinitely thin, infinitely conducting rigid opaque sheet. Their work predicted that a plane wave incident normal to the rear surface of the conductive sheet would result in a highly confined electric field directly beyond a sub-wavelength sized opening. The calculations also revealed two other important aspects of the confined electric field. First, the confined field was shown to exist for only a few nanometers beyond the surface of the sheet before, again, diffracting and becoming limited by the Abbe barrier. And second, that the intensity of the confined electric field diminishes exponentially with distance from the sub-wavelength sized aperture. In this way, Bethe and Boukamp made explicit the importance of maintaining a small aperture/sample separation if the confined electric field at a tiny aperture was to be employed for high-resolution optical imaging. This small distance at which the effects of the

confined evanescent field can be effectively exploited is termed the near-field.[16] Specifically the distance between sample and aperture needs to be kept much smaller than a single wavelength of the illuminating radiation source. For applications in the visible spectrum, this near-field region persists for only a few tens of nanometers beyond a sub diffraction sized aperture.[15]

Even with the theoretical support provided by Bethe and Bouwkamp, it was not until 1972, that the near-field enhancement proposed by Synge would be put to practical use in an experiment employing, not optical, but much longer wavelength microwave radiation. Ash and Nichols were able to demonstrate that spacings in a metal grid could be imaged with an apertured microwave source via raster scanning to yield impressive image resolution of nearly $\lambda/60$; far beyond the Abbe barrier predicted for the source radiation.[17] This experiment provided definitive proof that near-field effects could indeed be taken advantage of to greatly enhance image resolution. Technical difficulties concerning precision nanoscale manipulation and quality aperture fabrication, however, would delay experimental near-field progress in the optical realm until the mid 1980s.

Finally, in 1984, Denk and Pohl were able to employ contemporary advances made by Rohrer and Binnig related to STEM to develop the first optical near-field microscope.[18] The team attempted to use metal-coated, sharpened quartz crystals as substrates for near-field probe fabrication but low light throughput at the tip aperture limited their application and overall ability to obtain quality high resolution images. Further advances over the next few years lead to developments in capillary, and then optical fiber, pulling procedures. These

accomplishments resulted in the fabrication of extremely sharp, glass fiber substrates offering efficient light throughput while at the same time providing a platform to produce sub wavelength sized apertures when coated with a thin metal layer to prevent unwanted light leakage. Other technological progress concerning piezoelectric scanners and nanoscale actuators during this interim period resulted in the 1991 breakthrough of Betzig and Trautman. The researchers at Bell Labs were able to present the first near-field scanning optical microscopy data using relatively robust, modern aluminum-coated, fiber optic probes to demonstrate optical resolution approaching 50 nm or approximately λ/10 in the visible spectrum.[16,19]

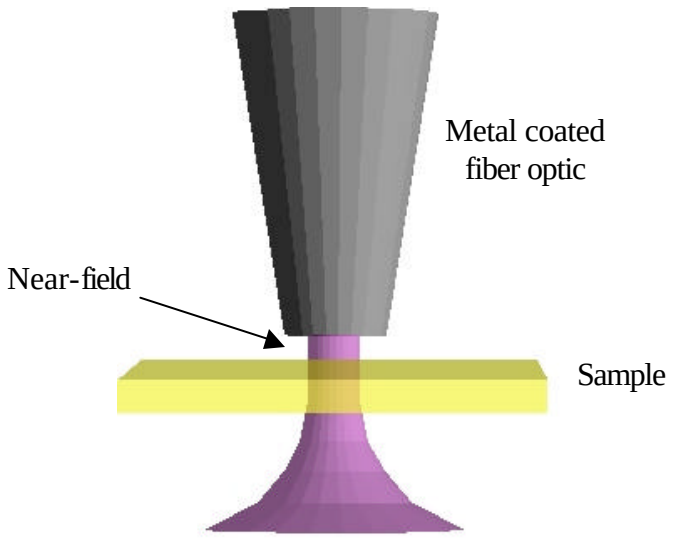

Figure 3.3 Diagram illustrating the use of a metal coated fiber optic as an apertured optical source.

FORMAL DESCRIPTION OF THE NEAR-FIELD

In microscopy the term "near-field" defines the region directly beyond a sub diffraction-limited sized aperture where high-resolution imaging can be carried out. The near-field is the region where the electric field is confined to the dimensions of the employed aperture and optical resolution is determined only by the size of this aperture. As the distance between aperture and sample increases the intensity of the evanescent field drops off exponentially while at the same time, diffraction effects become more prevalent until, at a separation on the scale of the tip aperture diameter, the image becomes analogous to that acquired using diffraction limited optics. In practical optical studies the near-field region is often described as the region between 3 and 25 nm from the aperture interface. It is only at this close separation, that the high intensity field can be exploited as a near-field illumination source, and enhanced resolution can be achieved. When a sample is scanned in the near-field regime of the sub-diffraction limited aperture the technique is synonymously referred to as near-field scanning optical microscopy (NSOM) or scanning near-field optical microscopy (SNOM).[3]

MODERN NSOM

With the monumental advances made by Betzig and Trautman concerning NSOM probe fabrication, the scanning probe technique became a feasible analytical tool for a much wider group of researchers. The optical throughput of metal-coated optical fiber probes far surpassed that which had been reported previously in the literature.[19] And although throughput was significantly increased, the size of the overall metal stylus apex was kept small to ensure high

resolution real-space surface mapping of specimens, usually on the scale of only a few tens of nanometers.

Over the next decade technical improvements as well as the commercial availability of standard NSOM instrumentation yielded great progress in high resolution near-field microscopic studies.[5,10,11,19-23] Experiments investigating sample transmission characteristics and examining mesoscale fluorescence were developed.[13,24] Reflection configurations for the interrogation of opaque specimens and collection mode approaches employing the NSOM aperture as a localized detector were also introduced.[25] Most recently, time resolved measurements and even schemes employing the near-field probe as a functioning electrode in voltage modulated studies have been devised and implemented with great success.[10,26,27]

PRACTICAL DESCRIPTION OF NSOM

In brief, modern NSOM instruments employ the tip apex of a tapered metal-coated, glass optical fiber as a sub-wavelength diameter aperture. By keeping the sample surface within close proximity of the tip aperture the high-resolution benefits of a confined electric field can be exploited and near-field imaging can be accomplished. A proven method for NSOM probe fabrication and a description of the instrument configuration employed in our laboratory will be briefly described in the following section.

The most vital aspect of NSOM imaging relies upon the fabrication of quality apertures possessing sub diffraction-limited dimensions for electric field confinement and high-resolution imaging. These apertures are currently produced

in our laboratory via a multi-step process beginning with a single-mode glass optical fiber with a 40 um diameter core (Thor Labs Cat# 1043). The initial fiber substrate with a transmission efficiency peaked at 633 nm is tapered using a commercially available capillary pipette puller (Sutter Instruments P2000). The pipette puller draws the glass fiber out into a thin taper and finally a fine point as it is heated using a focused high-intensity CO_2 laser. As the fiber melts and becomes more viscous the pulling force is adjusted in a two step pulling process to yield a reproducible taper with a sharp (<100 nm radius) needle point- adequate for high resolution SPM surface analyses.

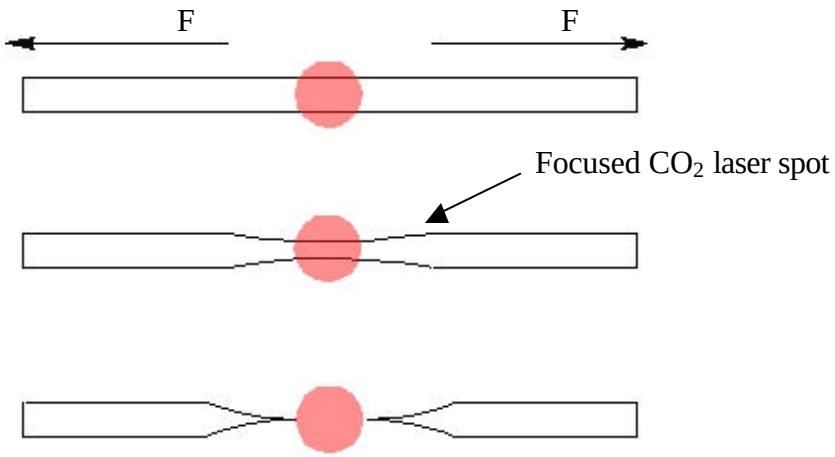

Figure 3.4 Diagram illustrating fiber optic tapering using a capillary pipette puller.

This first step in probe fabrication is vital, as the radius of the pulled tip apex ultimately determines the dimensions of the final NSOM aperture. The fiber taper is also a crucial aspect of probe fabrication as it defines overall optical throughput. The fiber pulling parameters are determined empirically to produce probes that promote efficient light transmission to the fiber apex as well as yield

sharp points. Acid etching of the glass fibers can also be employed as a means by which to produce reproducible sharp fiber tips, although this procedure is not used in our laboratory.[28-30]

Tip profiles and transmission characteristics of the pulled fibers are determined after the initial pulling stage using a conventional optical microscope. These preliminary measurements, however, offer only a rough estimate of tip quality as it is impossible to image the tiny fiber point with a diffraction limited optical scope. Once the sharpened glass tips have been produced, the fibers are subsequently vapor coated with aluminum using an angled shadow evaporation technique (Figure 3.5). This method yields only a single, small, uncoated aperture at the tip apex of each fiber. The aperture is generated by rotation of the fiber tip at 34 degrees relative to the horizontal axis, while aluminum is vapor deposited from below under high vacuum conditions (10^{-6} torr).

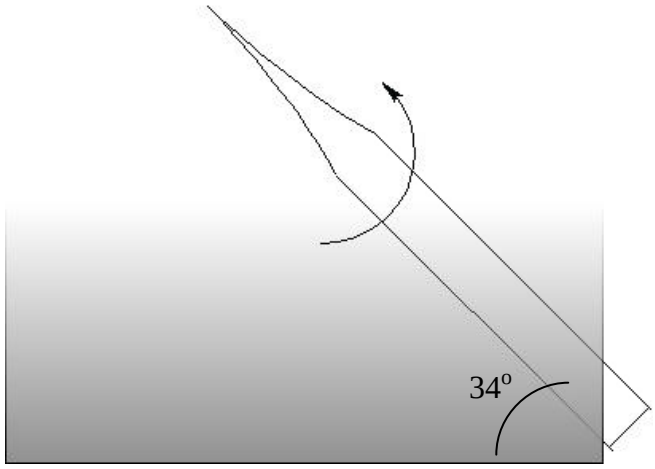

Figure 3.5 Rotation of a pulled fiber optic during aluminum shadow evaporation to produce NSOM probe apertures.

By creating a substantial distance between the evaporation source and the rotating glass fibers in the evaporation chamber, it is ensured that the metal vapor is unidirectional as it coats the spinning fibers. By controlling the deposition rate and the total amount of metal evaporated, it is possible to shadow the tip end and produce uncoated circular near-field apertures. SEM analysis of high quality NSOM probes produced in our laboratory demonstrate the presence of an 85 nm diameter aperture at the apex of a sharpened glass fiber deposited with a uniform 120 nm thick aluminum coating (Figure 3.6).

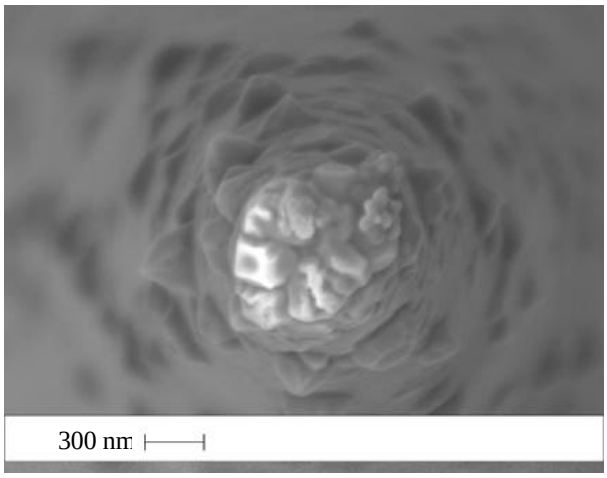

Figure 3.6 SEM micrograph displaying an 85 nm diameter NSOM tip aperture.

At this stage, the tips are again routinely examined using a simple optical microscope. This allows for a basic determination of tip size and identifies pin-holed probes, tips that are obviously too large or broken, and other probes lacking adequate optical throughput. Discarding these substandard tips at this stage of probe fabrication prevents unnecessary labor later related to tip mounting. Another possible route for aperture fabrication also exists and has been

experimented with in our lab. This procedure involves total coverage of the pulled optical fiber with aluminum during the metal vapor deposition process and the subsequent removal of metal from the end using a focused ion beam source to create an aperture in a top down approach. This method has been successfully tested in our laboratory using NSOM tips that possess no observable light throughput after simple optical examination. Focused ion beam milling of tip apertures, however, is not routine due to high instrument costs and complications involving tip mounting in the focused ion beam instrument chamber. After the preliminary optical investigation of the metal-coated fibers, select tips that are deemed adequate for near-field measurements are mounted onto 100 kHz piezoelectric quartz oscillators. The miniature tuning fork shaped oscillator (Digital Instruments/TM microscopes) comes pre-mounted from the supplier on a small circuit board that interfaces with the near-field microscope head unit.

Once the tip has been fastened to the piezoelectric quartz oscillator/circuit board chip, the NSOM probe is complete and ready for installation into the instrument. The probe is mechanically connected to the NSOM head unit (Digital Instruments/TM Microscopes Aurora II) with copper clips that also function to make electrical contact with the electrodes of the finished NSOM probe.

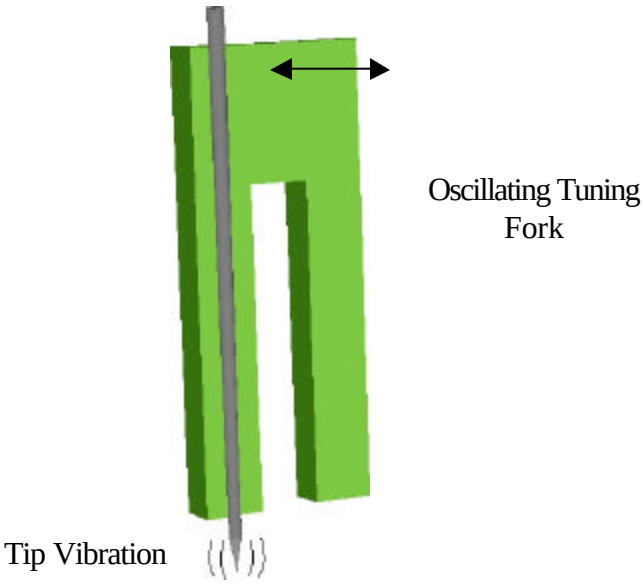

Figure 3.7 Piezoelectric quartz oscillator used to maintain electronic feedback and non contact mode imaging for NSOM analysis.

The NSOM head itself is equipped with a second set of piezoelectric oscillator circuitry that is used to drive the oscillator probe at the appropriate resonance frequency of the small tuning fork. This frequency is then monitored using a lock-in amplifier (Stanford Research Systems Model# SR830DSP) as the sample scanning stage is brought within close proximity of the NSOM tip. As the tip/sample separation approaches a few nanometers, the resonance frequency of the piezoelectric tuning fork becomes attenuated. The damped signal is read by the lock-in amplifier and the sample stage is adjusted and kept in a noncontact regime near the tip via an electronic feedback loop. It is suggested that the noncontact damping of the tip is the result of a thin layer of water molecules on the sample surface.[3] This thin contamination layer allows regulation of the

sample surface within a noncontact region only a few nanometers from the tip aperture.

USEFUL EXPERIMENTAL NSOM CONFIGURATIONS

With high resolution optical interrogation it is possible to use a number of powerful characterization techniques similar to those employed in other conventional far field microscopies. A few of the most powerful techniques used in our laboratory will be elaborated on here. In its simplest embodiment, NSOM can be configured in a straight forward transmission geometry (Figure 3.10A). Obviously, optically transparent or semi-transparent samples are needed for meaningful data collection. In this instrumental set up the probe is used as a high resolution illumination source to probe small areas of the sample film surface. Variations in index of refraction in the sample as well as film absorbance lead to differences in overall sample transmission. Transmitted signal is collected with a high NA microscope objective and subsequently focused on to the 500 um^2 active area of a high quantum efficiency detector, most notably in our laboratory, an avalanche photodiode (APD) single photon counting module. The variations in transmitted signal can be mapped as a function of overall surface position to identify areas of experimental interest or unique morphology. Transmission NSOM has been effectively used as a tool to characterize the dimensions of our in-house fabricated NSOM probes.[31] Small, isolated perforations in a metal film were imaged in transmission mode. The resulting optical signal was correlated with the topography of the associated perforation to characterize tip quality and size (Chapter 8).

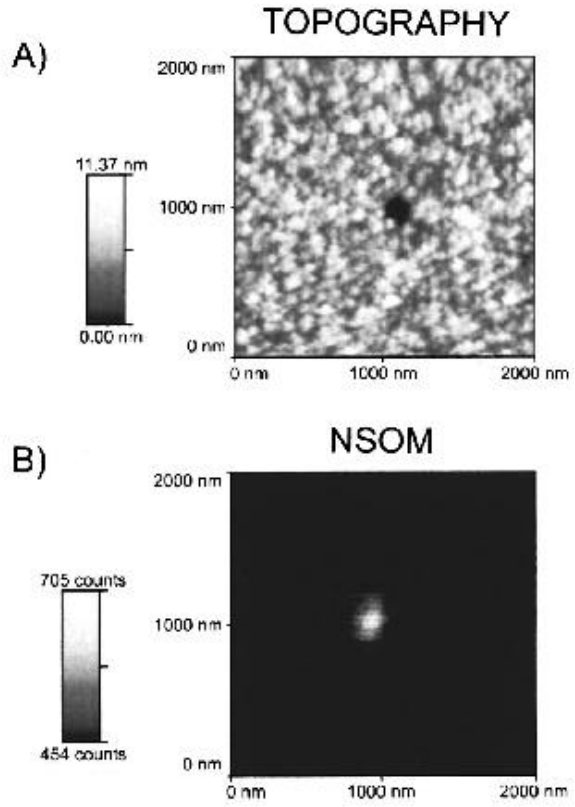

Figure 3.8 Topographic (A) and correlated Transmission NSOM (B) images of a 182 nm diameter circular perforation in a gold metal film.

Fluorescence methods can also be employed to great analytical benefit in NSOM studies. The chemical specificity and sensitivity of the technique allows for the analysis of samples ranging from phase separated polymer films of different fluorescent moieties to individual fluorescent molecules on a glass surface or in a polymer matrix.[12,24,32-34] The experimental configuration used for fluorescence data collection is only slightly more complex than that of the transmission geometry discussed earlier. Fluorescence collection requires the

implementation of a series of long pass filters between the sample and the photodetector (Figure 3.10B) . In this way, transmitted and scattered light are prevented from reaching the instrument detector and a high signal to noise ratio can be obtained during sample scanning. Focusing considerations become an issue as the effective focal length of a non achromatic lens varies with wavelength of the focused radiation. Because of this behavior, transmitted and fluorescence signals focus to different points and careful adjustment of the instrument detector is required for adequate fluorescence collection. We have used this technique to great advantage in locating fluorescent sample features.

Valuable information concerning the orientation of transition dipoles in a thin polymer film can be investigated using fluorescence polarization methods.[13,24,27,35] Fluorescence polarization NSOM is similar to the approach adapted for measurements of linear dichroism. Most often, circularly polarized excitation radiation is used to elicit sample fluorescence at the NSOM aperture. In an identical procedure to ordinary fluorescence measurements, the sample fluorescence is collected and subsequently filtered with a series of long pass optical filters. After the fluorescence has been filtered, however, the signal is split into two orthogonally polarized components using a polarizing beam splitter cube (Figure 3.10C). Each of the two signals are then focused onto two similar avalanche photodiodes. The difference between the signals collected at the two detectors can be analyzed to quantify film order and identify regions of well aligned molecular emission dipoles. In our lab this technique has proven

especially effective when examining well ordered films of conjugated polymer film samples of di-dodecyl poly(phenylene ethynylene) (DPPE) (Chapter 5).

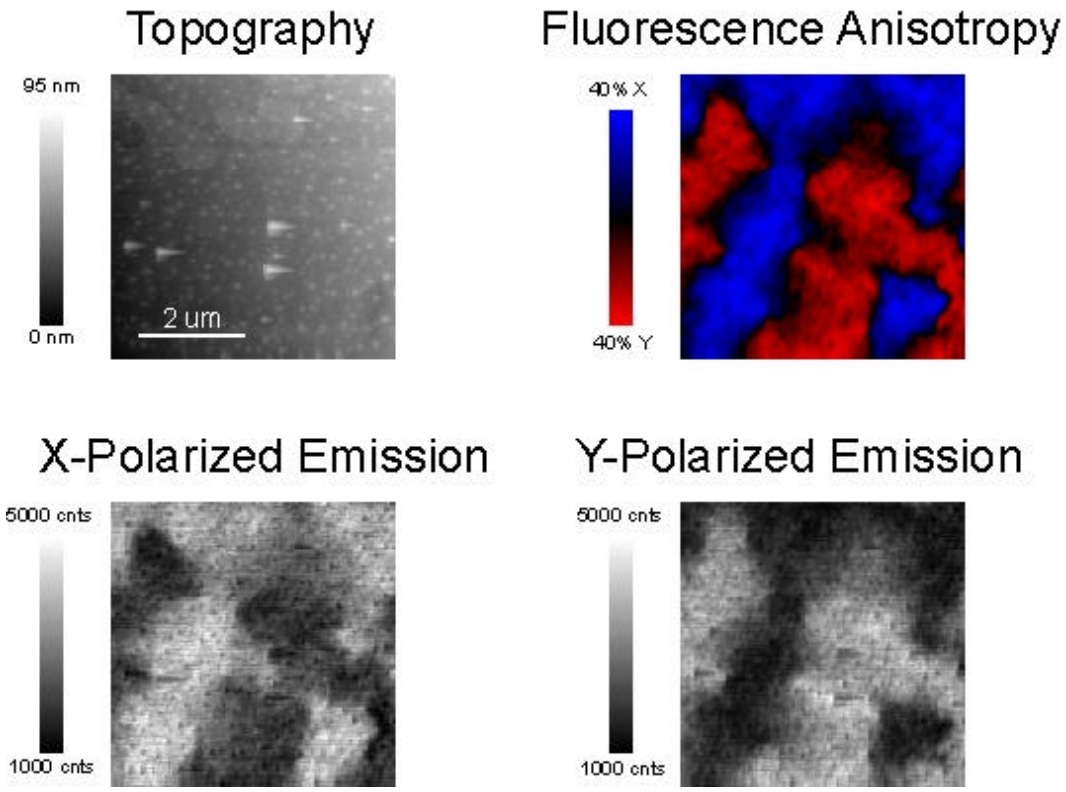

Figure 3.9 Topographic, fluorescence anisotropy, and anticorrelated polarized fluorescence emission images of an annealed di-dodecyl poly(phenylene ethynylene) (DPPE) thin film.

The final fluorescence technique to be used consistently in our laboratory involves the coupling of NSOM with time-correlated single-photon counting.[27,36] By incorporating TCSPC with NSOM it is possible to make fluorescence lifetime measurements at every pixel in an NSOM scan and gain highly spatially resolved data concerning fluorescence quenching and local fluorescence environments.

For this reason the technique is described as fluorescence lifetime imaging NSOM (FLI-NSOM). The experimental configuration is adapted from the simple fluorescence setup by again employing a beam splitter cube and two detectors for signal collection (Figure 3.10D). In the case of FLI-NSOM, however, one detector is used to monitor real-time fluorescence data and the other detector, a multi channel plate fast photo diode array (MCP), is used to collect fluorescence decay data at every image pixel. We have employed this powerful method to investigate fluorescence quenching of conjugated polymer films near a conductive metal interface (Chapter 6).

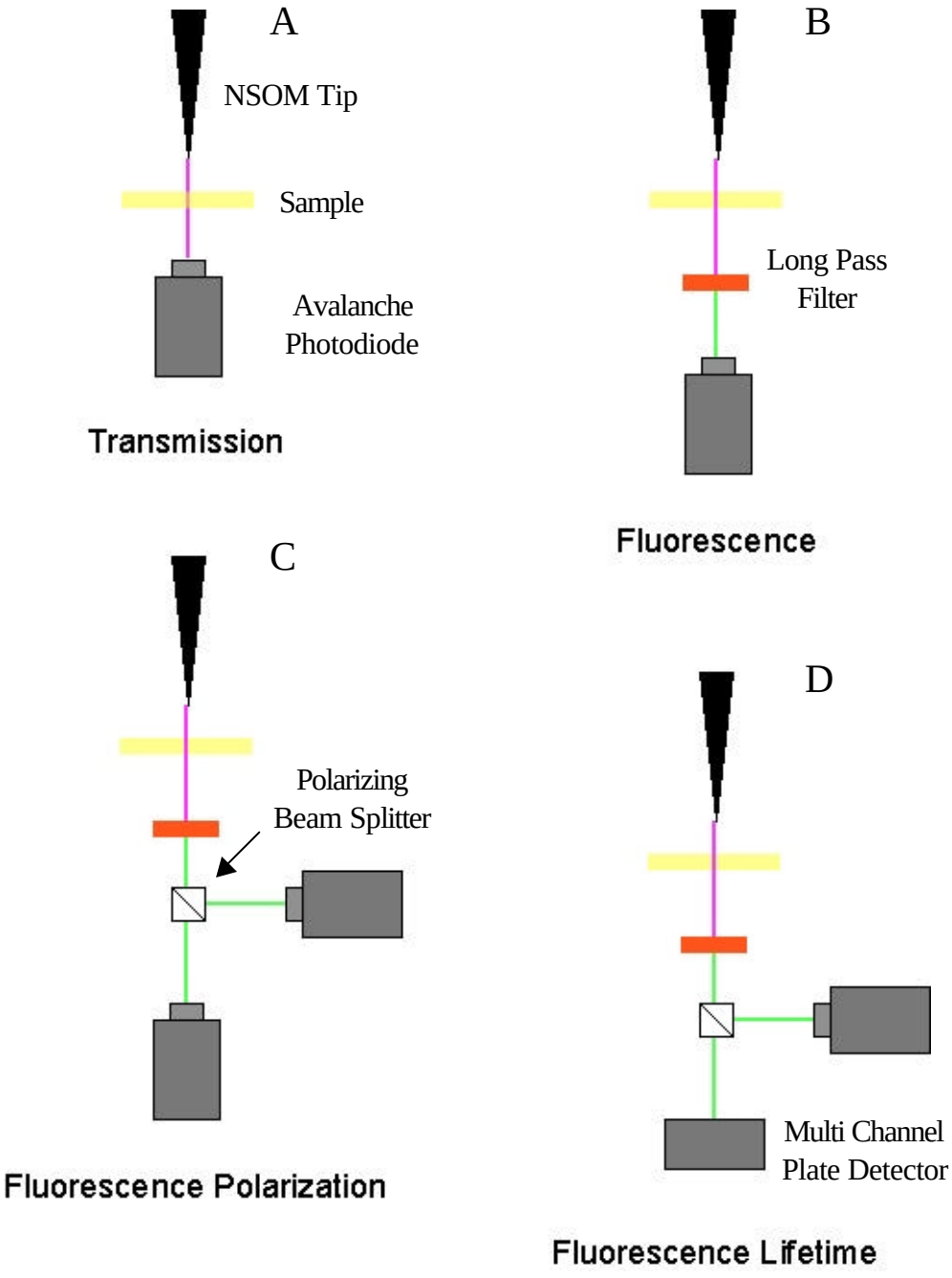

Figure 3.10 Experimental configurations used for transmission (A), fluorescence (B), fluorescence polarization (C), and fluorescence lifetime imaging (D).

CONCLUSION

In this chapter the limitations of conventional optical microscopy have been presented and an alternative means to extend optical resolution beyond the Abbe barrier has been chronicled. A brief historical overview describing ideas first presented by Synge in 1928 and the evolution of these ideas to current experimental incarnations of high resolution NSOM are outlined as well. Descriptions of the experimental NSOM configurations most widely used to great benefit in our lab have also been included for reference in later chapters. Transmission, polarization, and fluorescence lifetime, near-field methods have been outlined and will be used to examine organic thin films of conjugated polymer samples in the following studies.

REFERENCES

1. Adams, D. M.; Kerimo, J.; O'Connor, D. B.; Barbara, P. F. *Phys. Chem. A* **1999**, *103*, 10318.
2. Mei, E.; Higgins, D. A. *J. Chem. Phys.* **2000**, *112*, 7839.
3. Zenobi, R.; Deckert, V. *Angew. Chem., Int. Ed.* **2000**, *39*, 1747.
4. Dunn, R. C. *Chem. Rev. (Washington, D. C.)* **1999**, *99*, 2891.
5. Buratto, S. K. *Current Opinion in Solid State and Materials Science* **1996**, *1*, 485.
6. Hsu, J. W. P. *Mater. Sci. Eng.* **2001**, *33*, 1.
7. Moyer, P. J.; Paesler, M. A. *Near-field Optics: Theory, Instrumentation, and Applications* **1996**.
8. Brandon, D.; Kaplan, W. D. *Microstructural Characterization of Materials* **1999**.
9. Bottomley, L. A. *Anal. Chem.* **1998**, *70*, 425.
10. Adams, D. M.; Kerimo, J.; Liu, C.-Y.; Bard, A. J.; Barbara, P. F. *J. Phys. Chem. B* **2000**, *104*, 6728.

11. Barbara, P. F.; Adams, D. M.; O'Connor, D. B. *Annu. Rev. Mater. Sci.* **1999**, *29*, 433.

12. Kwak, E.-S.; Kang, T. J.; VandenBout, D. A. *Anal. Chem.* **2001**, *73*, 3257.

13. Teetsov, J.; Bout, D. A. V. *J. Phys. Chem. B* **2000**, *104*, 9378.

14. Synge, E. H. *Phil. Mag.* **1928**, *6*, 356.

15. Boukamp, C. J. *Phillips Res. Rep.* **1950**, *5*, 401.

16. Betzig, E.; Trautman, J. K.; Harris, T. D.; Weiner, J. S.; Kostelak, R. L. *Science* **1991**, *251*, 1468.

17. Ash, E. A.; Nicholls, G. *Nature (London)* **1972**, *237*, 510.

18. Pohl, D. W.; Denk, W.; Lanz, M. *Appl. Phys. Lett.* **1984**, *44*, 651.

19. Betzig, E.; Trautman, J. K. *Science* **1992**, *257*, 189.

20. DeAro, J. A.; Weston, K. D.; Buratto, S. K.; Lemmer, U. *Chem. Phys. Lett.* **1997**, *277*, 532.

21. Higgins, D. A.; Kerimo, J.; Vanden Bout, D. A.; Barbara, P. F. *J. Am. Chem. Soc.* **1996**, *118*, 4049.

22. van Hulst, N. F.; Veerman, J.-A.; Garcia-Parajo, M. F. ***J. Chem. Phys.*** **2000**, *112*, 7799.

23. Zhou, H. M., A. ; Mills, G. ; Donaldson, L. ; Weaver, J. M. R. *Appl. Phys. Lett.* **1999**, *75*, 1824.

24. Teetsov, J.; Vanden Bout, D. A. *Langmuir* **2002**, *18*, 897.

25. Buratto, S. K.; Hsu, J. W. P.; Trautman, J. K.; Betzig, J. K.; Bylsma, R. B.; Bahr, C. C.; Cardillo, M. J. *J. Appl. Phys.* **1994**, *12*, 7720.

26. Kwak, K. J.; Hosokawa, T.; Yamamoto, N.; Muramatsu, H.; Fujihira, M. *J. Microsc.* **2000**, *202*, 413.

27. Kwak, E.-S.; Kang, T. J.; Vanden Bout, D. A. *Anal. Chem.* **2001**, *73*, 3257.

28. Held, T.; Emonin, S.; Marti, O.; Hollricher, O. *Rev. Sci. Instrum.* **2000**, *71*, 3118.

29. Jung, M. Y.; Lyo, I. W.; Kim, D. W.; Choi, S. S. *J. Vac. Sci. Technol., A* **2000**, *18*, 1333.

30. Minh, P. N.; Ono, T.; Esashi, M. *Rev. Sci. Instrum.* **2000**, *71*, 3111.

31. Imhof, J. M.; Kwak, E.-S.; Vanden Bout, D. A. *Rev. Sci. Instrum.* **2003**, *74*, 2424.

32. McNeill, J. D.; O'Connor, D. B.; Barbara, P. F. *J. Chem. Phys.* **2000**, *112*, 7811.

33. Hollars, C. W.; Dunn, R. C. *J. Chem. Phys.* **2000**, *112*, 7822.

34. Shiku, H.; Dunn, R. C. *Anal. Chem.* **1999**, *71*, 23A.

35. Imhof, J. M.; Bly, R. K.; Bangcuyo, C. G.; Bunz, U. H. F.; Vanden Bout, D. A. *J. Am. Chem. Soc.* **2004**, *submitted*.

36. Imhof, J. M.; Kwak, E.-S.; Vanden Bout, D. A. *ACS Symposium Series* **2004**, *submitted*.

Chapter 4: Bulk Fluorescence Characterization of Di-Dodecyl Poly(Phenylene Ethynylene) Thin Films Under Thermal Processing

CHAPTER SUMMARY

The following group of studies were undertaken to more fully understand the basic fluorescence properties of the newly synthesized conjugated polymer, di-dodecly poly(phenylene ethynylene) (DPPE). A relative little amount of information concerning this particular poly(phenylene ethynylene) derivative is currently available in the literature. This chapter includes specific work reproducing solution phase experiments conducted by the South Carolina group, where the polymer originated, as well as new emission phenomena recognized in our lab concerning processed, condensed phase samples. Since our ultimate goal is to understand the effects of sample morphology on the electrical and optical properties of DPPE thin films, it is important to first understand their bulk photophysical properties. In particular, conventional polarization optical microscopy (POM), bulk absorption and fluorescence measurements, as well as time correlated single-photon counting (TCSPC) experiments were completed. A strong correlation between film processing and optical character was identified and an explanation for the change in emission with increased polymer order is presented in terms of molecular relaxation within a glassy condensed phase system.

INTRODUCTION

The semiconducting properties exhibited by conjugated polymer materials have made them highly attractive for application in a number of optoelectronic devices.[1-8] This interest has led to extensive research surrounding a select number of specific conjugated material families. In particular poly(phenylene vinylene) and poly(fluorene) derivatives have recently dominated the conjugated polymer literature.[9-14] An emerging new class of these polymers is that of the poly(phenylene ethynylene) (PPE) family. Materials in this class have shown high fluorescence quantum yields in the blue region of the visible spectrum and demonstrate excellent potential for use in LED and photovoltaic electronics applications.[15,16] PPE materials possess a structure where alternating acetylene linkages separate phenyl substituents. This construction enables extended conjugation along the rigid polymer backbone even when axial twisting of the straight-chain molecule is substantial.[17-20] The rigid nature and long persistence length of PPE macromolecules make them especially attractive for applications involving films of well-aligned polymer regions.[21,22] Polarization optical microscopy (POM) has been used to identify the formation of highly ordered regions in properly processed films. This structural organization is attributed to the rigid molecular properties of the PPE polymer backbone and the interaction of these long rods with each other.[15,16] It has been demonstrated that the spectral behavior of conjugated polymer thin films, in general, is intimately coupled to the overall sample morphology.[18-21] Specifically, numerous conjugated polymer studies have shown that increased film order leads to enhanced intermolecular

interactions between polymer chains and, in turn, to low-energy emissive species.[22-24] In the current investigation, a new conjugated polymer material, di-dodecyl poly(phenylene ethynylene) (DPPE)[25] was examined and direct correlations between the optical properties of the sample and polymer film morphology are identified. Bulk spectroscopic measurements and high-resolution near-field imaging are employed to examine polymer samples with varied processing histories. In much the same way as other conjugated polymer materials, it has been demonstrated that well ordered films of DPPE can be produced through thermal annealing.[26-33] In direct contrast to other conjugated systems, however, this new material is shown to yield a unique situation where both an increase in high-energy emission and only a slight reduction in overall quantum output is witnessed upon molecular reorganization to the much more ordered state. Here we present evidence that the spectral shift to higher energy emission witnessed in these films is the result of the thermal relaxation of a glassy system of interacting fluorophores.

EXPERIMENTAL

All work in the current study was carried out on the fluorescent conjugated polymer system, DPPE. The material was synthesized as previously described by Bunz et al.[16] The average polymer length is 90 repeat units as determined by gel-permeation chromatography. Dilute solution phase samples (0.05% wt DPPE in chloroform) were prepared to examine the spectral properties of isolated single macromolecules. Pristine polymer films were prepared via spin casting (2000 RPM) from a more concentrated organic solution (0.5% wt DPPE in chloroform).

The polymer samples were deposited onto base-cleaned glass microscope cover slip substrates. All samples were spin cast from solutions that had been briefly heated before spin deposition to produce transparent clear casting solutions. The resulting yellow films were subsequently placed under high vacuum (10^{-6} torr for 1 h) to remove residual solvent from the condensed phase systems. A second group of spin cast films were prepared and heated above the polymer glass transition to 200^{o}C. The heated samples were then allowed to cool back to room temperature at 20^{o}C/min to yield thermally annealed DPPE films. Both pristine and annealed films possessed thicknesses of ~70 nm as determined with AFM step-height measurements.

Absorption data were acquired using a diode array spectrophotometer (Hewlett Packard Model# 8453). Temperature controlled spectra were taken after equipping the instrument with a home-built heat exchange manifold. Temperatures between 25 and 200^{o}C could be set and regulated within 10^{o}C using the system.

All fluorescence measurements, except temperature dependent data, were acquired with a right-angle fluorometer (Photon Technologies International Quanta Master Model# C). Samples were excited at 400 nm and fluorescence beyond 420 nm was collected. The excitation beam was filtered using a 400 nm band pass filter to minimize the effects of any imperfections in the excitation monochromator grating. The fluorescence signal was also filtered using a series of long pass filters to prevent both scattered and transmitted excitation light from reaching the instrument detector. Film samples were analyzed in a reflection-type

geometry and attempts were made to limit reflection of the excitation source and maximize overall fluorescence signal. Film fluorescence was observed to depend greatly upon the orientation of the sample in the fluorometer chamber and attempts were also made to minimize angular variation between analyses of different films. Temperature dependent fluorescence data of thin-film samples were obtained employing a dual monochromator fluorometer (Spex FluoroLog) adapted with a home built temperature regulating film sample cell. The cell could effectively regulate within 10^{o}C the sample temperature between 25 and 200^{o}C.

Microscopic measurements were made using a compound optical microscope (Olympus Model# BX60) equipped with crossed polarizers and fluorescence filter cube set.

Time correlated single photon counting data were collected from pristine and annealed polymer films as well as dilute solution phase samples of DPPE using a TCSPC module with 30 psec time resolution. The instrument employs a tunable optical parametric oscillator (Coherent, Inc. Mira OPO) and a multi channel plate photodiode (Hamamatsu MCP) to achieve maximum time resolution. Samples were excited at 400 nm and time resolved fluorescence measurements were made above 420 nm in pristine samples, at both 450 nm and 500 nm in annealed films, and above 440 in solutions.

RESULTS

Dilute solution phase samples were used to collect information concerning the spectral properties of noninteracting DPPE macromolecules. These samples of isolated chromophores exhibited a single absorption peak centered near 390 nm

and appeared transparent and clear under ambient light conditions (Figure 4.1A). Little evidence of intramolecular energy transfer was witnessed as collected data were comparable with those obtained from previous studies conducted on oligomeric samples comprised of single fluorophore units[28]. The dilute solutions fluoresce in the blue region of the visible spectrum and possess emission spectra peaked near 430 nm with pronounced red shouldering near 450 nm (Figure 4.1A). With increased polymer concentration, a second absorption band appears near 450 nm while extensive red emission becomes evident beyond 450 nm in the fluorescence spectrum (Figure 4.1B). The more concentrated solutions adopt a yellow color under ambient light conditions. Mild heating can be used to eliminate both the red-shifted absorption band and reduce low-energy emission in the poorly solvated samples, rendering their absorption and emission properties identical to those of polymer in a dilute environment. Upon heating, the samples again resemble dilute systems as the solutions become both clear and transparent to the naked eye. The more concentrated solution samples exhibit only a temporary spectral transformation under thermal processing, and upon cooling back to room temperature, both the low-energy absorption and emission features return in an apparently reversible process. The solutions also return to their original yellow hue.

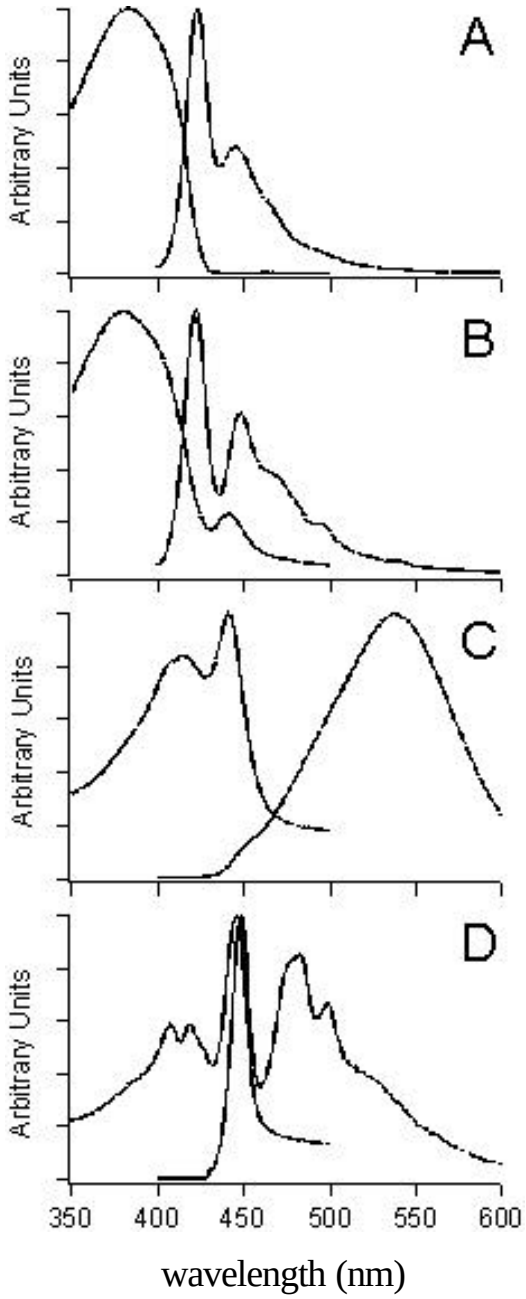

Figure 4.1 Normalized absorption and emission spectra from DPPE in A) dilute chloroform solution B) concentrated chloroform solution C) a pristine spin cast thin film and D) a thermally annealed thin film.

Pristine thin films of DPPE were prepared via spin casting from clear polymer solution. The absorption and emission properties of these yellow film samples are drastically different from those of the clear solution from which they are initially deposited. Film absorption spectra of the pale yellow films are identified as having two absorption peaks of near equal absorbance (Figure 4.1C). One peak is located near 400 nm and the other is centered close to 450 nm. Although the positions of the two absorption maxima are similar to those witnessed in the solution phase analysis of DPPE, the large intensity of the peak at 450 nm indicates much greater red absorption in the film. In significant contrast to the blue fluorescence emission seen in dilute solution, pristine films exhibit bright green fluorescence under ultraviolet excitation. The emission spectra of these films possess a single broad fluorescence peak centered at 540 nm, and present no evidence of the structured blue emission witnessed in the case of dilute solutions (Figure 4.1C).

When pristine films are thermally cycled above the polymer melt transition at 200^{o}C and allowed to cool slowly back to room temperature, the absorption and emission properties of the resulting thermally annealed films change drastically from those of the initial pristine samples. The absorption spectra of these cycled films appear slightly more structured as two peaks become apparent near 390 nm where only a single peak existed in the original pristine films (Figure 4.1D). The peak at 450 nm becomes more pronounced and narrows slightly. In addition to the changes seen in the absorption, a major change in the fluorescence signature of the films also occur. The broad green spectrum

exhibited by the pristine film is replaced by a more structured, blue-shifted emission (Figure 3.2).

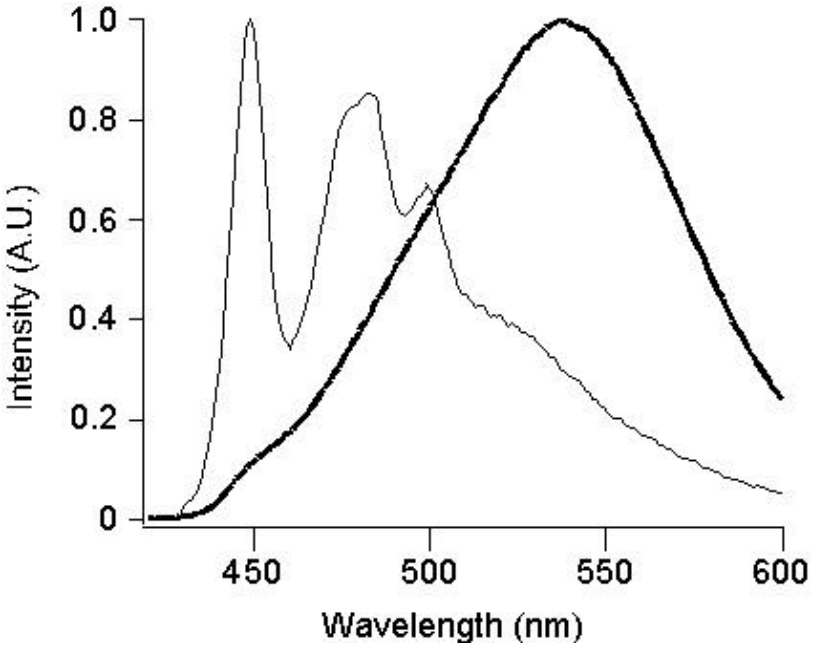

Figure 4.2 Normalized fluorescence emission profiles of DPPE in a pristine spin cast film (—) and in a film that has been thermally annealed (?).

In an attempt to further understand the transition in the spectral properties from the pristine to the annealed samples, in situ analyses of both absorption and fluorescence properties of the films were carried out using a temperature controlled film sample cell. Fluorescence and absorption spectra of a pristine film were obtained every 20°C while the sample was thermally cycled to 200°C and allowed to cool again back to room temperature to yield a thermally annealed thin film. As the pristine film is heated the absorption spectrum gradually changes from the two-peaked structure seen in Figure 4.1C to a single absorption

reminiscent of the polymer in a dilute solution environment (Figure 4.1A). The peak at 450 nm continues to decrease with increased temperature and eventually disappears completely near the melting temperature of the polymer at 180^{o}C. As the film is allowed to cool back to ambient temperature, the reverse trend is witnessed as the peak near 450 nm returns. The absorption of the initial spin cast film possessing a single maxima near 390 nm exhibits a slight increased in structure and two distinct absorption maxima can be observed near 380 and 400 nm in the annealed film. When examining the temperature controlled fluorescence data an interesting trend is also observed. The original broad green emission peak of the pristine film migrates toward higher energy with increased heating (Figure 4.3).

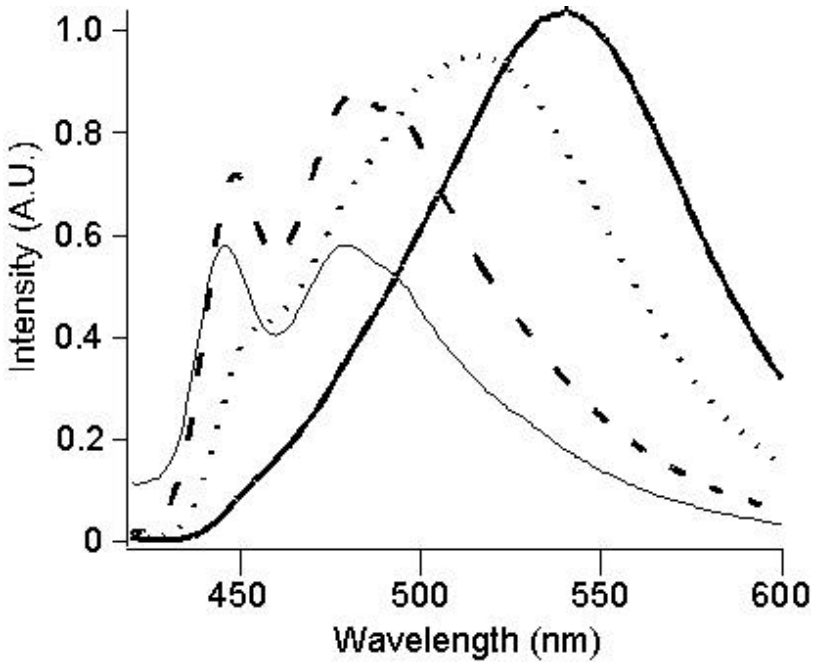

Figure 4.3 Absolute comparison of fluorescence emitted from a pristine room temperature film (?—) and the same film heated to 60°C (- - -), 110°C (**- - -**), and 150°C (?).

As the temperature approaches the melting point of the polymer, the fluorescence spectrum begins to resemble the emission exhibited by solution phase samples (Figure 4.4).

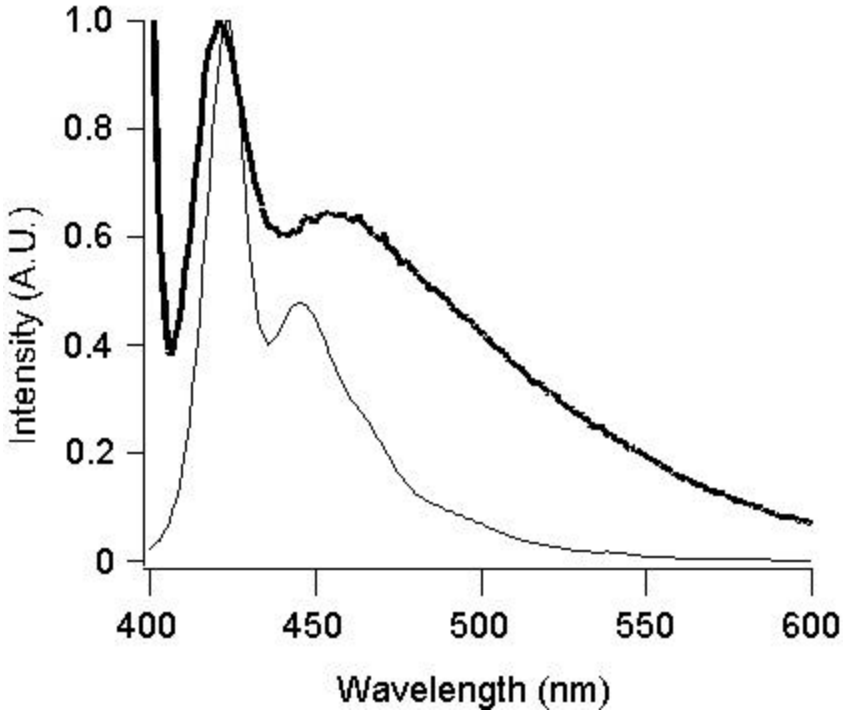

Figure 4.4 Normalized fluorescence emission profiles of DPPE in a well solvated solution (**?**) and a molten film at 180°C (—).

And in allowing the film to cool back to ambient temperature, the fluorescence spectrum shifts back toward lower energy but does not fully regain the broad green emission of the initial spin cast film. The annealed film fluorescence signature appears to be intermediate between that of the molten polymer film and that of the original spin cast sample, although it is obviously not a simple linear combination of those two component spectra. Heating of the polymer film to an isotropic melt followed by immediate removal of excess thermal energy by immersion of the film in an ice water bath, yields a spectral signature similar to that exhibited by pristine spin cast samples or samples that have undergone mild heating at 60°C (Figure 4.5).

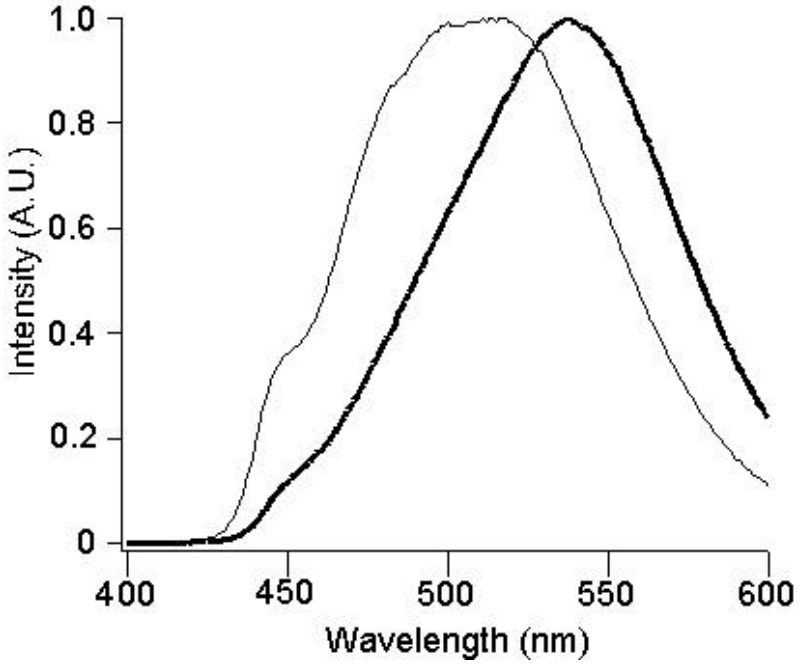

Figure 4.5 Normalized fluorescence emission profiles of pristine DPPE film (—) and a molten film flash frozen in 0°C ice bath (**?**).

Optical characterization of the thin film samples results in evidence of a pronounced difference in molecular order between the pristine and annealed films. Whereas the initial spin cast films appear uniform and isotropic when probed with conventional white-light microscopy through perpendicular polarizers, the thermally annealed films exhibit pronounced birefringent regions approaching the micron size scale that can be seen easily even with the resolution provided by conventional polarization microscopy (Figure 4.6).

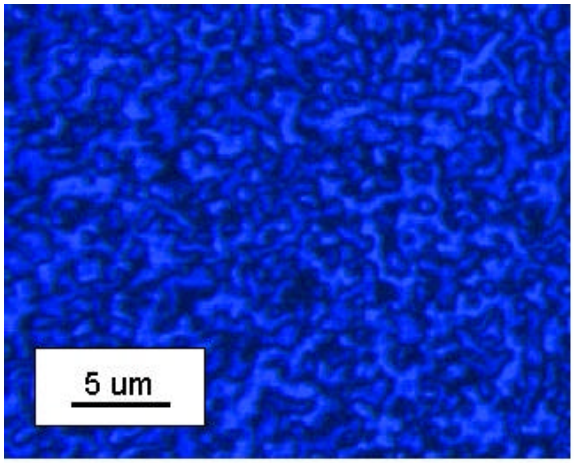

Figure 4.6 Polarized optical micrograph of a thermally annealed di-dodecyl poly(phenylene ethynylene) (DPPE) film with a total thickness of 70 nm.

Further investigation of film order using an adapted NSOM instrument configured for fluorescence polarization measurements indicates minimal optical alignment in the pristine films, whereas the annealed films exhibit enhanced fluorescence anisotropy values indicating an order of magnitude increase in molecular alignment in the thermally cycled samples (See Chapter 5).

Further in situ examination of a pristine film while it is thermally cycled to produce an annealed film demonstrates that the film is first heated to an isotropic melt and then cooled to near 150^{o}C before birefringent zones finally become apparent under POM analysis.

Fluorescence lifetime data were taken of both pristine and annealed films as well as dilute solution samples of DPPE (Figure 4.7). Pristine films are characterized by a long nonexponential fluorescence decay with an average lifetime of 4.49 ns. This fluorescence lifetime is uniform across the entire

spectral range of the pristine film emission. Upon annealing, the lifetime of the film changes dramatically. Two, much shorter, characteristic lifetimes are identified in annealed films. Fluorescence emission near 500 nm demonstrates a nonexponential decay with an average lifetime equal to 140 ps. The narrow peak near 450 nm also exhibits a nonexponential decay but with an even shorter lifetime of 90 ps. Solution phase samples reveal a single exponential fluorescence decay with a fluorescence lifetime intermediate to those measured for the two films. The lifetime is calculated as approximately 400 ps.

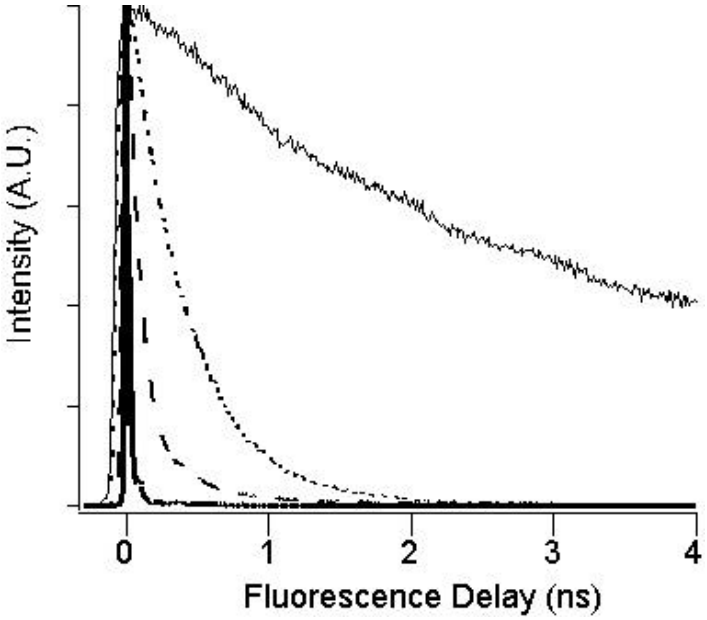

Figure 4.7 TCSPC fluorescence lifetime decays obtained from DPPE samples. A pristine polymer thin film (**?**), the polymer in a dilute chloroform solution (----), and a thermally annealed polymer thin film (**- - -**). The instrument response function is also displayed (**—**).

DISCUSSION.

The spectral trends witnessed in DPPE solutions as the concentration of polymer is increased can be easily rationalized. In dilute systems, only single, noninteracting dipoles are responsible for both sample absorption and emission. In these solution samples, the absorption possesses a single peak and the fluorescence is characterized by a spectrum comprised wholly of isolated single molecule emission. As the concentration of the polymer is increased, the absorption peak near 450 nm appears. This peak can be attributed to aggregate species formation due to molecular interaction in the ground state as chromophore concentration is increased. In the fluorescence data, a significant increase in the red emission at and beyond 450 nm becomes apparent. The presence of this emission component, displaying little Stokes shift as compared with the 450 nm aggregate absorption band, is strongly suggestive of polymer aggregate emission. When the more concentrated solution sample is heated, dipole-dipole interactions again decrease and the solution photophysics resemble that of a dilute polymer system. The same spectral effects seen in concentrated polymer solution have been chronicled in studies investigating the addition of poor solvent matrices to well solvated DPPE polymer systems.[15] The similarity of data acquired in these previous solubility experiments to the current study can be attributed to the formation of polymer aggregate species in the poorly solvated systems. Aggregate properties are shown to be greatly enhanced as interactions between molecules become more significant at higher solution viscosities/concentrations and at lower solution temperatures. It is difficult to quantify independent

aggregate photophysics or make accurate fluorescence lifetime measurements in the current study because of the overlap of DPPE aggregate absorption and emission properties with the spectra of the single molecule species remaining in solution. Both emission and excitation spectra prove independent of wavelength.

After spin casting solution samples into condensed phase films, the dramatic change in absorption characteristics from solution samples can be attributed to the formation of a new system with greatly enhanced ground state intermolecular interaction. Not surprisingly, the aggregate peak near 450 nm is a much larger portion of the overall sample absorption as the molecules come into close association with one another in the glassy film. In addition, the singlet absorption witnessed near 390 nm in solution broadens in the condensed phase as a greater distribution of frozen single chain molecular conformations are found in the glassy film system than in homogeneous solution phase samples. The broad green emission near 540 nm witnessed in pristine films is likely the result of excimer formation between the closely associated chains. Three characteristic features of the green emission are indicative of classic excimer formation. First, the pristine emission is broad and structureless, evidence of a vibrationally unstable ground state species. Next, film fluorescence is significantly Stoke's shifted from the film absorption, indicating a low-energy charge-transfer emitting species. And finally, pristine films of DPPE exhibit long-lived fluorescence signatures, often associated with poor overlap of the excited state and ground state wave functions. All three of these features, plus the lack of a new absorption band in the films, are strongly suggestive of the formation of an excited state

fluorescent excimer species. In disordered spin cast film samples it is possible for pi stacking to occur as the rigid rod polymers flatten against each other during the initial fast deposition process. This situation allows for the formation of a cofacially stacked geometry to arise in the glassy system. This face-on association is similar to that found in concentrated pyrene samples, the paradigmatic example of excimer formation.

When pristine films are thermally cycled to produce annealed samples the dramatic change in film spectroscopy can be attributed to the elimination of a molecular environment conducive to excimer formation. In contrast to the broad emission seen in pristine samples, the structured emission witnessed in annealed films is indicative of aggregate dominated fluorescence. The initial spin cast molecular geometry allowing cofacial pi-stacking in pristine films is disrupted upon, even slight, molecular reorganization in the annealed samples. The enhancement of sample film birefringence indicates a high degree of macromolecular alignment in the annealed films. Even though the samples become much more ordered upon thermal rearrangement, a situation is apparently created where the chains are at a larger separation from one another during the annealing process and are effectively solvated in the aliphatic dodecyl side chains surrounding the polymer backbone (Figure 4.8).

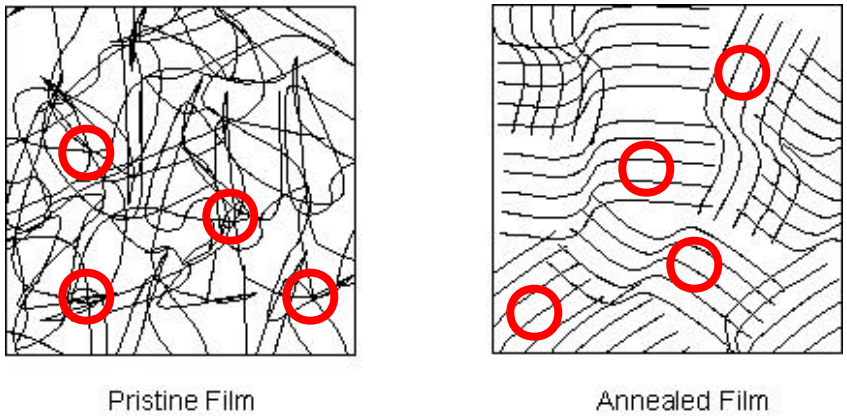

Figure 4.8 Schematic representation of majority sites (circled) responsible for fluorescence signature displayed by both pristine and annealed thin films of di-dodecyl poly(phenylene ethynylene).

In this way, each fluorophore is insulated from neighboring polymer chains enough to disrupt excimer formation. This effect is the opposite of what is typically observed in many polymer systems where excimer emission increases with enhanced polymer order.[18,24,28] The resulting system of aligned polymers in the current study is still demonstrates pronounced aggregate emission. The idea of aggregate dominated fluorescence is supported by the fact that the emission possesses little overall Stoke's shift from the sample absorption and that the emitting species are short lived compared with both the pristine film and isolated DPPE fluorophores measured in the solution phase.

To confirm that thermal rearrangement is indeed responsible for the change in the spectral characteristics of DPPE films, in situ measurements of film fluorescence were made. Direct observation of both absorption and emission properties during thermal cycling presents a clear route to characterize the optical/morphological transformation of DPPE films. It is possible to map film

spectroscopy as the temperature is cycled and gain insight concerning spectral transitions during molecular rearrangement at elevated temperatures. Without direct characterization of films undergoing thermal processing, only spectra from pristine and annealed films, the experimental endpoints, are available. With only these two spectra, valuable information concerning the spectral evolution of the films is lost.

When temperature dependent absorption data are collected it becomes obvious that the large absorption peak near 450 nm is indeed due to aggregate formation in the pristine film. As the pristine film is heated this peak gradually diminishes until it completely disappears beyond the film melt temperature near 180^{o}C. At this elevated temperature, aggregated species no longer exist because the polymer fluorophores become well solvated in the molten aliphatic side chain matrix. Upon cooling, molecular interactions in the film again increase and the aggregate absorption slowly reappears until it is again the dominant feature under ambient conditions. During thermal cycling the emergence of the two distinct absorption peaks near 380 and 400 nm in the annealed samples does not occur until the film has been completely melted and refrozen.

In examining in situ fluorescence data of DPPE films it is evident that thermal rearrangement plays a key role in film spectroscopy. As a pristine film is heated the broad green fluorescence shifts to higher energy and the emergence of a shoulder peak near 450 nm becomes evident. As heating is continued the fluorescence takes on more blue character and the peak at 450 becomes even more pronounced. Finally, upon reaching the melt temperature of the polymer,

the fluorophores transition into a system of noninteracting molecules and a fluorescence signature similar to that of a solution phase sample is elicited. The relative quantum yield measured from these molten polymer films; however, is significantly diminished from that of room temperature samples due to the presence of nonradiative relaxation pathways at high temperatures. As the sample is allowed to cool, ground state interactions again become prominent and red emission beyond 440 nm increases. With the concomitant return of the aggregate absorption band, this low energy, short lived emission can be attributed to the formation of emissive aggregate species. Upon further cooling the fluorescence of the film remains blue and structured. The green emission associated with the pristine film does not return because the film cools to a well ordered state with interchain spacings that are sufficiently large to prevent excimer species formation. If, however, the film is heated above the melting temperature and subsequently thermally quenched in a 0^{o}C ice water bath, the fluorescence of the resulting film is again dominated by excimeric emission and resembles that of the initial spin cast sample (Figure 4.5). The film is now trapped in a high energy configuration in which many chains are in close proximity. This close spatial arrangement allows for the formation of emissive excimer species between neighboring chains and again provides the ideal situation to yield excimer dominated fluorescence. Since the freezing of the film is still not instantaneous, a slight blue shift in the film emission maxima is still witnessed. The effect can be removed by annealing the sample to a lower energy equilibrium glass system.

CONCLUSION

Conjugated polymer films of DPPE provide a unique case to examine both aggregate and excimer dominated fluorescence. Fluorescence signatures from each of the separate species can be directly tied to film processing and the presence of different structural morphologies within these samples. In situ measurements of DPPE film emission show how the system evolves from a metastable glass demonstrating excimer dominated fluorescence in the pristine films to a energetically more favorable annealed film exhibiting pronounced aggregate emission. Spin casting or fast quenching of the film from the isotropic melt phase creates a high energy glassy film. In this state, many of the polymer chains are found in repulsive geometries that would not normally exist in a dynamic matrix or solution at room temperature. Thermal annealing and/or aging or allows the system to relax slowly from the metastable glass to a lower energy equilibrium conformation. This relaxation is characterized by the emergence of a blue shifted aggregate emission. In this way DPPE films with varying degrees of intermolecular interaction between polymer chains can be effectively created via thermal processing routes. The strong excimer dominated emission witnessed in pristine thin films is indicative of a disordered morphology in which many neighboring chains are close enough to have substantial wavefunction overlap. One would expect that such closely associated chains would demonstrate enhanced interpolymer energy transfer on a localized scale. Additionally, the susceptibility of these films to efficient excimer formation may yield sites of enhanced polymer chain interaction where electron/hole recombination in

electroluminescent devices may occur preferentially. This delicate condition, however, can be disrupted upon even minor thermal relaxation with the excimer state yielding to aggregate emission as seen in time resolved and steady state fluorescence measurements. By controlling DPPE film morphology and excited state species formation via thermal annealing an avenue is available for tuning thin film properties for device applications. Unfortunately in DPPE films, it is witnessed that even small increases in temperature yield substantial changes in film emission. This large change in film spectroscopy may occur under normal operating conditions found in conjugated polymer LEDs. Thus efficient devices may require thermal processing to enhance long lived stability even at the expense of overall emission yields.

ACKNOWLEDGEMENTS

Temperature controlled fluorescence and absorption data were collected on equipment in the Webber Research Group at the University of Texas at Austin. The author wishes to thank Dr. Stephen E. Webber and Dr. Ti Cao for access and assistance in acquiring these measurements. He also wishes to thank Dr. Jason B. Shear for access to the PTI fluorometer used for other photoluminescent measurements.

REFERENCES

1. Brown, A. R.; Greenham, N. C.; Burroughes, J. H.; Bradley, D. D. C.; Friend, R. H.; Burn, P. L.; Kraft, A.; Holmes, A. B. *Chem. Phys. Lett.* **1992**, *200*, 46.

2. Friend, R. H.; Gymer, R. W.; Holmes, A. B.; Burroughes, J. H.; Marks, R. N.; Taliani, C.; Bradley, D. D. C.; Dos Santos, D. A.; Bredas, J. L.; Logdlund, M.; Salaneck, W. R. *Nature (London)* **1999**, *397*, 121.

3. Yu, G.; Zhang, C.; Heeger, A. *J. Appl. Phys. Lett.* **1994**, *64*, 1540.

4. Friend, R. H. *Synthetic Metals* **1992**, *51*, 357.

5. Jakubiak, R.; Collison, C. J.; Wan, W. C.; Rothberg, L. J.; Hsieh, B. R. *J. Phys. Chem. A* **1999**, *103*, 2394.

6. Greenham, N. C.; Moratti, S. C.; Bradley, D. D. C.; Friend, R. H.; Holmes, A. B. *Nature (London)* **1993**, *365*, 628.

7. Nguyen, T.-Q.; Kwong, R. C.; Thompson, M. E.; Schwartz, B. J. *Synthetic Metals* **2001**, *119*, 523.

8. Kambili, A.; Walker, A. B. *Phys. Rev. B* **2000**, *63*, 012201.

9. Gross, M.; Müller, D. C.; Nothofer, H.-G.; Scherf, U.; Neher, D.; Brauchle, C.; Merrholz, K. *Nature (London)* **2000**, *405*, 661.

10. Babel, A.; Jenekhe, S. A. *Macromolecules* **2003**, *36*, 7759.

11. Shuknov, M. N.; Osterbacka, R.; Fuji, A.; Yoshino, K.; Vardeny, Z. V. *Appl. Phys. Lett.* **1999**, *74*, 1648.

12. Choo, D. J.; Talaie, A.; Lee, Y. K.; Jang, J.; Park, S. H.; Huh, G.; Yoo, K. H.; Lee, J. Y. *Thin Solid Films* **2000**, *363*, 37.

13. Lemmer, U.; Vacar, D. M., D.; Heeger, A. J.; Ohnishi, T.; Noguchi, T. *Appl. Phys. Lett.* **1996**, *21*, 3007.

14. Greenham, N. C.; Samuel, I. D. W.; Hayes, G. R.; Phillips, R. T.; Kessener, Y. A. R. R.; Moratti, S. C.; Holmes, A. B.; Friend, R. H. *Chem. Phys. Lett.* **1995**, *241*, 89.

15. Pschirer, N. G.; Miteva, T.; Evans, U.; Roberts, R. S.; Marshall, A. R.; Neher, D.; Myrick, M. L.; Bunz, U. H. F. *Chem. Mater.* **2001**, *13*, 2691.

16. Schmitz, C.; Posch, P.; Thelakkat, M.; Schmidt, H. W.; Montali, A.; Feldman, K.; Smith, P.; Weder, C. *Adv. Funct Mater.* **2001**, *11*, 41.

17. Miteva, T.; Palmer, L.; Kloppenburg, L.; Neher, D.; Bunz, U. H. F. *Macromolecules* **2001**, *33*, 652.

18. Halkyard, C. E.; Rampey, M. E.; Kloppenburg, L.; Studer-Martinez, S. L.; Bunz, U. H. F. *Macromolecules* **1998**, *31*, 8655.

19. Bunz, U. H. F.; Enklemann, V.; Kloppenburg, L.; Jones, D.; Shimizu, K. D.; Claridge, J. B.; Loye, H.-C.; Lieser, G. *Chem. Mater.* **1999**, *11*, 1416.

20. Deans, R.; Kim, J.; Machacek, M. R.; Swager, T. M. *J. Am. Chem. Soc.* **2000**, *122*, 8565.

21. Cotts, P. M.; Swager, T. M.; Zhou, Q. *Macromolecules* **1996**, *29*, 7323.

22. Ricks, H. L.; Choudry, U. H.; Marshall, A. R.; Bunz, U. H. F. *Macromolecules* **2003**, *36*, 1424.

23. Kim, J.; Levitsky, A.; McQuade, D. T.; Swager, T. M. *J. Am. Chem. Soc.* **2002**, *124*, 7710.

24. Kloppenburg, L.; Jones, D.; Claridge, J. B.; zur Loye, H.-C.; Bunz, U. H. F. *Macromolecules* **1999**, *32*, 4460.

25. Kloppenburg, L.; Song, D.; Bunz U. H. F. *J. Am. Chem. Soc.* **1998**, *120*, 7973.

26. Nguyen, T.-Q.; Martini, I. B.; Liu, J.; Schwartz, B. J. *J. Phys. Chem. B* **2000**, *104*, 237.

27. Schwartz, B. J. *Annu. Rev. Phys. Chem.* **2003**, *54*, 141.

28. Nguyen, T. Q.; Doan, V.; Schwartz, B. J. *J. Chem. Phys.* **1999**, 110, 4068.

29. Nguyen, T. Q.; Schwartz, B. J.; Schaller, R. D.; Johnson, J. C.; Lee, L. F.; Haber, L. H.; Saykally, R. J.; J. *Phys. Chem. B* **2001**, *105*, 5153.

30. Blatchford, J. W., Gustafson, T, L., Epstein, A. J., Vanden Bout, D. A., Kerimo, J., Higgins, D. A., Barbara, P. F., Fu, D.-K., Swager, T. M., MacDiarmid, A. G. *Phys. Rev. B* **1996**, *54*, R3693.

31. Rubner, M. F.; Sandmann, D. J.; Velazquez, C. *Macromolecules* **1987**, *20*, 1296

32. Sandmann, D. J. *Trends Polym. Sci.* **1997**, *5*, 71.

33. Teetsov, J.; Vanden Bout, D. A. *Langmuir* **2002**, *18*, 897.

34. Whitehead, K. S.; Grell, M.; Bradley, D. D. C.; Jandke, M.; Strohriegl, P. *Appl. Phys. Lett.* **2000**, *76*, 2946.

Chapter 5: Atomic Force Microscopy (AFM) and Near-field Scanning Optical Microscopy (NSOM) Characterization of Di-Dodecyl Poly(Phenylene Ethynylene) Thin Films

CHAPTER SUMMARY

AFM and polarization NSOM have been used to examine concomitant changes in surface morphology and spectral properties of organic thin films. Data in the current chapter is used in conjunction with results from Chapter 4 to formulate a theory concerning the molecular rearrangement of DPPE molecules in a glassy polymer system and the subsequent change in excited state emission properties under thermal treatment. Morphological changes in the films are induced through thermal cycling at different processing temperatures. Small changes in polymer film structure, not detectable with far field techniques, are observed with a high resolution NSOM approach. Transitions in surface morphology are also measured and confirmed using contact mode AFM.

INTRODUCTION

In the previous chapter the change in fluorescence properties of conjugated polymer thin films was examined. In this chapter, those spectral properties are directly correlated with trends involving polymer surface morphology. Di-dodecly poly(phenylene ethynylene) (DPPE) is examined and shown to form large ordered regions under thermal annealing. It is also demonstrated that glassy films of this same material can be manipulated well below the glass transition (Tg) of the polymer.[1] Atomic force microscopy (AFM) can be employed to uncover sample surface morphology with high spatial

resolution.[2] In the current contact-mode AFM approach, the sample is raster scanned beneath a sharpened silicon nitride tip. As the tip tracks across the surface during each AFM scan it produces a high-resolution map of the surface morphology in a pixel-by-pixel image acquisition.

In the current group of studies optical information is also acquired from thermally treated films of DPPE. A polarization technique is used in conjunction with high resolution NSOM imaging to yield information concerning polymer order. The method is an adapted form of the more straight forward experimental configuration used for simple fluorescence imaging.[3,4] Similar to simple fluorescence measurements, the polarization NSOM configuration uses a circularly polarized laser source for isotropic sample excitation. The method also uses a high numerical aperture (NA) microscope objective to collect both transmitted and fluorescence photons from the sample of interest. Excitation radiation is subsequently removed using a series of long-pass fluorescence filters. A polarizing beam splitter cube is employed to separate the total sample fluorescence signal into components oriented at orthogonal polarizations after the long pass filters. Two, high quantum yield detectors are then employed, instead of a single detector, to collect polarized fluorescence oriented parallel and perpendicular to the direction of the NSOM scan.

Measuring fluorescence anisotropy is conceptually similar to making a measurement of linear dichroism, but instead of examining variations in absorption with changes in illumination polarization, the technique uses a circularly polarized excitation source and collects fluorescence emitted at two

orthogonal orientations. Circularly polarized light is used to excite transition dipoles oriented in all directions of the sample plane equally. When the emitting species relax radiatively, their fluorescence is separated into separate components along the polarization axes of each of the two detectors using a polarizing beam splitter cube. By examining the differences between the normalized intensities of the detectors, it is possible to highlight regions of polymer alignment in images of thin film samples and calculate an anisotropy value, *A*, at every pixel.[3,4] *A* values are calculated by employing the following equation that examines the difference in fluorescence emission between the two detectors and normalizes the signal by the total fluorescence intensity of the sample at each pixel.

$$A=(I_{perp}-I_{para})/(I_{perp}+I_{para}) \qquad (4.1)$$

Where I_{perp} is the signal measured at the detector collecting photons polarized in the direction perpendicular to the sample scan, and I_{para} is the signal measured at the detector collecting photons polarized in the direction parallel to the sample scan. By building up a histogram of calculated *A* values, it is also possible to construct a sample distribution representing the statistical spread of *A* values in the bulk measurement of the sample film. Further calculation of the standard deviation, σ, from the resulting distribution of *A* values yields an order parameter that can be calculated so that quantitative comparisons of sample order can be made between different films or even between different materials.[3,4]

EXPERIMENTAL

DPPE Film Preparation

Three sets of polymer films were prepared for surface morphology analysis and subsequent NSOM interrogation. The films were all initially spin deposited from organic solution (0.5 wt% DPPE in chloroform) onto base cleaned glass microscope cover glass substrates. One set of films was left as prepared (pristine samples). A second set of films was heated briefly below the polymer melt temperature (70^{o}C for 1 hour) (heated samples). And another, third set of films, was heated beyond the polymer melt temperature to an isotropic liquid (annealed samples).[5] The molten samples were then allowed to cool slowly back to room temperature from 200^{o}C at 20^{o}C/min to yield thermally annealed polymer thin films. All three sets of films were approximately 70 nm in thickness, as determined via AFM step height measurements across a polymer/glass interface. All samples were cleaved into two equal halves yielding two identical films: one for AFM analysis and another for NSOM measurements.

Atomic Force Microscopy

Atomic Force Microscopy (AFM) is a surface scanning probe tool used to characterize sample morphology. AFM is used in the current study to examine the surface properties of DPPE films that have undergone different thermal treatments. The AFM yields images with lateral surface resolution of approximately 10 nm.[2,6] Contact mode AFM imaging is technically much more simple than NSOM sample analysis. This fact, coupled with the knowledge that

AFM can yield data with better spatial resolution than NSOM, makes the technique a good preliminary way to characterize sample morphology before proceeding further with near-field measurements. All of the current AFM micrographs were obtained using silicon nitride contact mode AFM probes (Microprobe 150) with 15 nm radii of curvature at the tip apex. The probes are mounted into the instrument head unit of a Nanoscope IIIa AFM (Digital Instruments/Veeco) for all analyses. Samples were prepared for AFM scanning by affixing the glass substrates to AFM pucks using double-sided adhesive. After placing the samples into the AFM head and aligning the photodiode used to measure cantilever position, force plots were obtained before scanning was commenced to adjust and minimize the contact tension between the AFM probe and the sample surface. Repeated scanning of the same sample area revealed identical surface profiles, indicating little sample damage caused by the sharpened silicon nitride probe under imaging conditions. High resolution surface images were collected from pristine, heated, and annealed thin films of condensed phase DPPE.

Polarization NSOM

NSOM is employed in the current study to obtain fluorescence polarization data that can offer insight into molecular ordering in thermally treated films of DPPE. NSOM images were acquired using an adapted Aurora II NSOM (Digital Instruments/TM microscopes). Optical measurements were acquired using a frequency doubled Ti-Sapphire laser system emitting at 400 nm. The UV laser beam was filtered with a series of short pass filters to remove

residual 800 nm emission from the Ti-Sapphire system and resulted in a 20 mW excitation source for fluorescence measurements. The beam was subsequently coupled into the home-fabricated fiber optic NSOM probe for near-field measurements. The home fabricated NSOM probes possess tip apertures of 85 nm, as determined with SEM batch analysis and measurements made using standard samples fabricated for tip characterization. Both fluorescence and transmitted light were collected using a long working distance objective and transmitted laser emission was filter out using a series of 430 nm long pass filters. The fluorescence signal was then separated into separate polarization components oriented along the direction of the sample scan and perpendicular to it, using a polarizing beam splitter cube. Each of the polarized signals were finally collected on two identical avalanche photodiode (APD) single photon counting modules (EG&G Canada). High resolution fluorescence polarization images were collected along with correlated sample surface morphology data of pristine, heated, and annealed DPPE sample films.

RESULTS

AFM micrographs of pristine spin cast DPPE films indicate a relatively smooth uniform surface morphology. A few cluster structures are present in the smooth films with lateral diameters approaching the microscale and heights of approximately 100 nm. These clusters are most likely due to poorly dissolved polymer aggregate clumps present in solution that have been carried through spin casting and remain in the final deposited films. A representative image is presented in [Figure 5.1A]. No significant order can be witnessed in the spin cast

films and the overall morphology is fairly nondescript. Even with brief thermal treatment below the glass transition temperature of the polymer, however, structural changes can be observed within the film. The formation of small clump structures with diameters between approximately 200 and 500 nm in diameter become more pronounced and the surface rms roughness of the film increases from 7 to 30 nm. The sample still exhibits no pronounced surface ordering but is of considerable interest that the sample is prone to rearrangement even below the glass transition [Figure 5.1B]. This effect may be attributed to increased polymer plasticity resulting from the presence of residual solvent in the initial spin cast film or the pristine sample existing in a strained, high energy glassy state prone to relaxation/clump formation upon the input of thermal energy. With increased thermal processing to an isotropic melt followed by subsequent slow cooling to a thermally annealed film, still greater film rearrangement is observed. Not surprisingly, the formation of micron sized meso domains is further evidence for molecular reorganization on this size scale as is demonstrated by far-field polarization optical microscopy images of the samples obtained in Chapter 4. A few cluster type structures remain in the film and again these features may be attributed to undissolved aggregates within the initial spin cast films. Although the film becomes an isotropic melt, areas of increased film thickness retain their thick character. As can be seen in [Figure 5.1C], the clump structures appear shorter and slightly broadened by the thermal cycling. The clump structures from the pristine films, therefore, become less sharp and are rounded and flattened by isotropic melting and subsequent slow cooling.

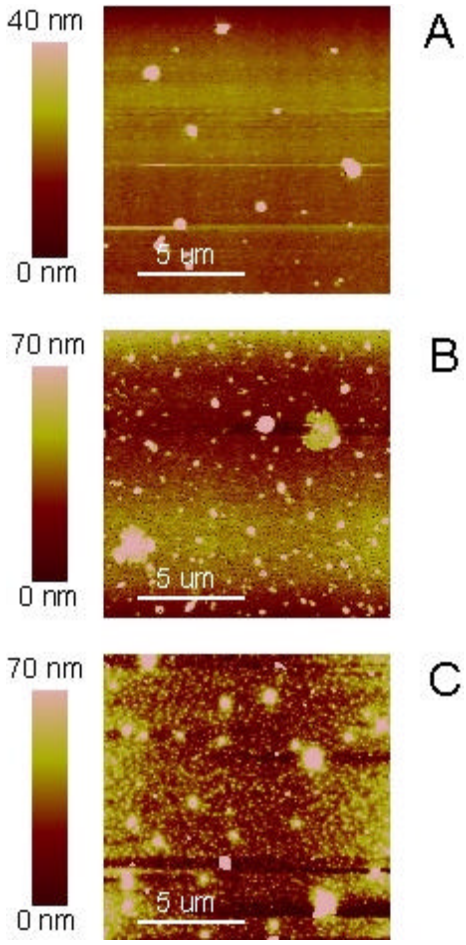

Figure 5.1 Contact mode AFM micrographs of pristine, heated, and thermally annealed films of di-dodecyl poly(phenylene ethynylene).

In good agreement with measurements made using AFM, NSOM analyses indicate a progression from a system possessing very little molecular order in pristine film samples to a system of substantial molecular alignment within samples that have been subjected to thermal annealing. Similar to results obtained with AFM analysis, the topography of the pristine films as measured with NSOM is smooth and possess only a small accumulation of surface cluster

formations approaching the 100 nm size scale. When examining the total fluorescence signal from the film, it is apparent that the entire sample is luminescent, with clusters demonstrating slightly attenuated fluorescence signals. These areas of decreased fluorescence are most likely due to the variation in thickness with the cluster formation and/or polymer self absorption.[3,4] The total fluorescence image of the pristine film in Figure 5.2 is a composite image generated by adding the signals collected from both of the orthogonally oriented detectors. Within this total fluorescence image, a phototreated 2 x 2 um^2 box is visible where a previous scan was initially collected. DPPE exhibits a curious response under UV irradiation. Whereas most fluorescent films become photobleached and exhibit a decrease in overall quantum yield, the fluorescence quantum yield of DPPE films actually increase with high energy excitation before finally bleaching at longer exposure times. This effect appears to be unrelated to localized heating as it is dependent upon the wavelength of the excitation beam. By collecting both the X and Y polarized emission components, it is then possible to generate a fluorescence anisotropy image that highlights sample film alignment using Equation 5.1. In pristine films, the fluorescence anisotropy appears uniform across the entire sample area, even within the areas that have been previously phototreated. Limited polymer chain order is indicated by the calculation of a small value for the order parameter, σ=0.039. This value, near zero, suggests that there is almost no ordering within the pristine polymer film. The calculated σ value, in fact, is not any larger than the σ value predicted from a simple calculation of the shot noise associated with the single-photon counting modules.

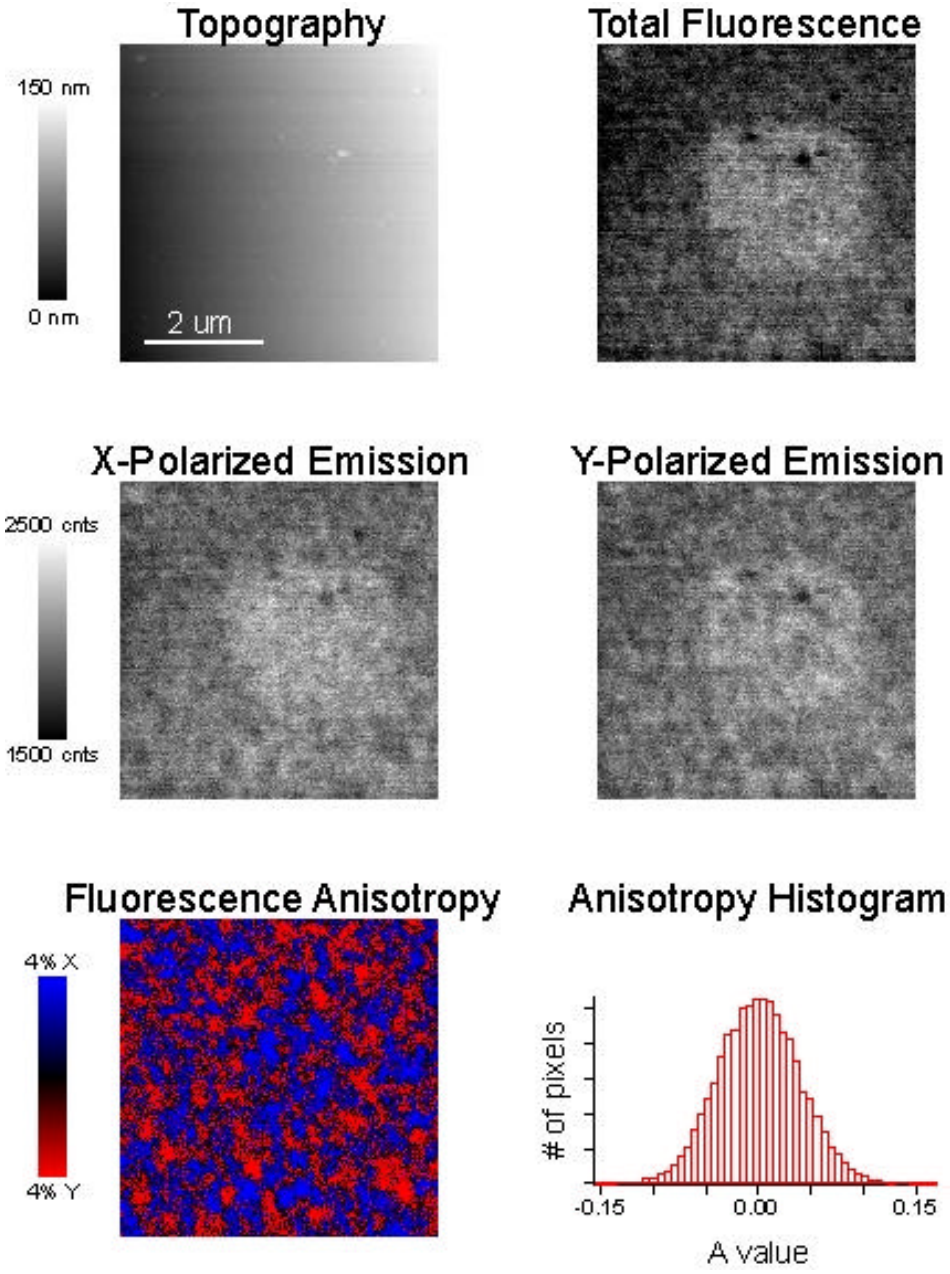

Figure 5.2 Topography, total fluorescence, polarization, and fluorescence anisotropy images of a pristine spin cast film of di-dodecyl poly(phenylene ethynylene). The standard deviation of the fluorescence anisotropy histogram yields a σ value of 0.039.

When examining heated films of DPPE, it is again, not surprising that the same topological trend is seen as in previous AFM micrographs. With mild heating below the polymer glass transition, the film begins to show increased surface roughness, most likely due to polymer chain relaxation to a lower energy conformation. No large cluster formations are seen in Figure 5.3 due to the specific area chosen for the NSOM scan. A smooth area was chosen for high resolution NSOM scanning to prevent tip aperture damage and extend the lifetime of the probe. The roughness in the film reveals a total fluorescence image with areas of high and low fluorescence intensity on the distance scale of ~100 nm. This variation in total fluorescence signal is, again, most likely due to variations in the sample film thickness on this same size scale. Obtaining the fluorescence anisotropy image allows for direct observation of polymer film alignment. Anisotropy values are measured to be somewhat higher in the mildly thermally treated films than those acquired in the pristine spin cast samples, a σ value of 0.052 is a sound indication of increased polymer chain alignment in the heated samples. Although the increase in σ value (as compared with values calculated from pristine films) may be attributed to a slightly better quality probe aperture in the current scan, it is unlikely that numerous scans over numerous days would result in the same s values being calculated repeatedly unless the probe apertures were fairly reproducible. This would indicate that the change in anisotropy values witnessed as a film is thermally processed is the result of sample ordering. With the heated samples, it appears the order parameter σ is larger than that calculated from a measure of detector noise, indicating mild molecular alignment.

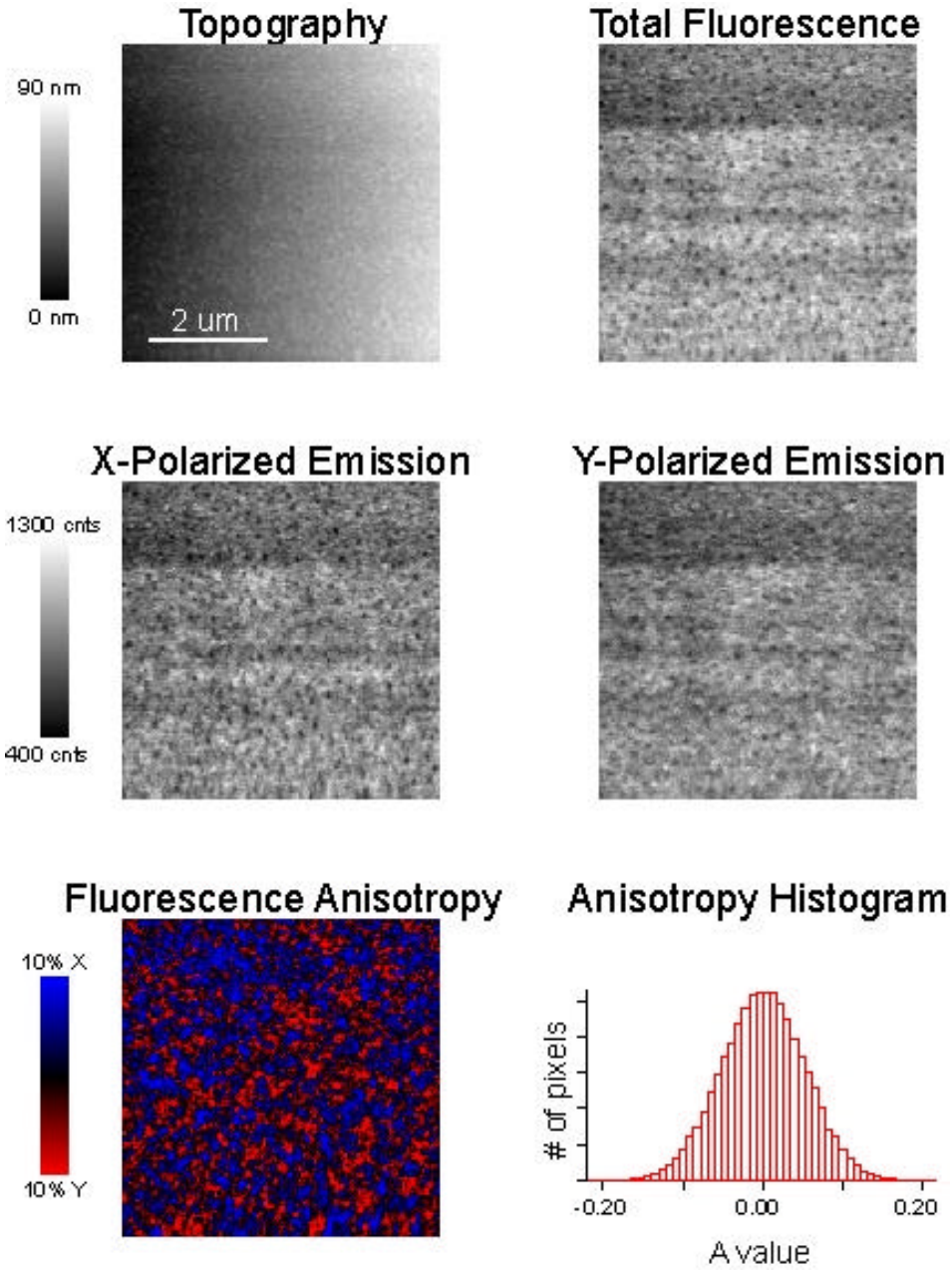

Figure 5.3 Topography, total fluorescence, polarization, and fluorescence anisotropy images of a heated spin cast film of di-dodecyl poly(phenylene ethynylene) treated at 70°C for 1 hour. The standard deviation of the fluorescence anisotropy histogram yields a σ value of 0.052.

In examining the final set of samples, the thermally annealed DPPE films, it is apparent that significant structural rearrangement has occurred within this polymer thin film. The topographic information obtained using NSOM agrees well with data acquired using AFM analysis and also with far field polarization micrographs obtained in Chapter 4. All of these results are indicative of the formation of a well ordered system of molecules under adequate thermal treatment. As with AFM, NSOM topographic analysis reveals a uniform film with a few large clustered surface structures. In examining the total fluorescence near-field image of the film no substantial polymer chain alignment is obvious. Variations in film thickness, as with the other two sets of films, are most likely responsible for small fluctuations in the total fluorescence signal. When the fluorescence anisotropy image is examined, however, polymer order is observed to be pronounced. Anisotropy values indicating nearly 40% polymer chain alignment along the collection axes in certain areas of the films are calculated. The histogram of the image becomes distinctly bimodal as the order occurs over a relatively large, micron-size length scale, and the scan size is not substantially larger than the size of these ordered regions. Although the distribution of anisotropy values is far from gaussian in nature, σ values can still be calculated to gain some insight into quantitative sample order. The σ value calculated for these well ordered, thermally annealed samples is found to be 0.292, indicating a sample with substantial molecular ordering.

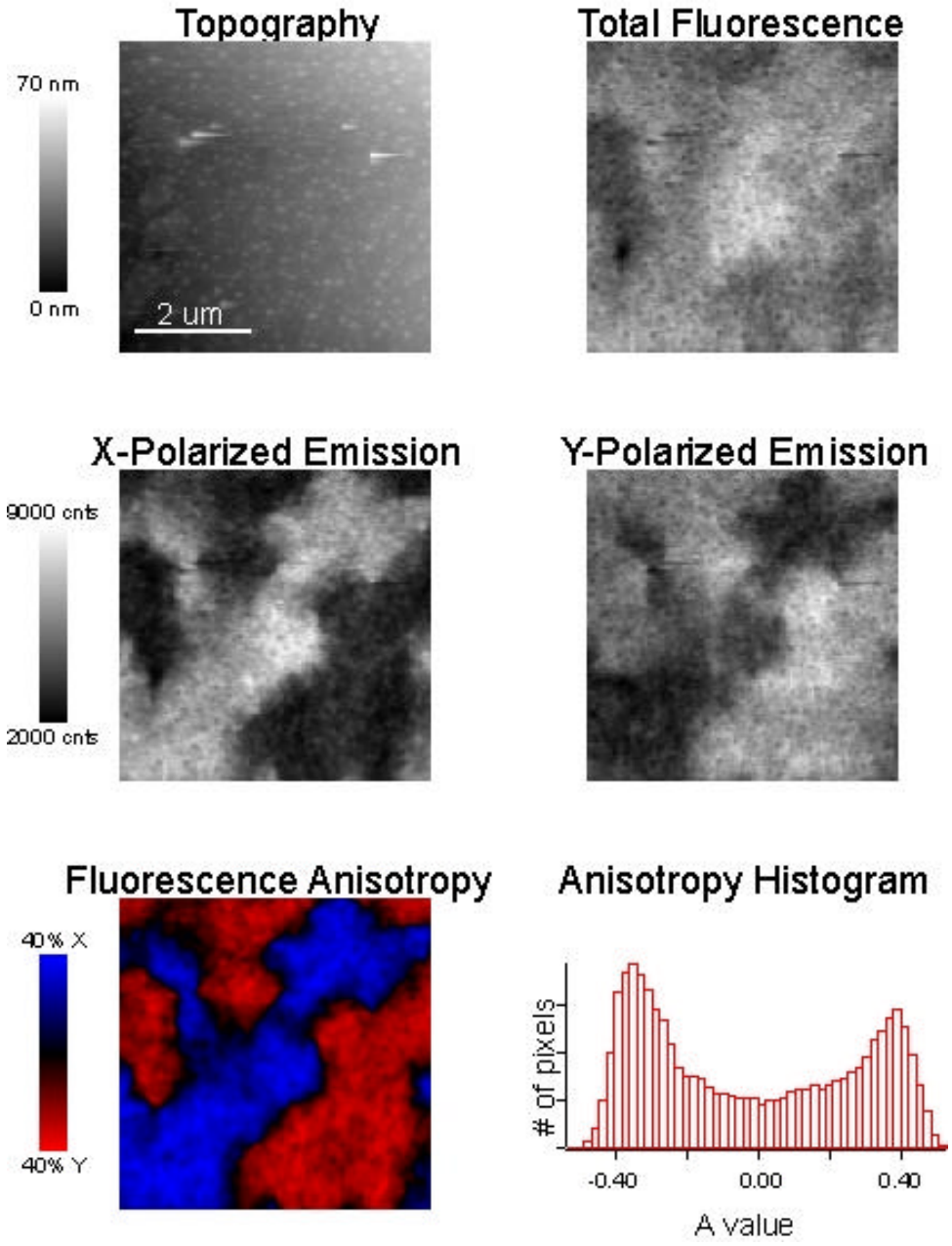

Figure 5.4 Topography, total fluorescence, polarization, and fluorescence anisotropy images of an annealed spin cast film of di-dodecyl poly(phenylene ethynylene). The standard deviation of the fluorescence anisotropy histogram yields a σ value of 0.292.

The current work has examined organic thin films of the conjugated polymer, DPPE. Collected data indicate molecular rearrangement of the rigid rod polymer moieties during thermal processing. An initial DPPE glass can be made into a more ordered glass following mild heating. Further, more extensive, polymer annealing is also seen to cause significant morphological rearrangement and molecular ordering.

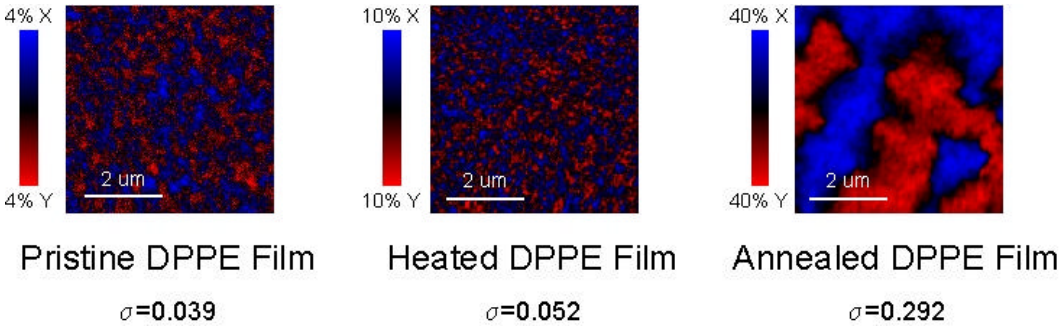

Figure 5.5 Comparison of three films and respective order parameters calculated for each. Di-dodecyl poly(phenylene ethynylene) molecular order is shown to increase with thermal relaxation of organic thin films at elevated temperatures.

DISCUSSION

AFM, NSOM, and far field optical measurements all carried out on DPPE thin films with varied thermal histories indicate that an increase in molecular reorientation/alignment occurs with increased sample temperature. This fact is significant because it appears that molecular reorganization occurs at temperatures well below that predicted by examining the polymer glass transition. This phenomena can be explained by realizing that initial spin cast films are highly strained glassy systems. NSOM analysis especially provides insight into

polymer arrangement within sample films possessing little order. By examining fluorescence anisotropy images and calculating σ order parameters for the various films, it becomes possible to identify a basic morphological/spectroscopic trend. Pristine spin cast samples are highly disordered, heated films possess slightly more organization, and annealed samples show significant regions of well aligned polymer emission dipoles. The results presented in Chapter 4 concerning bulk DPPE spectral behavior indicate a majority presence of an excimer like emission state in pristine spin cast films, while thermally treated samples exhibit a subsequent progression to a more aggregate dominated emission. This simple progression is evidence for the relaxation of an energetically unfavorable, structurally strained, glassy system, where close associations in the spin cast film are responsible for the observed excimer like fluorescence. Unlike conventional far-field polarization microscopy, polarization NSOM analysis is able to probe the sample fluorescence with adequate spatial resolution to identify the subtle molecular relaxation induced even by low temperature processing, and confirm the results of Chapter 4, mainly that films subjected to even minor thermal processing exhibit a substantial change in fluorescence emission because of polymer relaxation and molecular ordering.

NSOM is also capable of providing valuable information concerning the semi-quantitative ordering of birefringent films produced under thermal cycling.[4,7] Far-field polarization optical microscopy demonstrated the presence of micro-sized meso structure in Chapter 4, but uncertainty remained concerning the constitution of the birefringent domains. Near-field studies conducted on organic

thin films of poly(fluorene) samples have indicated the presence of small ordered regions that form a composite birefringent zone witnessed using far field microscopy.[3,4] Data in Chapter 4 was unable to discern if annealed DPPE samples exhibited this same behavior, and were composed of still smaller sub-diffraction limited sized regions. Fortunately, polarization NSOM is able to present definitive proof that the birefringent zones seen with conventional microscopy are well ordered and homogeneous on the distance scale above 85 nm. This data can be used to rule out the existence of further, smaller nanoscale subdomains that may contribute to the spectral/structural properties of the annealed films.

In the current study contact mode AFM imaging proved a valuable tool for probing high resolution surface morphology. The technique identified the presence of clustered polymer domains within the uniform film that could be further investigated using NSOM polarization techniques. Previous studies examining these clustered structures in di-alkyl poly(fluorene) films demonstrated conclusively that there was no organizational or chemical difference between these structures and the rest of the bulk film. In the current study examining thermally processed films, it is evident that even small increases in temperature provide adequate thermal energy for polymer chain relaxation. With this in mind, it would be surprising if cluster structure or spectral response differed from the smooth regions of the films. Attenuated fluorescence from these clustered areas can therefore be attributed to self absorption in areas where the films remain thick.

DATA SIMULATIONS

The images obtained using NSOM are convolutions of the actual sample properties and the spatial averaging induced by the size and shape of the NSOM probe aperture. It is possible to simulate the polymer film as a collection of non interacting dipoles. By convolving this data matrix with a matrix representing the tip aperture, it is possible to reproducibly simulate the appropriate size and distribution of mesostructure demonstrated in fluorescence anisotropy NSOM images. The simulation requires only that the diameter of the tip aperture be known, and the subsequent adjustment of the size of the molecular dipoles within the image matrix. Iterative adjustment enables generation of an image similar to that obtained in the anisotropy image. Once the simulation yields a reasonable result, indicating the correct size and gaussian distribution of anisotropy values, the size of the oriented dipole can be recorded and an estimate of the nanostructure found within the sample can be made. This technique is valuable in discerning the actual molecular organization of rigid rod polymer moieties within condensed phase polymer films.

CONCLUSION

Strong evidence has been demonstrated for the molecular relaxation of conjugated polymer species within condensed phase thin films following thermal processing. The results presented both in this chapter and in Chapter 4 have demonstrated measurable molecular reorganization using contact mode AFM, polarization NSOM, and polarization optical microscopy (POM). Glassy films were observed using far field optical methods to form strongly birefringent meso

domains upon temperature cycling. AFM is used in the current study to confirm a concomitant change in surface morphology, with the changes in surface roughness most likely being attributed to the rearrangement of polymers into a low energy pocket. The buckling of the surface to accommodate these lower energy islands leads to an increased surface roughness. NSOM analysis provides even more powerful characterization data and is employed to quantitatively measure film order and resolve explicitly the formation of homogeneous meso structure within thermally annealed DPPE films on the micron size scale. Results from this chapter indicate that small changes in molecular organization/film morphology can have a profound effect upon the optical properties of DPPE films. Large changes in luminescence behavior of conjugated polymer systems will be of significant interest in device applications where device operating temperature may fluctuate markedly and cause changes in optoelectronic spectral response.

REFERENCES

1. Kloppenburg, L.; Jones, D.; Claridge, J. B.; Loye, H.-C.; Bunz, U. H. F. *Macromolecules* **1999**, *32*, 4460.

2. Bottomley, L. A. *Anal. Chem.* **1998**, *70*, 425.

3. Teetsov, J.; Vanden Bout, D. A. *Langmuir* **2002**, *18*, 897.

4. Teetsov, J.; Bout, D. A. V. *J. Phys. Chem. B* **2000**, *104*, 9378.

5. Miteva, T.; Palmer, L.; Kloppenburg, L.; Neher, D.; Bunz, U. H. F. *Macromolecules* **2000**, *33*, 652.

6. Cooke, P. M. *Anal. Chem.* **1996**, *68*, 333R.

7. Vanden Bout, D. A.; Kerimo, J.; Higgins, D. A.; Barbara, P. F. *Acc. Chem. Res.* **1997**, *30*, 204.

Chapter 6: Fluorescence Lifetime Imaging NSOM to Examine Di-Dodecyl Poly(Phenylene Ethynylene) Quenching Near a Conductive Metal Boundary.

CHAPTER SUMMARY

The ability to obtain high spatial resolution images, coupled with time resolved data is demonstrated. Near-field scanning optical microscopy (NSOM) is coupled with time correlated single photon counting to yield a tool that can be used to measure local changes in the lifetime of fluorescence species. Fluorescence lifetime imaging (FLI) is possible with this unified technique. The chemical specificity and sensitivity of lifetime measurements to local chemical environment make lifetime measurements ideal for applications where other contrast mechanisms are not appropriate or cannot be employed due to scanning artifacts or variations in overall film thickness. Correlated morphological/lifetime data is particularly useful in probing structurally distinct areas of the film, such as cluster, that may possess similar or different spectral character than that of the bulk film. In the current study di-dodecyl poly(phenylene ethynylene) (DPPE) is observed near a conductive metal interface. The sample is fabricated to model the situation found in organic light emitting devices where an emissive chemical species is found within close proximity of a conductive boundary. Specifically, we demonstrate that fluorescence quenching near the interface occurs over a short distance scale; detectable but ill resolved by FLI-NSOM analysis.

INTRODUCTION

It has been repeatedly demonstrated that nonradiative quenching of an excited state fluorophore occurs near a metal surface.[1-3] The metal surface, when in close proximity to a fluorescent species, acts as an energy sink to provide a nonradiative route for fluorophore relaxation to occur from the first singlet excited state back to the ground state.[3] Understanding of this process has resulted in extensive modeling of nonradiative quenching near conductive interfaces and theory agrees well with experiment.[4] Numerous treatments and review articles provide in-depth explanations of this quenching effect.[3]

In recent literature concerning conjugated polymers and organic light emitting devices (OLEDs) this issue is of great interest because of the geometry of typical sandwich type light emitting systems.[5] The OLED is most simply described (and fabricated) as a layered structure with four distinct regions. Typically a transparent conductive material, most commonly ITO, is deposited on to glass or another suitable solid support structure to be used as a anode. Over the ITO is then spin cast or printed a 50-100 nm thick active layer of organic light emitting material. And finally, a metal cathode is vapor deposited over the organic layer to complete the circuit and yield a finished OLED. When a voltage is applied to the device, the transparent electrode of the system allows generated electroluminescence to escape with high efficiency. The concern with these devices is that the small dimensions of the organic active layer leave excited state fluorophores especially susceptible to nonradiative quenching near the conductive interfaces of the sandwich structure.[5] Since many conjugated polymer materials possess high hole mobility but low electron mobility, the specific worry is that

electron/hole recombination may occur directly at the interface between the polymer material and the metal cathode. This creates the best possible situation for nonradiative quenching of the luminescent excited state recombination product and the worst possible scenario when considering overall device efficiency and OLED quantum yield. The current study is an attempt to quantify the distance scale on which fluorescence quenching occurs in conjugated polymer light emitting devices. By modeling a typical sandwich OLED structure with a planar configuration. A polymer/metal interface will be fabricated using gold and the conjugated polymer, di-dodecyl poly(phenylene ethynylene) (DPPE).[6] In the current study it will be possible to make quantitative measurements using high-resolution near- field scanning optical microscopy (NSOM)[7-9] coupled with time-correlated single-photon counting (TCSPC) to yield a fluorescence lifetime imaging (FLI)-NSOM technique.[10,11] Practical suggestions regarding typical OLED device improvement will be presented explicitly, and the sensitivity of fluorescence lifetime imaging FLI-NSOM as an analytical tool will be sufficiently demonstrated.

EXPERIMENTAL

Fluorescence Lifetime Sample Preparation

Preparation of the polymer/metal interface specimens used to investigate quenching of a conjugated system near a metal boundary were prepared as follows. Microscope cover slip substrates were soaked in a basic aqueous solution (15 wt% KOH) under sonication for 10 minutes to yield clean, uniform substrate surfaces. The cover slips were then triply rinsed with deionized water and

sonicated in a pure water bath for an additional 10 minutes before being dried in a 70^{o}C oven. The cleaned substrates were then coated with gold (40 nm thickness) via sputter coating to yield smooth, uniform metal thin films. Each gold coated cover slip was then scored with a sharp razor edge resulting in a smooth, crisp, linear metal/glass boundary. Conjugated polymer solution (0.5 wt% DPPE in chloroform) was subsequently deposited via spin casting (4000 RPM) over the etched gold boundary. The resulting 45 nm thick polymer film provided uniform coverage of the substrate surface with little roughness across the metal/glass threshold. This method provides an easily located and identified metal/polymer boundary for further NSOM analyses. DPPE is a conjugated polymer system that, in spin cast, condensed phase thin films, possesses a singlet absorption peaked in the ultraviolet at 390 nm, while the emission is broad and structureless and peaked in the visible green near 540 nm. Fluorescence lifetime measurements of pristine DPPE films exhibit nonexponential fluorescence decays with an average lifetime of approximately 4.49 ns.[12]

Time Correlated Single Photon Counting

As the name implies, TCSPC relies upon the ability to count single fluorescence photon events. In our laboratory this is accomplished in a reverse timing procedure. The time difference between the triggering of a fast photodiode by an excitation photon and the detection of a delayed fluorescence photon at a micro channel plate detector is measured. In the current reverse timing scheme the initial excitation pulse is used as a stop pulse for a time-to-amplitude converter and the arrival of a fluorescence photon at the detector represents the

start pulse. Each single photon event is then binned according to its arrival time using a multi channel analyzer (MCA). By repeating this process it is possible to build up a distribution of single photon events and construct a fluorescence decay from the ensemble collection. If the method is to be used effectively in a raster scan imaging approach it is necessary to wait long enough at each image point to build up a substantial number of fluorescence photons to generate a decay with adequate signal-to-noise. In this way, TCSPC is easily coupled with NSOM. NSOM requires rather slow dwell times during raster scanning using shear-force feedback, so that the additional acquisition of fluorescence lifetime data does not introduce a requirements for significantly more instrument time than other standard NSOM measurements.

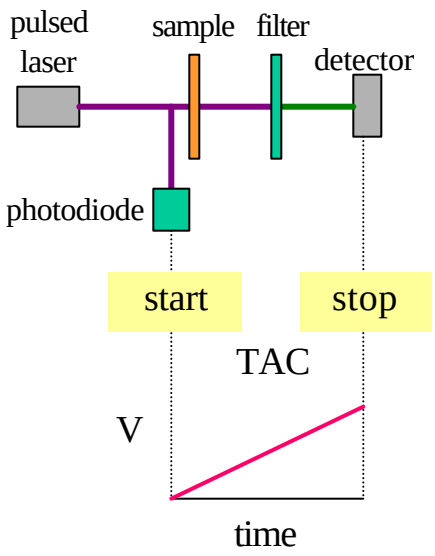

Figure 6.1 Schematic representation of the time-to-amplitude (TAC) converter used to measure fluorescence lifetimes in time-correlated single-photon counting measurements. A pulsed UV laser is used for excitation and triggers the TAC start pulse, while a green fluorescence photon functions to stop the TAC (forward timing mode).

Basic FLI-NSOM Instrument Configuration

Fluorescence lifetime imaging (FLI) near- field scanning optical microscopy (NSOM) is a technique allowing for the simultaneous acquisition of highly spatially resolved images with accompanying time resolved fluorescence data. These measurements are made by coupling the high spatial resolution of NSOM with the time resolution benefits of TCSPC technology. The current instrument will be described here. A commercial NSOM instrument (Aurora II, Digital Instruments) has been modified to acquire both simple fluorescence data as well as make more complex polarization measurements that allow insight into sample ordering on the mesoscale. The microscope also employs a frequency doubled Ti-Sapphire laser emission as a 400 nm excitation source for fluorescence measurements. The laser source pulses with a frequency of 81 MHz and allows accurate fluorescence lifetime measurements up to 10 ns with the 13 ns delay between adjacent pulses of peak laser intensity. Even longer lived events can be probed if a pulse picking cell is employed to reduce the effective repetition rate of the laser pulse train. In the current study, the full 81 MHz train of 400 nm pulses is coupled into a fiber optic NSOM probe fabricated in-house (detailed in Chapter 3). A shadow evaporation technique produces a circular metal aperture at the NSOM tip apex that can be used as a localized excitation source for subsequent near-field fluorescence analyses. In order to perform non contact, shear-force sample scanning the fiber optic is mounted to a 100 kHz piezoelectric quartz oscillator. In this noncontact method, the sample is kept within the near-field of the tip aperture as the sample is raster scanned beneath the NSOM probe.

High resolution morphological data can be collected along with powerful optical information and lifetime data using relatively short 10 ms dwell times and employing a reverse timing mode for time-correlated data collection.[13] Sample fluorescence beyond 430 nm is collected using a high NA microscope objective and a series of long pass filters. The fluorescence signal is split into two orthogonally polarized components similar to polarization NSOM approaches. In FLI-NSOM, however, only one polarization component is detected with an avalanche photodiode single-photon counting module (APD), while the other orientation is collected via the fast photodiode array of a multichannel plate detector (MCP). This fast response detector is then used for collection of time-resolved fluorescence decays of the sample. The APD is used for real-time fluorescence monitoring at every image pixel, while the MCP collects lifetime decays at every point to be analyzed later. Although the two detectors collect light of orthogonal polarization, no adverse effects are apparent when examining a highly disordered isotropic pristine spin cast DPPE film. Both the time-to-amplitude converter and multi channel analyzer necessary for TCSPC measurements are contained on a single PCI card (Timeharp 1000). In this way, an entire fluorescence decay can be collected at every pixel, stored quickly, and analyzed later. Without a multichannel analyzer the experiment can still be performed using dual or triple channel approaches, but the ability to examine different time windows is lost after the initial data acquisition process has been completed. The time resolution of the current instrument is limited by the response of the employed MCP detector. Instrument response of the system was

calculated by examining the decay profile exhibited by the MCP of the transmitted laser pulse train through an uncoated glass microscope coverslip. The measured instrument response was 500 ps.

RESULTS AND DISCUSSION

The current work examines representative FLI-NSOM images obtained of the conjugated polymer, DPPE, spin cast over a metal interface. The topology of the polymer film is uniform with only a few minor cluster structures appearing on the sample surface that otherwise exhibits an rms roughness of only 7 nm (Figure 6.2A). The metal boundary can be seen easily in the topographic image of the NSOM scan as a vertical cliff on the edge of a 40 nm thick plateau. The region of the sample possessing a metal film is also evident when examining the total fluorescence signal of the NSOM scan. Since the polymer film is excited over the metal film and the fluorescence must, subsequently, travel through the metal layer before collection at the APD, the total fluorescence signal appears significantly attenuated in the metal coated sample regions. The resolution, defined by the NSOM tip aperture, controls the sharpness of this boundary between light and dark regions in the fluorescence image. In the current study this resolution is approximately 100 nm, indicating a high quality NSOM aperture.

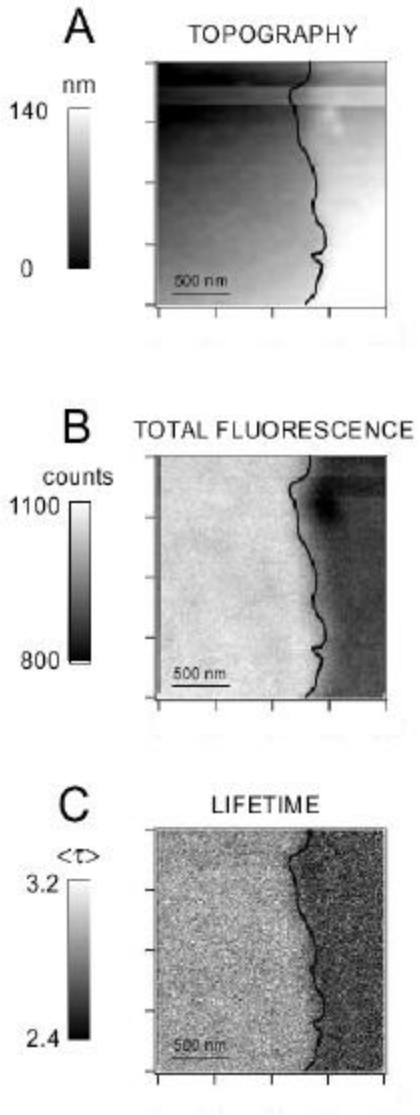

Figure 6.2 A single 2 x 2 um FLI-NSOM data scan provides A) topographic B) total fluorescence and C) lifetime images of a DPPE/gold interfacial region. The metal interface was traced in image A and superimposed on to both images B and C. Average lifetimes, $<\tau>$ values, were calculated from single-exponential fits to the resulting fluorescence decay at each pixel.

The most powerful information provided during the NSOM scan, however, results from the simultaneous collection of time-correlated fluorescence decays at every image point. By approximating the fluorescence decay profile of the DPPE as a single exponential decay, the following equation can be used to make a qualitative comparison of the average fluorescence lifetimes measured in areas of the sample exhibiting both quenched and unquenched fluorescence profiles.

$$<t>=-T/\ln(I_f/I_T) \qquad (6.1)$$

where <t> is the average calculated fluorescence lifetime of the emitting species, I_T represents the total number of photons emitted during the entire fluorescence decay, and I_f represents the fraction of fluorescence photons emitted after a certain cutoff time, T. In the current study, T=2 ns was chosen as an arbitrary cutoff time and <t> was calculated at every point in the 2 x 2 um NSOM image scan along the sample region along the metal polymer interface. As stated previously, the cutoff time, T, can be shifted during later data analysis to maximize image contrast and search for interesting time resolved properties. In a situation where a purely single exponential decay were being observed, a change in T would have no effect of the calculation of <t>, but when examining the current set of non exponential decays, T will have an impact on the calculated, <t> value. In this initial fluorescence lifetime image, it was evident that their were two distinct regions with distinctly different fluorescence lifetimes.

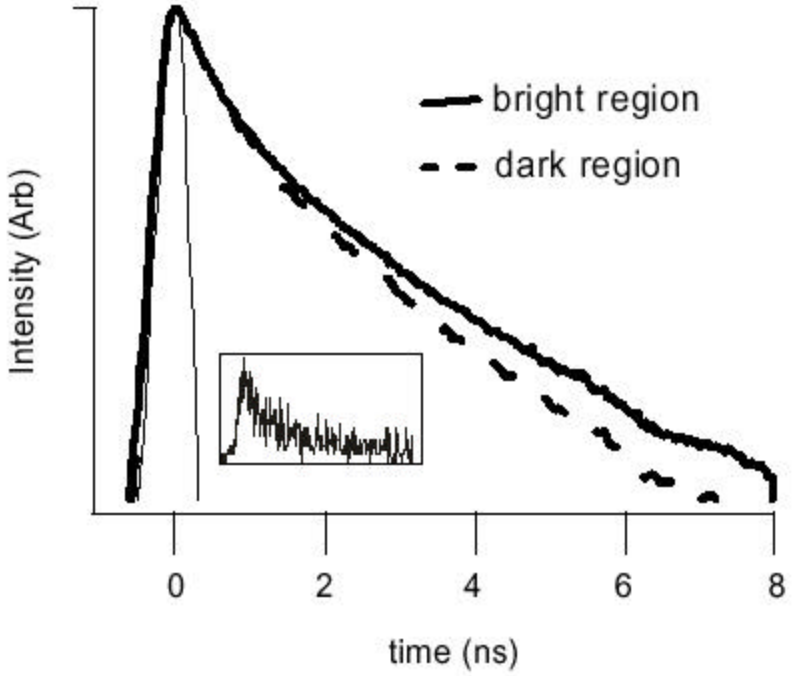

Figure 6.3 Log plots of fluorescence decays constructed by averaging 1000 pixels in the dark region (dotted) and the bright region (solid) of Figure 1C. The instrument response is also plotted. Inset: A fluorescence decay from a single image pixel.

Since lifetime decays from a single pixel typically consist of only a few hundred photons with a 10 ms dwell time (Inset Figure 6.3), the signal to noise can be greatly increased by summing the counts from separate image pixels within a common region of interest. In the current study, 1000 pixels were averaged in both the long and short lived regions of the image to produce high signal to noise decays where accurate determinations of a <t> value for the polymer film in both regions could be made (Figure 6.3). The FLI-NSOM image

provides a unique and reliable way to visualize sample fluorescence lifetime and enables simple determination of regions with different lifetime signatures. The collected fluorescence decays are not single exponential in nature due to the numerous structural conformations adopted by the large disorganized polymer molecules in the glassy spin cast film. The large number of random conformations provides a variety of differing environments and degrees of interpolymer interaction that can be easily identified through the nonexponentiality of the DPPE film decays. Even though the decays are not single exponential, it is still possible to compare the decays obtained from the two different film regions. From the curves produced from pixel averaging it was possible to observe that the fluorescence decays between the two regions differed significantly only at times beyond 1.63 ns. T=1.63 ns was subsequently used as the cutoff time, T, to generate the fluorescence lifetime image shown in Figure 6.2C. This T value provides the greatest image contrast between the two regions of the sample and highlights differences caused by quenching at the polymer/metal interface.

Three main points should be stressed concerning the resulting fluorescence lifetime image. The first, and most obvious point, is that the contrast provided by FLI-NSOM is substantial, even for the small difference in <t> calculated for the two regions of the polymer thin film. The subtlety of the lifetime quenching over the metal surface can be attributed to averaging of the lifetime information in the z-direction in the 40 nm thick film. Excited state fluorophores may be quenched quite severely directly at the metal boundary but this information is averaged with lifetime information from other fluorophores in

the cross-section of the film that are located farther from the metal surface and are less prone to nonradiative quenching interactions at Förster energy transfer distances. The overall effect is a quenched decay that differs only slightly at times beyond 1.63 ns as compared with the unquenched system over glass.

The second major aspect of the fluorescence lifetime image not to be overlooked is the solid black curve spanning the image from top to bottom. This line represents the superimposed boundary of the metal film in the plane of the sample scan and it can be drawn because of the direct correlation between surface morphology and optical information during the NSOM scan. The boundary is determined by tracing the metal interface in the topographic image and transferring the curve to the fluorescence and lifetime images. The superior sensitivity and contrast of FLI-NSOM enables the detection of nonradiative fluorescence quenching beyond this boundary and into the bulk polymer region of the sample. The quenching effect, however, remains difficult to quantify as the quenching region is not of uniform penetration and the effect is small. The ability to detect this quenching effect but not to resolve its dimensions indicates that the quenching behavior beyond the metal interface is less than the resolution of our tip and can be estimated to be effective on a maximum distance between 20 and 50 nm; in good agreement with the data obtained concerning quenching over the metal surface itself in the 40 nm thick polymer film. The ability to detect any fluorescence lifetime quenching on the small length scales involved at the interface is a testament to the sensitivity of FLI-NSOM. The third interesting characteristic of the fluorescence lifetime image concerns the chemical specificity

of FLI-NSOM. When examining NSOM images generated from total fluorescence signals, scanning artifacts and variations in sample thickness often present problems concerning accurate data interpretation. Cluster like areas of conjugated polymers often appear less intense in total fluorescence intensity images but this effect may be attributed to self absorption in the thicker regions of the film and not a quenching mechanism. Scanning artifacts also often complicate data analysis along topological boundaries or interfaces. Small changes in the distance between the sample surface and the near- field aperture often lead to dramatic changes in fluorescence yields. These small changes in distance often occur when scanning over large objects in the tip path when shear force tracking has a tendency to vary slightly. When examining the images in Figure 6.2 it is easy to identify both of these types of phenomena. There is a slight glitch in the tip tracking in image 6.2A near the top of the scan, and a number of polymer cluster structures that have low total fluorescence intensity are visible in image 6.2B. In image 6.2C, however, it is apparent that neither variation due to sample thickness nor to scanning artifacts have caused significant image contrast. In this way, clustered features on the sample surface can be seen to possess the exact same fluorescence lifetime as the remainder of the bulk film.

Fluorescence lifetime imaging provides for the clear identification of two distinct sample regions: unquenched polymer fluorescence over glass, and quenched polymer fluorescence over a gold surface. This data is simple to interpret as it is not complicated by image scanning or tip tracking artifacts. The cleanness of the image is due to the normalizing effect of calculating the

fluorescence lifetime image from the ratio of fluorescence photons beyond a certain cuttoff time to the overall fluorescence intensity.

CONCLUSION.

The current study has demonstrated the viability of FLI-NSOM as a powerful analytical tool. Three main aspects of FLI-NSOM were highlighted in this work. This imaging technique provides high contrast information that allows for minor changes in fluorescence lifetime to visualized easily and effectively. High resolution optical data collected during FLI-NSOM scans enable the method to be sensitive to phenomena that are effective on a small distance scale, similar to those fluorescence quenching along a conductive metal interface. And although the method is sensitive to small chemical and environmental differences it is not, however, complicated by variations in sample thickness or other scanning artifacts common to most other NSOM imaging techniques. This stability allows for accurate interpretation of high resolution images without the pitfalls common when simply examining measurements of total fluorescence intensity for fluorescence quenching.

The current study also indicates the presence of nonradiative fluorescence quenching on distance scales comparable with those found in thin sandwich-type light emitting polymer devices. We have demonstrated explicitly the dangers associated with single layer OLEDs; especially those devices with unbalanced electron/hole mobility values where excited state species may accumulate near a conductive boundary. The efficiency of OLEDs fabricated using active layers with high hole mobility can be increased by employing a second polymer material

as a electron transporting layer. In this manner the area of electron/hole recombination will be distanced from the metal cathode and the effects of nonradiative quenching can be reduced. Fortunately, we have also demonstrated that fluorescence quenching at the polymer boundary will not appreciably limit our ability to make high resolution measurements of photoconductivity or light emission near a conductive interface in planar device configurations. Planar devices with bulk polymer active layer dimensions in the micron range should prove relatively unaffected by the short range quenching effects of the employed metal electrodes that occur over only a few tens of nanometers. It may also prove beneficial to examine the distance dependence of nonradiative quenching in the presence of an induced external electric field. Simple experiments in our lab measuring film fluorescence near the metal boundaries of a functioning metal/polymer/metal device, however, have yielded results that sample fluorescence remains unaffected by changes in device bias over the size scales accessible with high-resolution NSOM methods.

REFERENCES

1. Azoulay, J.; Debarre, A.; Richard, A.; Tchenio, P. *Europhys. Lett.* **2000**, *51*, 374.
2. Li, L; Ruzgas, T.; Gaigalas, A. K. *Langmuir* **1999**, *15*, 6358.
3. Waldeck, D. H.; Alvisatos, A. P.; Harris, C. B. *Surface Science*, **1985**, *158*, 103.
4. Enderlein, J. *Chemical Physics* **1999**, *247*, 1.
5. Heeger, A. J. *Sythetic Metals* **2002**, *125*, 23.

6. Bunz, U. H. F; Enkelmann, V.; Kloppenburg, L.; Jones, D.; Shimizu, K. D.; Claridge, J. B.; zur Loye, H.-C.; Lieser, G. *Chem. Mater.* **1999**, *11*, 1416.

7. Paesler M. A.; Moyer, P. J. Near-field Optics: Theory, Instrumentation and Applications; John Wiley and Sons: New York, 1996.

8. Teetsov, J.; Vanden Bout, D. A. *Langmuir* **2002**, *18*, 897.

9. Teetsov, J.; Vanden Bout, D. A. *J. Phys. Chem. B* **2000**, *104*, 9378.

10. Kwak, E.-S.; Kang, T. J.; Vanden Bout, D. A. *Anal. Chem.* **2001**, *73*, 3257.

11. Kwak, E.-S.; Vanden Bout, D. A. *Analytica Chemica Acta* **2003**, *496*, 259.

12. Imhof, J. M; Bly, R. K.; Bangcuyo, C. G.; Bunz, U. H. F.; Vanden Bout, D. A. **2004**, manuscript submitted.

13. Lakowicz, J. R. Topics in Fluorescence Spectroscopy; Plenum Press: New York, 1991; Vol. 1: Techniques.

Chapter 7: Optoelectronic Device Fabrication Using Di-Dodecyl Poly(Phenylene Ethynylene) Active Layers and The Characterization of Molecular Light Emitting Species

CHAPTER SUMMARY

Both typical sandwich type light emitting devices (LEDs) and small gap planar LEDs have been produced using di-dodecyl poly(phenylene ethynylene) (DPPE) conjugated polymer materials as active semiconductor layers. Electroluminescent spectra obtained from devices fabricated using pristine and annealed films of DPPE as active layer materials have been used to identify chemical species responsible for light emission in devices made from this novel polymer compound. Planar devices have also been fabricated to facilitate high resolution optical investigation of optically active sites. Similar optoelectronic behavior from planar devices fabricated using annealed and pristine films of DPPE further confirms that the same chemical species is responsible for light emission in both of these films. Promising preliminary work examining the viability of localized photoconductivity measurements using near-field scanning optical microscopy (NSOM) is also presented.

INTRODUCTION

Since the discovery of conjugated polymers in the early 1990s great advances have been made concerning their technological application and implementation in optoelectronic devices.[1-6] As organic semiconducting materials, their utility as active layers in simple light-emitting panels was

recognized early on. Great progress has continued to be made in this realm and polymer LED light sources can now be produced with electroluminescent efficiencies beginning to rival those of current power-efficient fluorescent lamp sources.[7] To further enhance light emission and capitalize on processing advantages offered by these new materials it has become of prime concern to explicitly characterize carrier transport processes in these polymeric systems and identify sites of efficient electron/hole recombination in hopes of improving device light emission. In conventional inorganic light emitting diodes it is well documented that current flow under a controlled bias will elicit light emission.[8] Besides simple LED structures, semiconductors can be employed in photovoltaic applications and in photodetectors.[3] When a semiconducting diode is exposed to radiation of the appropriate wavelength, current can be made to flow in the reverse overall process to that occuring during light emission, in this way a photovoltaic device can be produced. The ability to efficiently generate electricity from visible radiation is an area of enormous interest for implementation in inexpensive renewable alternative energy sources like large-area solar cells. Organic conjugated polymer semiconductors can exhibit similar photovoltaic behavior under appropriate processing and device fabrication conditions. Most polymer-based LEDs and photovoltaic cells are typically fabricated in a multi layered sandwich cofiguration to maximize the surface area of the active polymer layer, although interdigitated device geometries have recently been explored as well.[9] Although much empirical work has been completed to maximize electroluminescence and improve overall organic device

performance, a number of fundamental issues concerning excited state species formation and localized charge transport remain unresolved. Since material spectroscopy has been demonstrated to depend significantly on morphology and local chemical environment, further research is particularly need developing these correlations under typical conditions found during optoelectronic device operation. An attempt to make in situ measurements of localized organic LED electroluminescence and photoconductivity is described here.

Previous experimentation and theory

A number of experiments have been carried out in an effort to directly characterize the processes involved with light emission and photoconduction in conjugated polymer condensed phase device systems. The most straightforward set of experiments, carried out by Lemmer et al., has involved direct optical imaging of electron/hole recombination in LED devices with planar electrode geometries.[10] Luminescence from a relatively large 20 micron electrode spacing constructed on a freestanding MEH-PPV polymer film was observed at liquid nitrogen temperatures with a long working distance microscope objective. The researchers lacked adequate optical resolution to observe specific regions of preferential light emission, however, and a simple asymetry in the spatial emission profile was the only phenomenon observed. In this simple planar symmetric device no attempt was made to optimize carrier mobility. As the injection efficiency differs significantly for electrons and holes, as well, the overall asymmetry in device electroluminescence is not surprising. As MEH-PPV

is a much better conductor of holes than electrons, uneven charge injection and transport results in increased electroluminescence near the device cathode.

In a separate study carried out by DeAro et al., the high resolution imaging benefits of near-field scanning optical microscopy were employed to investigate stretch aligned films of the conjugated polymer, MEH-PPV.[11] A device geometry similar to that used by Lemmer et al. was used to make localized measurements of device photoconductivity. Freestanding films of MEH-PPV had been stretch aligned to yield an oriented aspect ratio of nearly 10:1 aligned in the direction perpendicular to the electrode gap axis. On top of this ordered film were vapor deposited two gold electrodes using a 20 micron thick tungsten wire as a mask to produce the device line gap. In this set of experiments a large bias (200V to produce a field of 10^7 V/cm) was placed across the electrode gap and correlated images of surface morphology coupled with photocurrent induced in the polymer film were obtained.[11] Correlations between sample fluorescence, photoconductivity, and surface morphology were all explored. The relatively large dimensions of the device led to inconclusive data regarding film alignment and photoconduction, with only one small aligned feature being well correlated in both the photoconductivity and morphology images. The research group concluded that this aligned feature was oriented parallel to the axis of the applied electric field (stretch axis) and that near-field illumination resulted in increased photoconductivity in this region of the film. The group also concluded that enhanced charge carrier separation in this aligned region results in a quenching of overall fluorescence signal at this particular feature.[11]

Most often charge carrier transport is investigated in polymer materials using simple time-of-flight experiments.[12,13] These studies involve photoexcitation of charge carriers in the first few nanometers of a strongly absorbing polymer film between two electrodes. Under bias, either electrons or holes are selected to migrate through the film (typical thicknesses ~3um) in a strong electric field. When the carriers reach the side of the device opposite the initial photoexcitation, a characteristic transient response can be measured. This approach is useful in determining relative bulk mobilities in various materials but lacks the spatial resolution required to directly image light emission or identify centers associated with efficient charge separation or light emission.

The following sets of experiments were undertaken in an attempt to clarify the physiochemical processes responsible for light emission in organic thin films of di-dodecyl poly(phenylene ethynylene) (DPPE). Methods similar to those employed by Heeger at al. and Buratto et al. are improved in order to gain definitive, high-resolution optical data correlating polymer film order and device operation. In the first section of this chapter will be described standard sandwich OLED fabrication and the data collected from devices constructed employing DPPE thin films with different thermal processing histories. To allow for high resolution optical imaging, it is necessary to fabricate an electrode structure conducive to microscopic interrogation and this is discussed in the second part. High resolution is accomplished by fabricating a planar structure similar to those used by Heeger et al. and Buratto et al. In the current study, however, two major improvements have been made. In the first major adjustment, a much smaller line

gap is employed to increase imaging resolution. The 20 um line gap employed by previous groups is replaced with a much smaller 1 um gap instead. This reduction in distance allows for device operation at much lower voltages, and better simulates the distances found in functioning polymer optoelectronics. The smaller gap is created using focused ion beam milling technology, as opposed to an evaporative shadow masking technique. The second improvement involves the microscope. A high magnification, long working distance, objective is used to better spatially resolve the interelectrode gap and provide insight into regions of improved light emission or charge separation. Data collected from these devices will be combined with results from Chapters 4 and 5 to present a complete picture of light emission and carrier transport in devices fabricated from thin films of DPPE. In the third, and final, section of the chapter, preliminary data measuring DPPE photoconductivity using an NSOM aperture as a localized illumination source is presented.

Investigation of Electroluminescent Behavior in Sandwich LEDs of DPPE

Initial studies examining conjugated polymer light emission and photoluminescence were all carried out using simple sandwich LED structures. These devices were fabricated in a typical bottom-up multi layer technique using recipes provided in the literature.[14,15] ITO ($50\Omega/cm^2$) coated borosilicate float glass microscope slides (Delta Technologies) were cut to the appropriate dimensions and employed as rigid device substrates/support structures. The ITO surface was etched into a small strip running lengthwise along the center of the rectangular glass substrates using aqua regia solution and a thick organic mask

(Krylon H/D Outdoor Spray Paint) to protect the ITO region of interest. After rinsing the substrate in an organic solvent to remove the mask layer, the etched substrates are further plasma cleaned for five minutes to remove any remaining organic contamination from the organic masking procedure. What remains is a clean strip of ITO, positioned down the center of a glass chip, that can function as a transparent anode in LED applications. It is at this point that conjugated polymer films are deposited via spin casting (2000 RPM) from conjugated polymer solution (0.5 wt% DPPE in chloroform) over the face of the glass/ITO anode resulting in uniform polymer thin films of approximately ~70 nm in thickness (Figure 7.1).

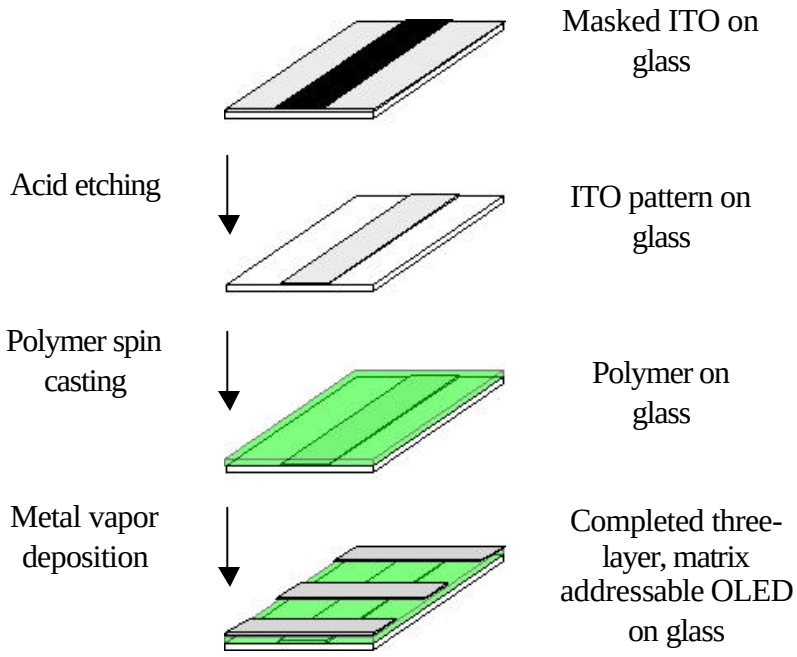

Figure 7.1 Step wise fabrication of multilayered organic polymer light emitting device sandwich structures.

LED structures were all initially fabricated using methoxy ethyl hexyloxy poly(phenylene vinylene) MEH-PPV as a conjugated polymer active layer to ensure that other work documented in the literature could be reproduced, and to substantiate that LED fabrication was indeed possible. It was only after perfecting device fabrication methods/protocols using MEH-PPV, that a more ambitious attempt was made to fabricate luminescent devices incorporating the less studied DPPE polymer as an active optoelectronic material. After the DPPE conjugated polymer layer was initially spin deposited, the film could then either be coated with an aluminum film to complete the LED sandwich structure and form a pristine DPPE device. For annealed devices, substrates could be subsequently thermally annealed at 200^{o}C and allowed to slowly cool (20^{o}C/min) before the final metal vapor deposition process. Both sets of sandwich devices, annealed and pristine, were fabricated for electroluminescent analysis. An aluminum cathode was vapor deposited over the polymer active layer through a shadow mask pattern to yield (typically in our lab) 4 sandwich LED structures per glass substrate in a matrix addressable configuration (Figure 7.1). In this manner, electrical short-circuits and other defects can be limited to only a portion of the entire glass chip and other, smaller, usable areas can still function independently. After a few months of practice the production of functional devices possessed a success rate that approached 75%. Upon device completion, each separate light emitting region possessed an active surface area of approximately 5 x 5 mm^2. Initial measurements of light emission were carried out on these basic structures to make sure that the experimental DPPE material was genuinely

electroluminescent, to examine the general viability of the thin film devices, and to research the stability of the devices under bias as a function of time. It was on these initial sandwich type devices that photoconductive behavior was first noticed with a simple pen light in a dark room, before later becoming of more significant experimental interest.

Description of Instrumentation Used for Device Electrical Characterization

A Keithley Model 2400 Sourcemeter was used for electrical data acquisition and to source voltage for experimental device operation. The sourcemeter is a versatile instrument capable of sourcing both voltage or current with great precision. Constant source values may be selected or more complicated ramping profiles can be employed during electrical analyses. In addition to acting as a reliable power source, the instrument may also function as a high quality digital multimeter. Measurements of external device resistance, current flow, and voltage drop can all be made with great precision and accuracy. The sourcemeter was specifically employed to source voltages for sandwich LED operation. The instrument is able to source voltages as well as make measurements of current flow simultaneously. Voltages ranging from 0 to 210 V could be sourced and accurate current measurements could be made into the tens of picoamperes range using the sourcemeter. Four-point measurements were not necessary when examining the LED structures because of the high resistivities and low power losses associated with the organic semiconductor devices. Simple mechanical connections were made to LEDs with the positive terminal of the sourcemeter being connected to the ITO anode layers of each device. In the same

manner, the circuit was completed by connecting the negative terminal of the sourcemeter to the metal cathode of each device. Sandwich luminescence data were taken with bias voltages ranging from 0 V to 30 V.

Description of Electroluminescence Collection

Electroluminescent spectra were collected from organic LEDs fabricated in a sandwich type configuration. The emitting device area was focused into a grating monochromator (Acton Research Corp. Model# 150) equipped with a CCD detector (Princeton Instruments Inc. Model# LN/CCD-1340) so that the entire spectrum could be collected simultaneously. Devices were biased at a voltage where electroluminescent emission could be seen in a dark room before attempting to collect electroluminescence spectra. The wavelength dispersion of the spectrometer was calibrated using 457.9 nm, 488.0 nm, 514.5 nm emission lines from and Argon ion laser source. After the calibration, the spectrometer was checked using a red 632.8 nm laser emission to assure calibration over the entire range of our experiment. Once the wavelength range of the spectrometer was calibrated, a NIST traceable light source was employed to acquire a calibration for the response of the detector over the selected wavelength range. Data over the range from 300 to 800 nm could be accurately collected using the fully calibrated spectrometer. Spectra were also unchanged with deviations in the mounting position of the device in the focal plane of the spectrometer from measurement to measurement.

SANDWICH LED RESULTS AND DISCUSSION

Electroluminescent spectra were collected from DPPE sandwich devices fabricated using both pristine and annealed active layers of the polymer films. Each device was run at the lowest possible bias voltage to detect visible light emission with the unaided eye and to minimize electrical/thermal stress on the delicate structures. This voltage was approximately 8 V for devices constructed using pristine DPPE layers and 15 V for devices employing annealed thin films. Both sets of devices produced a green luminescence that was easily seen within a darkened room. Device luminescence could be made to last for a period of a few hours using low operating voltages (<20V). Emission (as well as current flow) from the device appeared to be in a constant state of flux as the LED was operated at a stable operating bias. The intensity of individual light emitting areas within each LED appeared to fluctuate considerably with time and all devices appeared to be dynamic. Certain areas of the sandwich luminesced more strongly while others appeared less emissive. This behavior would often reverse and the device would exhibit the opposite behavior only seconds later; yielding a sparkle-type effect as the device was operated over time. This type of flickering behavior is witnessed until the device electrically shorts and ceases to be electroluminescent at any bias voltage (<3 hrs of operation). Electroluminescent spectra were acquired using various exposure times and no fluctuations in spectral response were witnessed with changes in the spectrometer integration time. Spectral signatures of the devices also remained unchanged with time. Spectra taken early

in the lifetime of the device were identical to those taken after the device had been operated for an extended period.

In examining device electroluminescence two significant features must be noted in the analysis of bulk DPPE device emission spectra. The first item of interest is the similarity of the two spectra obtained from devices employing films with different processing histories (Figure 7.2). This is completely unlike the behavior witnessed during studies of DPPE photoluminescence. The second item of significance results from the similarity of the spectra, not only to each other, but the overwhelming resemblance that the electroluminescent spectra exhibit to photoluminescent spectra collected from pristine, spin cast samples of DPPE. The key points of similarity are related to the broad featureless nature of the electroluminescent spectra as well as the presence of a significantly red shifted emission as compared with data collected from both solution phase and annealed films (Chapter 4) with photoluminescent emission maxima peaked above 500 nm.

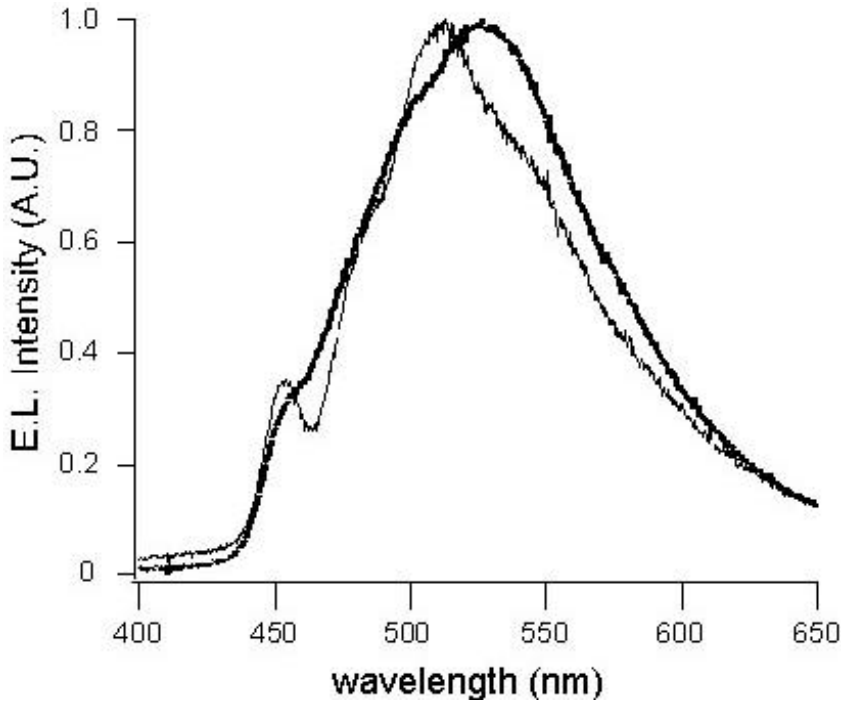

Figure 7.2 Electroluminescence measured from sandwich type light emitting devices fabricated using pristine (—) and annealed (?) films of di-dodecyl poly(phenylene ethynylene) as active layers.

The similarities witnessed between DPPE electroluminescent emission from both pristine and annealed sandwich LEDs as well as that of the pristine photoluminescent spectrum can be explained in terms of polymer chain associations on the molecular level. In Chapters 4 and 5, the transition of the broad green fluorescence spectra associated with pristine films of DPPE to the more structured blue emission found in annealed DPPE films is attributed to molecular relaxation and the structural limitation of excimeric close-associations. Thermal rearrangement of the polymer chains with even small increases in thermal energy enables polymer backbone relaxation and the breaking of the close

polymer associations necessary for excimer formation as well as for the broad green fluorescence emission. Similarly, the current electroluminescent studies indicate that thermal relaxation of the DPPE backbone structure can again be used to explain the luminescent behavior witnessed from pristine and annealed films of the material.

As in Chapters 4 and 5, the thermal relaxation of DPPE macromolecules results in an overall decrease in the concentration of closely associated interpolymer sites responsible for photoluminescent excimer emission. When considering electroluminescent devices, however, despite the reduction in these closely associated excimer sites results in spectral signatures that are always dominated by interpolymer excimer-type radiative relaxation. The similarity of the electroluminescent emissions from pristine and annealed samples indicate that DPPE electroluminescence is an excimer dominated process. This excimer dependent response lies in the fact that efficient electron/hole recombination may occur only at closely associated sites of overlapping polymer molecules. As these excimer sites are in high concentration in randomized pristine films, it is not surprising that electroluminescence is dominated by a broad green excimer-like emission. Since DPPE electroluminescence changes very little upon thermal reorganization of the films, it can be concluded that the same excited state species is responsible for light emission in thermally annealed films as well. A strong argument can be presented around the current collection of electroluminescent data, that defines excimer type polymer associations as imperative to electron/hole recombination and subsequently for efficient light emission. When

polymer films are allowed to relax to a lower energy glassy state upon thermal annealing, the concentration of excimer sites decreases significantly. As these closely associated sites become less prevalent in the glassy matrix, there are subsequently less sites where light emission can occur, leading to the trend witnessed where increases in bias voltages are necessary to elicit an electroluminescent response from thermally treated devices. This condition can be illustrated schematically in Figure 7.3. Electroluminescence from the well ordered sites in the polymer film is significantly reduced as poor electronic overlap occurs in these regions and interpolymer distances increase with reorganization in the sea of surrounding aliphatic side chains (Figure 7.3). If electrons are being injected from the left side of Figure 7.3, and holes are being injected from the right, the two carriers may only effectively combine at certain well associated molecular sites (circled).

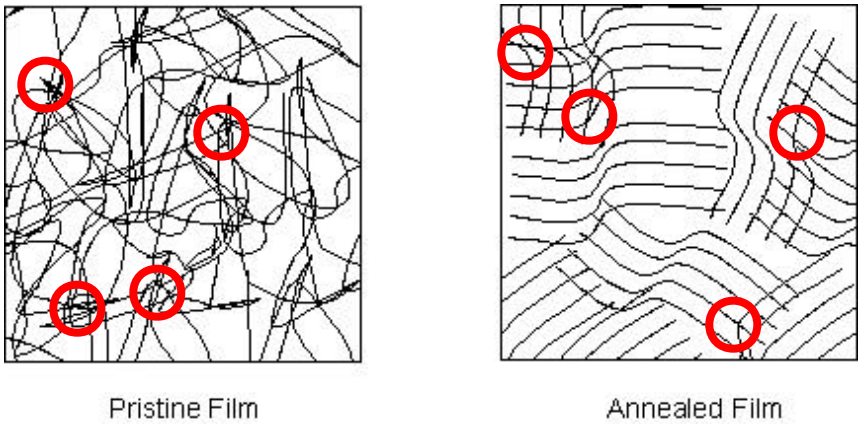

Figure 7.3 Schematic representation of closely associated molecular sites responsible for electroluminescent signature witnessed from light emitting devices fabricated using pristine and annealed di-dodecyl poly(phenylene ethynylene) thin films as active materials.

PLANAR GOLD/DPPE/GOLD OPTOELECTRONIC DEVICE STUDIES

The situations represented in the schematics of Figures 4.5 and 7.3 offer explanations as to why thermal annealing alters film photoluminescence substantially, while, at the same time, making only a minor impact on the electroluminescent signature of the condensed phase polymer. In an attempt to better understand the relationships between aligned polymer chains and the luminescence displayed by these optically active materials, it is necessary to devise an experimental configuration conducive to high resolution optical microscopy under standard LED operating conditions. To probe localized light emission and to make in situ observations of electroluminescent regions in organic semiconductor materials it is necessary to employ, not the typical sandwich structure, mentioned previously, but a modified planar device geometry. Encapsulation of polymer semiconductor active layers within typical sandwich-type electrode structures prevents rigorous optical characterization of these materials and ultimately hinder high resolution studies of local light emission. The modified geometry presented here is similar to that used by Buratto and Heeger. The basic experimental approach involves a single-layer planar metal electrode structure. Unlike previous efforts, however, the line gap is an order of magnitude more narrow (only 800 nm-1000 nm). This sub-micron scale line gap is constructed so that the orientation is normal to the substrate surface (Figure 7.4).

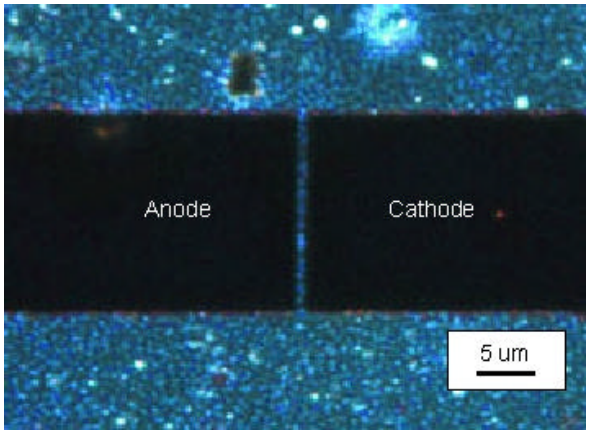

Figure 7.4 POM micrograph of annealed di-dodecyl poly(phenylene ethynylene) thin film deposited across a 1 um line gap in a symmetric gold electrode/polymer/gold electrode light emitting device.

These planar devices can be employed and directly used to probe localized regions of polymer light emission and charge separation using high resolution optical microscopy. Direct control of the planar electrode dimensions, and the gap between them, also allows for manipulation of the overall electrical response of the planar optoelectronic device. The fabrication of each planar electrode device employs multiple steps requiring proficiency in techniques ranging from organic thin film deposition to nanoscale focused ion beam milling.

The planar electrode device fabrication begins with the deposition of a thin layer of gold onto an insulating glass support structure. Sputter coating of a 100 nm thick layer of gold onto a glass microscope slide yields a uniform smooth metal surface with acceptable adhesion properties to prevent delamination of the gold from the glass. The metal film provides an adequate medium for electrode fabrication in a top-down etching procedure. Once the metal layer has been deposited it becomes necessary to use a photolithographic process to produce a 40

um wide gold bridge from the initial gold film layer. This bridge structure provides a practical balance in device dimensions, allowing both a small bridge structure for further micro-scale milling processes, as well as larger contact pads that can be manipulated and connected without the practical complications stemming from working with microscopic electrical connections.

Positive resist photolithography provides a straight forward method for producing the 40 um-wide conductive electrode bridge. The bridge will eventually be etched to produce two separate gold electrodes possessing a line separation less than a single micron. The photoresist procedure first requires the deposition of a micron thick coating of positive photoresist over the metal base layer. The polymer is deposited via spin casting to yield a surface coating of uniform thickness. The layered gold/photoresist structure is then briefly cured in a 90^{o}C oven for 5 min to set the photoresist and ensure adequate surface adhesion to the substrate. Next, a photomask with the appropriate bridge pattern to be replicated is selected and placed over the photoresist-coated gold film. The mask/film combination is then exposed with 1000 watts of unidirectional UV radiation for 5 min to form a latent image of the selected bridge structure in the photoresist film. The region of the photoresist exposed to the UV radiation possesses greatly enhanced solubility in organic solution, as compared with that of the unexposed regions. At this point, the latent image is developed with photolithographic developing solution and only the regions of the photoresist shadowed by the bridge structure mask are left undissolved. The resulting photoresist pattern is then further thermally crosslinked at 120^{o}C for 5 additional

minutes to provide a robust organic protective layer over select regions of the gold film. After allowing the structure to cool under ambient conditions back to room temperature, the gold/photoresist structure is placed into a concentrated KI solution that functions as a gold metal etchant. The solution etches away the areas of the gold film not protected by the crosslinked photoresist to leave a copy of the bridge structure from the original photomask pattern. Additional rinsing of the structure in pure acetone removes the residual photoresist protective layer to yield a bare gold metal bridge on a supportive glass substrate. The bridge structure is then suitable for further processing into two free-standing gold electrodes.

Once an adequate bridge structure has been produced it is necessary to form two separate electrodes via an ion beam milling procedure. The etching of the tiny channel that divides the bridge into electrodes is carried out using a dual electron/focused ion beam system (FEI Strata DB235). Good electrical contact has to be maintained between the sample and ground to ensure precise milling. Similar to scanning electron microscopy (SEM), excess static charge accumulation on the sample surface caused by Gallium ion bombardment renders imaging and milling difficult so that the sample must be thoroughly electrically grounded. Employing the focused ion beam to remove material from the metal bridge to create two free-standing electrode structures eliminates variations in line separations that may occur with photolithographic techniques on this small distance scale. The severe aspect ratio of the gap feature (50 or 100 to 1) to be rendered also makes lithographic etching difficult (not impossible, though).

Small variations in spin cast photoresist thickness can cause significant defects when chemically etching the small line gap. For these reasons, the electrode line gap is generated with a focused ion beam mill with a cutting resolution approaching 50 nm. With the focused ion beam, device-to-device reproducibility is enhanced, electrode geometry variations are limited, and structural symmetry is maintained in the final two-electrode configuration. One major issue causing concern when employing any ion beam technique, however, is the extent with which the high-momentum cations are incorporated into the substrate. If significant ion implantation occurs, it can have profound effects on electrical conductivity and device performance. Gallium ions are known to implant efficiently into crystalline silicon used in semiconductor applications but their doping in the current application appears low as there is no evidence of any appreciable conductivity in the planar open circuit device. In fact oxides of silicon are typically used as masks to ion implantation in semiconductor device fabrication.

After the metal electrode structure has been fabricated using both photolithographic and ion beam milling procedures, the device is ready to be spin cast (or drop cast) with conjugated polymer solution (0.5 wt% DPPE in chloroform). Spin casting the solution at 2000 RPM yields smooth uniform pristine polymer thin films of ~70 nm in thickness over the 100 nm thick gold electrodes and across the inter electrode spacing. The completed glass chip structure is subsequently placed under vacuum for 1 hr to remove any residual casting solvent and ensure limited conductivity due to residual surface moisture.

The samples may also be thermally annealed at this juncture. Once the chip is adequately dried it is mounted into a home built chip holder that allows electrical connections with the small chip contact pads to be made. Mechanical contacts are reinforced with silver paste to provide excellent electrical conductivity between the voltage source and the micro electrode system. Both photoconductivity and light emission studies can be conducted using the resulting planar metal/conjugated polymer devices.

Photoconductivity Investigated in Planar DPPE Devices

Two-point measurements of the device could be made because negligible power is dissipated by the small device. When characterizing the small organic semiconductor junctions, voltage is sourced and current flow can be measured simultaneously with the sourcemeter. Source voltages from 0 to 210 V are accessible with the unit. The instrument also enables accurate measurements of current flow with high sensitivity and a limit of detection extending into the pico amp range. All initial studies examining device conductivity were carried out under an inert nitrogen atmosphere. Far-field measurements of photoconductivity induced in the small electrode gap were attempted initially to identify and quantify the photoresponse of the device. Photoconductivity measurements of functional micro scale planar metal-polymer-metal devices were made using the lamp source of an Olympus microscope in an epi-illumination geometry (10 W) and the sourcemeter. Devices were fabricated by depositing a 70 nm layer of DPPE over the electrode gap. The resulting amorphous films span the electrode junction and produce a smooth uniform surface as determined with AFM,

indicating good adhesion and adequate electrical contact. Dark current measurements of these devices yielded significant values but a small photoresponse could still be measured under intense white light illumination. With the small line gaps separating the electrodes of the planar devices, only small bias values (<5 V) were required to elicit current flow in the symmetric gold structures. The small interelectrode spacing creates a situation where a large field strength exists at the polymer junction. Dark current measurements from devices fabricated using pristine spin cast films are significant and only a small change in current flow is measured under high intensity halogen illumination (Figure 7.5).

Similarly, identical planar metal-polymer-metal junctions were fabricated using thermally annealed films of DPPE. In these devices, the films were initially spin cast at the junction and then annealed directly on the glass device support structure. AFM analysis of these devices indicated little change in surface roughness or thickness of the film as compared with measurements made on those fabricated from pristine DPPE films. No delamination or mechanical trauma was evident at the interfaces between the microelectrodes and the polymer phase following the annealing process. Dark current measurements from these annealed devices were substantially lower than those of their pristine counterparts. With increased bias, however, the films demonstrated far superior photoconductive response with values approaching an order of magnitude improvement over those witnessed from devices employing pristine active layers.

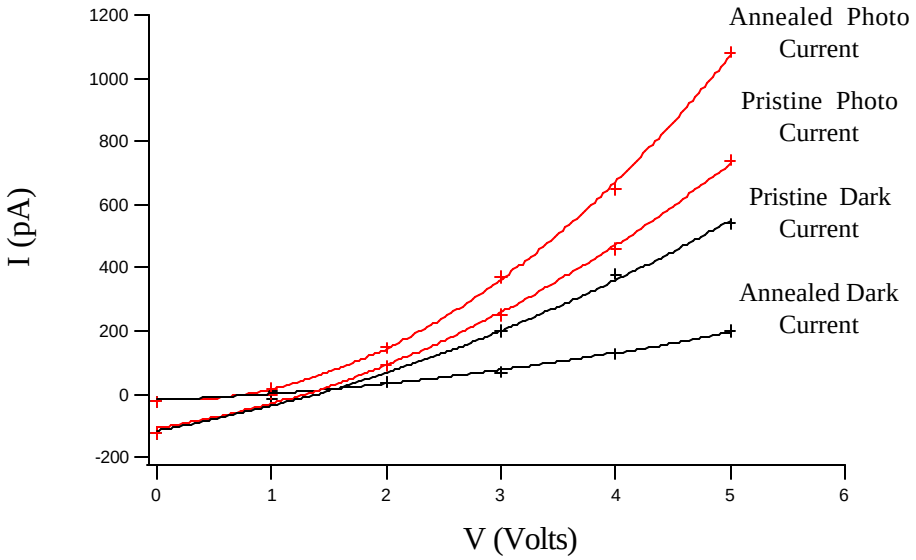

Figure 7.5 Photoconductivity measured under ambient conditions from planar devices fabricated using pristine and annealed DPPE active layers. The dark current is decreased and the photoconductive response increases in devices made from annealed films.

Difficulties arose, however, upon introduction of the polymer devices into an evacuated environment. Experiments attempted in an evacuated cryostat were unsuccessful in measuring photoconductivity or mapping stable/reproducible current-voltage relationships. This observation creates concern that the photoconductivity data collected previously under a nitrogen atmosphere may be intimately coupled to surface vapor or the presence of a volatile contaminant and may not be a true measure of the photoconductive response of the polymer.

High-Resolution Imaging of Planar DPPE LEDs

A typical bare planar device structure lacking any polymer dielectric was used for open circuit measurements. A constant open-circuit current (~150 pA) was measured until a violent ablation of the thin metal bridge occurred above 170

V. At this high electric field the metal bridge electrically short circuited, became a filament, and glowed brightly for a moment before being destroyed in a firey corona. After the destructive event, the electrodes were effectively ablated and the device was not able to be used for further studies. It was witnessed that the onset of this ablation event could be delayed until higher voltages if the sample was kept within an evacuated cryostat. The remainder of the studies conducted upon light emission from planar devices were all subsequently carried out in such an evacuated environment at liquid nitrogen temperatures.

Light emission from planar DPPE devices was observed under the following conditions. A bare gold planar electrode structure with an 800 nm line gap was spin cast with DPPE from organic solution (0.5 wt% DPPE in chloroform). This sample was then wired into a cryostat with an optically transparent window so that the polymer deposited across the interelectrode spacing could be observed (Figure 7.6 upper). The cryostat was evacuated for 1 hour at room temperature before cooling the system to liquid nitrogen temperatures at 10^{o}C/min. Extended pumping time was employed to eliminate any volatile components that may condense onto the electrodes at colder temperatures. Following cryostat cooling, the device bias was ramped from 0 to 130 V at ~5 V/sec. At a voltage of 130V, bright green light emission could be observed from the interelectrode gap of the device (Figure 7.6 lower). Interestingly, the entire electrode gap did not become illuminated and only preferential sites exhibited light emission. The areas that were luminescent seemed unstable with time and demonstrated similar flicker-type behavior to that

witnessed in sandwich LEDs. Current readings also fluctuated substantially in devices held at constant voltage, indicating dynamic changes in device conductivity/morphology with time. Pristine and annealed films of DPPE exhibit identical electroluminescent behavior.

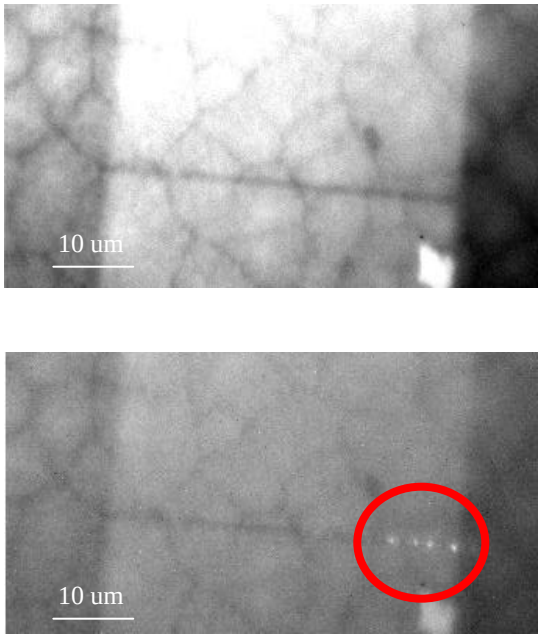

Figure 7.6 A monochrome fluorescence image of an annealed film of di-dodecyl poly(phenylene ethynylene) deposited over an 800 nm line gap separation (top). Light emission elicited from the device at a bias of 130 V (5 second integration time) is overlaid on the fluorescence image in the lower micrograph. Electroluminescence can be viewed to originate at the device cathode.

The polarization dependence of electroluminescence emitted by planar devices fabricated using annealed films of DPPE was investigated in an attempt to better understand light emission as a function of polymer chain order. Device emission was collected at two orthogonal polarizations using a simple polarizer.

No definitive change in luminescence efficiency was observed between the two polarizations. Certain areas did exhibit changes in electroluminescent intensity but this is most likely attributable to the general instability of light emission from the small luminescent regions. No trend was observed indicating that regions of the polymer oriented in a certain direction lended themselves to more efficient light emission. This result from devices made with annealed DPPE films, coupled with identical data collected from measurements of pristine planar LEDs, is further evidence suggesting that polymer organization is secondary to interpolymer close-associations as the mechanism most responsible for efficient electron hole recombination.

Another interesting feature observed in planar DPPE devices, is the asymetry of the electroluminescence from the interpolymer spacing. By changing device polarity, it is apparent that polymer light emission always occurs preferentially near the cathode of the metal-polymer-metal junction. This asymmetry can be attributed to the differing efficiencies of electron and hole injection from the gold electrodes and the unequal mobilities of the charge carriers within the polymer. These results agree with those observed in MEH-PPV literature.[10]

Toward Near-field Photoconductivity Measurements of Aligned Polymer Films.

Preliminary work was completed examining the viability of measuring localized photoconductivity in thermally annealed films of DPPE. Planar DPPE devices could be positioned on the NSOM scanning stage and the interelectrode spacing could be found with the NSOM tip. A tip with a large aperture (300 nm

diameter) was employed to examine if photoconductivity at the metal-polymer-metal junction could be detected. Annealed films of DPPE were chosen for NSOM studies because of increased photo response compared to pristine films and the presence of well order meso domains.

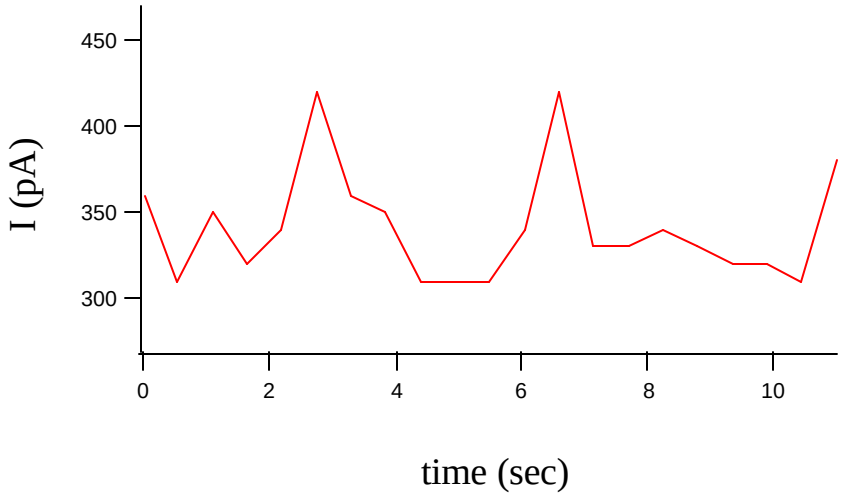

Figure 7.7 Photoconductive response measured with a 300 nm diameter NSOM aperture and 400 nm excitation. Photoconductivity could be measured when the NSOM tip was positioned over the electrode gap at t=3 and 6.5 seconds. The line gap in the electrode structure was 1 um and the bias voltage was set at 5V.

Increased conduction could be easily identified in scans of the electrode gap in the presence of 400 nm excitation light (Figure 7.xx). However, this photoconductive response may be greatly depended upon surface contamination or other atmospheric parameters, as all NSOM studies are conducted under ambient conditions. Even with the current experimental complications, the ability to collect high resolution, correlated morphological/photoconduction images of ordered DPPE samples looks promising. Fluorescence polarization NSOM

methods could be employed to locate and identify regions of polymer chain order in the sample while simultaneously collecting high resolution photoconductivity measurements using the NSOM probe as a localized illuminations source. These measurements may offer further insight into polymer chain alignment/carrier separation or polymer chain alignment/light emission relationships.

CONCLUSION

We have been able to definitively measure electroluminescence from polymer films of DPPE with different thermal processing histories. Electroluminescent spectra were collected from sandwich OLEDs fabricated using both pristine and annealed films of DPPE. The similarities witnessed between the electroluminescence elicited from each set of devices and the fluorescence measured from pristine DPPE films is strong evidence indicating an excimer mediated process responsible for light emission in devices. Results from Chapters 4 and 5 indicated that thermal relaxation in DPPE films leads to a decrease in the amount of sites available for excimer formation. When these closely associated sites are disrupted under polymer chain relaxation, it eliminates areas where efficient electron/hole recombination may occur and leads to a decrease in device quantum efficiency. This reduction in quantum efficiency is easily observed by the increase in device bias required to elicit electroluminescence from thermally annealed DPPE films.

In order to confirm that light emission is significantly controlled by the presence of excimer type molecular associations, a series of experiments were undertaken examining direct light emission from a series of planar gold-polymer-

gold devices. The observation that device emission was not uniform across the polymer gap and possessed little dependence upon polymer chain order is strong evidence for an excimeric electroluminescent species. Rather than observing well polarized emission from regions of the sample possessing significant interpolymer order oriented parallel or perpendicular to the applied electric field, isotropic emission from only a few select sites is witnessed. The asymmetric profile of light emission from the planar devices is indicative of unbalanced carrier injection/mobility in the model system. Severe quenching of the excited state species at the cathode can be effectively ruled out by considering the results presented in Chapter 6.

Further experiments determining the viability of probing localized regions of polymer sample photoconductivity using NSOM are also described. Unfortunately complications concerning photoconductivity and the possible dependence of this phenomena on surface vapor or other environmental contaminants has hindered further advances in this area, although the experiment should not be dismissed as impossible.

ACKNOWLEDGEMENTS

The author would like to thank Dr. Keith Stevenson at the University of Texas at a Austin for access to the Nikon microscope used to image the planar DPPE devices as well as assistance with using the imaging software. He would also like to acknowledge Sungwook Kim for assistance concerning metal sputter coating and photolithographic procedures developed in the McDevitt Research Group.

REFERENCES

1. Brown, A. R.; Greenham, N. C.; Burroughes, J. H.; Bradley, D. D. C.; Friend, R. H.; Burn, P. L.; Kraft, A.; Holmes, A. B. *Chem. Phys. Lett.* **1992**, *200*, 46.

2. Friend, R. H. *Synthetic Metals* **1992**, *51*, 357.

3. Granstrom, M.; Petritsch, K.; Arias, A. C.; Lux, A.; Andersson, M. R.; Friend, R. H. *Nature (London)* **1998**, *395*, 257.

4. Yu, G.; Pei, Q.; Heeger, A. J. *Appl. Phys. Lett.* **1997**, *70*, 934.

5. Scott, J. C.; Brock, P. J.; Salem, J. R.; Ramos, S.; Malliaras, G. G.; Carter, S. A.; Bozano, L. *Synthetic Metals* **2000**, *111-112*, 289.

6. Yu, G.; Zhang, C.; Heeger, A. J. *Appl. Phys. Lett.* **1994**, *64*, 1540.

7. Luo, F.-T.; Tao, Y.-T.; Ko, S.-L.; Chuen, C.-H.; Chen, H. *J. Mater. Chem.* **2002**, *12*, 47.

8. Singh, J. Semicondcutor Devices: Basic Principles **2001**.

9. Cao, Y.; Yu, G.; Heeger, A. J. *Adv. Mater.* **1998**, *10*, 917.

10. Lemmer, U.; Vacar, D. M., D.; Heeger, A. J.; Ohnishi, T.; Noguchi, T. *Appl. Phys. Lett.* **1996**, *21*, 3007.

11. DeAro, J. A.; Moses, D.; Buratto, S. K. *Appl. Phys. Lett* **1999**, *24*, 3814.

12. Lee, H. M.; Oh, D. K.; Lee, C. H.; Lee, C. E.; Lee, D. W.; Jin, J.-I. *Synthetic Metals* **2001**, *119*, 473.

13. Brinza, M.; Adriaenssens, G. J.; Roca, P.; Cabarrocas, P. R. I. *Thin Solid Films* **2003**, *427*, 123.

14. Liu, J.; Shi, Y.; Yang, Y. *Appl. Phys. Lett.* **2001**, *79*, 578.

15. Liu, J.; Shi, Y.; Ma, L.; Yang, Y. *J. Appl. Phys.* **2000**, *88*, 605.

Chapter 8: Standard Sample Characterization of Near-field Scanning Optical Microscopy (NSOM) Probe Apertures.

CHAPTER SUMMARY

A quick, cost effective, semiquantitative means for gauging the quality of near-field scanning optical microscopy (NSOM) probe apertures has been demonstrated by employing a nanoperforated thin metal film standard sample. Small 182 nm holes were created by evaporating gold over dispersed latex spheres with subsequent removal of the spheres. The size of the NSOM aperture can be determined from a deconvolution of the image size and the known sample size and geometry. Results from the standard correlate well with aperture size measurements made from scanning electron micrographs.

INTRODUCTION

Near-field scanning optical microscopy (NSOM) is a versatile scanning probe technique that, through the implementation of a small aperture, is able to provide correlated topological and optical information with higher resolution than that achievable with conventional microscopic approaches.[1-8] In conventional far-field microscopic techniques using lens systems, resolution is limited by the diffraction of the probe radiation as demonstrated by Abbe and can be approximated as half the wavelength of light, or a few hundred nanometers, for visible regions of the spectrum. NSOM can achieve resolution superior to far-field methods by illuminating the sample through a small aperture. In modern NSOM, a single-mode optical fiber is pulled or etched to a fine point that is then

shadowed with an opaque metal coating leaving only a 50-100 nm circular aperture at the probe apex allowing light propagation.[4,5] The intense electric field produced at the apex of the coated waveguide remains confined to the NSOM aperture for only a short distance (on the order of half the diameter of the aperture) and this region is termed the near-field.[6-7] This phenomenon proves to be of great advantage in imaging, as optical resolution in the near field becomes independent of source wavelength and is defined only by the size of the NSOM aperture.[8] By confining the incident electric field at the tip with the tiny NSOM aperture, it is possible to break the conventional diffraction limit and extend optical resolution to impressive limits of $\lambda/6$ or better (50-100 nm). Resolution approaching 30 nm has been demonstrated.[9] Imaging is achieved by raster scanning the sample in a noncontact scheme beneath the NSOM aperture. Shear force is employed to keep the piezoelectrically controlled scanning stage in an electronic feedback loop to maintain the proper sample/tip separation.[10] In this way, a topographic map of the sample surface is obtained simultaneously with valuable optical information during two-dimensional raster scanning.

In the decade since its inception, NSOM has become widely used in materials science and biological research. The versatility of NSOM to be used in transmission, reflection, polarization, and fluorescence modes allows for a plethora of samples to be optically characterized on the nanoscale.[2, 6, 8, 9, 11-16] One major drawback accompanying NSOM analysis, however, stems from the difficulty associated with adequate tip aperture characterization. Often tips possessing diameters larger than 200 nm or tips that have been damaged will still

yield optical features that appear to be smaller than diffraction limited.[17] These small artifacts can lead to confusion during data interpretation and result in erroneous optical characterization of samples. Because of this ambiguity, it is of paramount importance to definitively measure the NSOM aperture in order to verify that the instrument is indeed functioning in a subdiffraction-limited capacity. A well characterized aperture is also essential when modeling tip/sample field interaction and devising experimental simulations.[3, 18]

Numerous techniques have been used to try and make meaningful measurements of NSOM tip aperture size. The most common and accepted procedure for accurate near-field tip characterization employs scanning electron microscopy (SEM).[2, 8, 19] The imaging of a sharpened metal probe with SEM, however, remains not only difficult but destructive. General positioning requirements of the electron microscope mandate that the NSOM fiber be clipped short and mounted in a geometry pointing directly into the imaging electron beam. Another complication arises due to oxidation of the aluminum coating of the near-field probe. Aluminum-coated tips oxidize quickly under ambient conditions so that poorly conductive aluminum oxide covers the outer surface of the probe. Since static electric charge accumulates at the non-conductive aluminum oxide tip apex, the probe must be delicately covered with conductive paint to minimize static charging that is detrimental to clear SEM imaging. Neglecting to ensure good conduction and attempting to image a probe in a nondestructive manner leads to poor images that cannot be used for quantitative analysis. The numerous complications associated with SEM analysis often result

in ambiguous micrographs that lead to inconclusive measurements of NSOM tip aperture sizes, making the technique costly and cumbersome for quantitative work. Yet another approach for tip aperture characterization using fluorescent single molecules to effectively map the near-field aperture has also been attempted.[20] Single molecules have been employed to allow optical contrast without introducing topology that produces scanning artifacts. This method requires the examination of numerous molecules to account for polarization effects introduced by the random orientation of the single transition dipoles of each probe molecule. While extremely effective, the technique is demanding and remains far from a routine method for simple probe aperture measurements. Another common means of NSOM probe characterization involves the use of a uniform antisphere array.[21] The array consists of triangular metallic features that are left behind when a metal film is vapor deposited over an array of close-packed latex spheres on a glass matrix and the spheres are later removed. The remaining regular pattern is easily found and identified but the small metal features possess pronounced topography and produce only minimal optical contrast, presenting only a qualitative measure of NSOM aperture size. Finally, the most basic means of analysis is to examine the NSOM fiber using conventional far-field microscopy. Simple observation of the tip coupled to a laser source under a high numerical aperture objective can be used to make a rudimentary approximation of tip quality but it is impossible to quantitate a subdiffraction-limited feature with a diffraction-limited microscope.[22] Although it is possible to identify tips with extremely large apertures, the method remains unreliable in determining which

tips have large apertures or merely superior light throughput. Recent work in our lab has focused on the fabrication of a quantitative standard sample that can be scanned in a preliminary fashion to easily characterize a given NSOM aperture before other samples are imaged. Criteria for an ideal standard sample that were addressed included: minimization of topography to limit scanning artifacts, creation of small uniform optical features that could be used to quantitate the NSOM aperture, as well as incorporation of easily identified and imaged optical features to simplify and expedite the characterization process. The most vital requirement was to employ a contrast agent that could be used in a transmission mode configuration so that the standard sample could be used with any NSOM instrument.

EXPERIMENTAL

Standard sample preparation

The standard sample was prepared by uniformly dispersing latex nanospheres (182 nm diameter Polysciences) over a glass substrate in a surface concentration of approximately 0.25 nanospheres/ um^2. A 10^{-3} aqueous dilution of the stock sphere solution was deposited on to a glass coverslip with an equal volume of aqueous Triton X-100 solution (~0.25 wt %) to ensure that the spheres did not appreciably form multisphere aggregates on the substrate surface. A thin gold film (~20 nm thick) was then vapor deposited over the combined substrate/sphere system. The polymer spheres were removed from the metal layer by briefly soaking the samples in solvent grade dichloromethane or methanol.

Treatment with the common organic solvents ultimately yielded a smooth nanoperforated metal film on a transparent glass support structure.

Characterization of sample perforations with atomic force microscopy

Tapping mode atomic force microscopy (AFM) (Digital Instruments Nanoscope IIIa) was employed to measure the size of circular cavities left within the smooth nanoperforated sample by the dissolution and removal of single latex nanospheres.

Characterization of near-field scanning optical microscopy probe apertures

The nanoperforated standard was scanned using transmission NSOM (Chapter 3) using pulled aluminum-coated tips fabricated in-house using single-mode optical fiber probes. The tips were mounted on 100 kHz piezoelectric tuning forks in order to maintain electronic feedback and regulate tip/sample separation. 10 um scans were taken initially to locate perforations in the metal film, while actual measurements of optical features were made on higher magnification 2 um images with 10 nm image pixels. The NSOM piezostage was calibrated on the 2 um scale using an AFM calibration grid with 463 nm spacings. Quality tips were fabricated on a micropipette puller (Sutter Instrument Co. Model P-2000) using instrument parameters that gave sharp fibers with impressive light throughput before being coated with ~200 nm of aluminum metal. These tips were then used for imaging the nanoperforated gold standard sample. Damaged tips with larger apertures were also used for imaging to give data over a range of tip diameters. All tips used for NSOM scanning were also

imaged using high-resolution SEM (LEO Model 1530) to give a second, independent, measure of the NSOM tip aperture diameter.

RESULTS AND DISCUSSION

Shear-force NSOM and AFM measurements indicate that the deposited thin gold film possesses peak-to-peak roughness of <10 nm. The dissolution of single latex nanospheres yields uniform circular perforations in the smooth film with reproducible diameters of 182 nm (Figure 8.1).

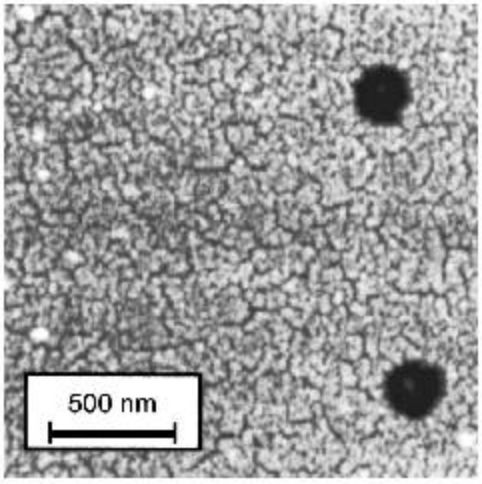

Figure 8.1 2 X 2 um tapping mode AFM micrograph of nanoperforated 20 nm thick gold standard sample. 182 nm latex spheres have been removed to leave dispersed uniform 182 nm circular perforations in the smooth flat metal matrix.

These small perforations, when imaged with a given NSOM probe, give an image that can be analyzed to reveal the true tip aperture diameter. Adequate contrast in NSOM imaging was provided by the thin metal film and the small uniform features were easily found and imaged using NSOM to give quality topographic and optical images (Figure 8.2A). The thickness of the metal film

was chosen due to the ease with which nanospheres could be removed to leave circular cavities. Smooth regions of the sample, away from areas containing residual undissolved spheres and surface defects, were used for quantitative analysis to minimize complications from topological artifacts. The perforations yielded bright cross-sectional profiles in the near-field optical image that were modeled well with Gaussian fits (Figure 8.2B and 8.2C).

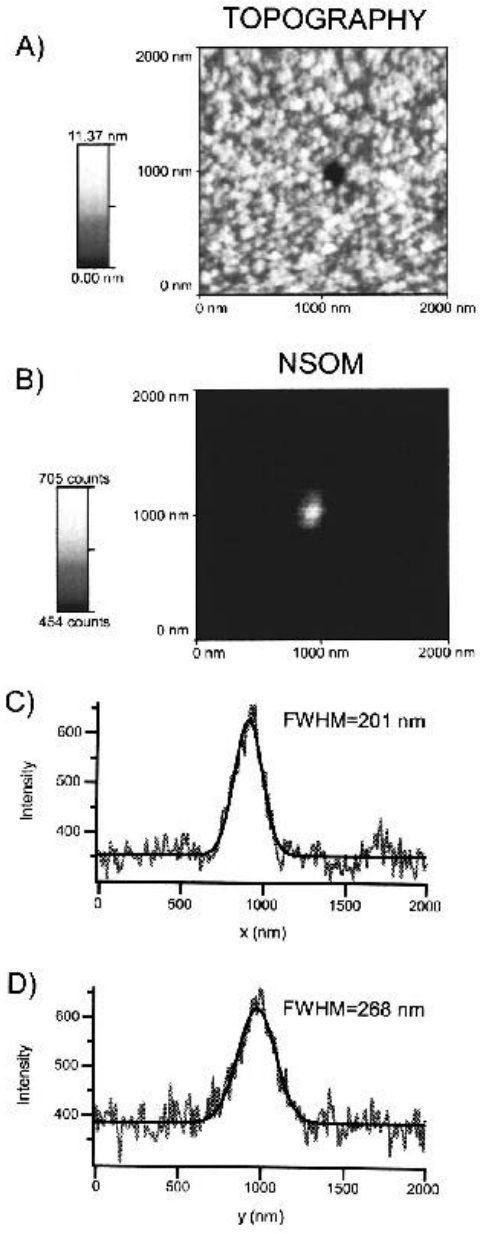

Figure 8.2 Topographic image (A) and optical image (B) from 2 X 2 um NSOM scan of a flat gold standard containing a 182 nm perforation. FWHM measured from the best Gaussian fits to NSOM line scans along the short and long axes of the optical transmission profile (C and D).

This is an approximation of the fields calculated using methods developed by Bethe and Bouwkamp that proves both quick and reproducible. The full width half maximum (FWHM) of the fits were then interpreted as the diameters of the optical features. The resulting Gaussian model represents a linear convolution of the NSOM instrument transfer function with a function representing the nanoperforation in the standard sample. The linear convolution integral:

$$f(x) * g(x) = \text{int}[f(x- x') g(x')]dx' \qquad (8.1)$$

simplifies in the case that the instrument transfer function, the sample perforation, and the measured NSOM image are all modeled with normal fits to:

$$(\text{image diameter})^2 = (\text{tip aperture diameter})^2 * (\text{perforation diameter})^2 \qquad (8.2)$$

Using this function allows for the straightforward calculation of the NSOM tip aperture diameter. Attempting to treat the transmission of the nanoperforation as a more intuitive step function (or hat function) and linearly convolving this function with a Gaussian instrument transfer function yields a non-Gaussian result that does not correlate well with our experimental data. In an approach using the full-Gaussian model it is possible, by knowing the FWHM of the image produced upon near-field scanning, to deduce the tip aperture size by knowing only the size of the nanoperforation in the metal film. Theoretically, the technique works most effectively when the feature being imaged is much smaller than the actual tip aperture (approaching a point source) but the deconvolution approach works for other tip/feature size combinations as well. The current method is quantitative for NSOM tip apertures with sizes down to ~90 nm. Once this lower limit is achieved, the technique becomes only qualitative in identifying high-resolution

NSOM probes. Very small transmission features may prove practically unsound in the current standard sample motif as very small spheres would prove extremely difficult to disperse and remove from the metal film and light throughput will decrease rapidly with perforation diameter, making image contrast less pronounced and analysis much more labor intensive. The current metal standard sample, however, remains unperfected and significant improvements in image contrast may be achieved by using different contrast agents and metals of different thicknesses to optimize uniform feature production while at the same time maximizing transmission contrast.

Although the diameter of the perforations is comparatively large with respect to the near-field aperture, it is adequate for making a semiquantitative determination of tip size. The correlation between image size and tip diameter makes it possible to easily determine aperture diameters over a wide range of values (Figure 8.3).

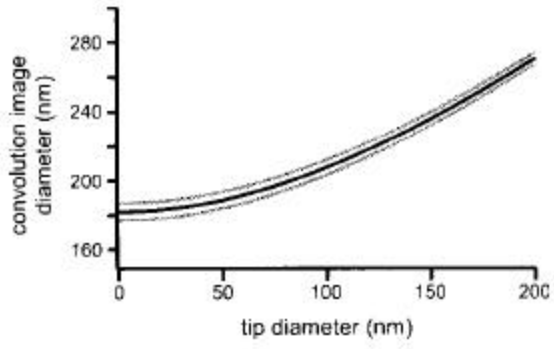

Figure 8.3 Calculated NSOM image diameter from linear convolution of 182 +/- 5 nm perforation with a given tip aperture diameter. The flattening of the convolution function at tip diameters <100 nm makes aperture quantitation difficult in this small-aperture range but the sample can still be employed as a diagnostic tool to confirm subdiffraction-limited imaging.

As the shape of the curve in Figure 8.3 begins to flatten at image diameters approaching the size of the perforation, it becomes more difficult to quantitate the probe size. Most importantly, definitive measurements can be made, even in the flat region of the curve, to identify probes with diameters less than 100 nm that will be suitable for high-resolution imaging. In the current study, tips were prepared in various ways to yield apertures ranging from 50-250 nm in diameter. The standard sample clearly reveals any asymmetry in the aperture geometry as shown in Figure 8.2B. This asymmetry is most important when considering polarization effects and will help in the selection of probes with circular apertures for rigorous polarization applications.

Measurements of aperture diameters taken using high-resolution SEM micrographs were difficult to make reproducibly and proved even harder to quantify with any meaningful confidence limits due to complications associated with static charge build up at the metal tip and other questions concerning light transmission through thin regions of the aluminum coating near the tip apex (Figure 8.4).

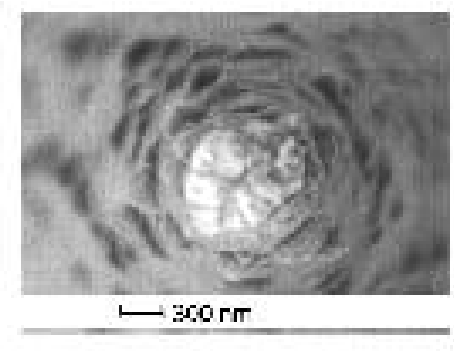

Figure 8.4 A typical SEM micrograph of the end of a metal-coated NSOM probe. Characterization of the tip aperture remains subjective and leads to wide variations in tip measurements.

Thin regions in the aluminum coating of the probe would appear similar to the rest of the aluminum skin under SEM observation, but light leakage through these thin areas can be easily seen using the current standard sample. Gaussian modeling and image deconvolution using the in-house standard sample predicts tip aperture diameters that are comparable with rudimentary measurements made using SEM (Figure 8.5).

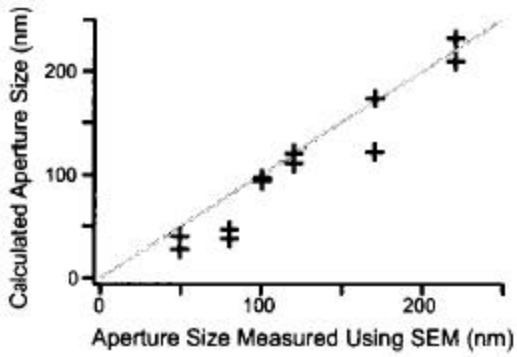

Figure 8.5 Tip aperture diameter measured using nanoperforated standard sample plotted against measurements made from SEM micrographs. The line illustrating when the two measurements are identical is provided as a guide for the eye. Aperture diameters <100 nm yield NSOM images approaching the size of the nanoperforations in the standard. Errors in measuring these small differences lead to the deviation from the line below 100 nm. Although these small apertures cannot be quantified, it is obvious that the probes are functioning in a subdiffraction-limited capacity and are adequate for true near-field analysis. The deviations between the two types of measurements are explained by ambiguous characterization of SEM micrographs.

Deviation of measurements made using the standard sample from those made using SEM is much more of a commentary on the limitations of measurements made from ambiguous SEM micrographs than on the effectiveness

of the demonstrated standard sample. Figure 8.5 illustrates that larger apertures are more easily quantified using SEM and measurements agree well with those made using the standard sample, whereas, smaller apertures become harder to characterize and deviate from values attained using the standard. The standard can be routinely scanned to yield reproducible results.

CONCLUSION

Until now, NSOM has proven to be a powerful analytical tool but for the most part has remained largely qualitative. Accurate imaging of nanoscale sample regions has been complicated by artifacts introduced by unknown tip geometries. The current sample allows for the accurate determination of the size and shape of the electric field confined at the near-field aperture and consequently enables the semiempirical calculation of nanoscale domain sizes in other samples of interest. In the current project, we have minimized topographic artifacts and produced an easily employed standard sample that allows for the direct mapping of the confined electric excitation field at the near-field probe apex. The standard sample indicates definitively, through direct observation, the area of a sample under the near-field aperture that interacts with the confined electric field and in so doing reveals the true optical resolution of the observed tip. Further work in this area optimizing the optical transmission and contrast of the standard sample by altering the thickness of the opaque film as well as the film material may prove beneficial.

ACKNOWLEDGEMENTS

The author wishes to thank Sungwook Kim of the McDevitt Research Group at the University of Texas at Austin with the gold deposition necessary for standard sample fabrication.

REFERENCES

1. Betzig, E.; Trautman, J. K.; Harris, T. D.; Weiner, J. S; Kostelak, R. L. *Science* **1991**, *251*, 1468.

2. Hsu, J. W. P. *Mater Sci. Eng. Reports* **2001**, *33*, 1.

3. M. A. Paessler and P. J. Moyer, Near-field Optics: Theory, Instrumentation and Applications, Wiley, New York, **1996**.

4. Buratto, S. K. Curr. Opin. Solid State Mater. Sci. **1996**, *1*, 485.

5. Van Hulst, N. F.; Veerman, J.-A.; Garcia-Parajo, M. F. *J. Chem. Phys.* **2000**, *112*, 7799.

6. Zenobi, R.; Deckert, V. *Angew. Chem. Int. Ed. Engl.* **2000**, *39*, 1747.

7. Zhou, R.; Midha, A., Mills, G.; Donaldson, L.; Weaver, J. M. R. *Appl. Phys. Lett.* **1999**, *75*, 1824.

8. Dunn, R. C. *Chem. Rev.* **1999**, *99*, 2891.

9. McNeill, J. D.; O'Connor, D. B.; Barbara, P. F. J. *Chem. Phys.* **2000**, *112*, 7811.

10. Karrai, K.; Groeber, R. D. *Appl. Phys. Lett.* **1995**, *66*, 1842.

11. Mei, E. H.; Higgins, D. A. *J. Chem. Phys.* **2000**, *112*, 7839.

12. Herndon, M. K.; Bradford, W. C.; Collins, R. T.; Hawkins, B. E.; Kuech, T. F.; Friedman, D. J.; Kurtz, S. R. *Appl. Phys. Lett.* **2000**, *77*, 100.

13. Huser, T.; Yan, M. *Synthetic Metals* **2001**, *116*, 333.

14. Sacristan, J.; Reinecke, H.; Mijangos, C.; Spells, S.; Yarwood, J. *Macromol. Chem. Phys.* **2002**, *203*, 678.

15. Bian, R. X.; Dunn, R. C.; Xie, X. S.; Leung, P. T. *Phys. Rev. Lett.* **1995**, *75*, 4772.

16. Friend, R. H.; Gymer, R. W.; Holmes, A. B.; Burroughes, J. H.; Marks, R. N.; Taliani, C.; Bradley, D. D. C.; Dos Santos, D. A.; Bredas, J. L.; Logdlund, M.; Salaneck, W. R. *Nature (London)* **1999**, *397*, 121.

17. Williamson, R. L.; Brereton, L. J.; Antognozzi, M.; Miles, M. J. *Ultramicroscopy* **1998**, *71*, 165.

18. Teetsov, J.; Vanden Bout, D. A. *Langmuir* **2002**, *18*, 897.

19. Betzig, E.; Trautman, J. K. *Science* **1992**, *257*, 189.

20. Hollars, C. W.; Dunn, R. C. *J. Chem. Phys.* **2000**, *112*, 7822.

21. Gottlich, H. S.; Stark, R. W.; Pedarnig, J. D.; Heckl, W. M. *Rev. Sci. Instrum.* **2000**, *71*, 3104.

22. Valaskovic, G. A.; Holton, M.; Morrison, G. H. *Appl. Opt.* **1995**, *34*, 1215.

Appendix A

NANOPERFORATED STANDARD SAMPLE FABRICATION

Metal standard samples are prepared by uniformly dispersing pink fluorescent latex nanospheres (182 nm diameter Polysciences) over a glass substrate in a surface concentration of approximately 0.25 nanospheres/ um^2. Dispersing the spheres is accomplished via the following method. A 10^{-3} aqueous dilution of the stock sphere solution is deposited on to a glass coverslip with an equal volume of aqueous Triton X-100 solution (~0.25 wt % in water). To ensure that the spheres do not appreciably form multisphere aggregates on the substrate surface, the solution is distributed equally over the glass substrate surface using a second microscope coverslip. Once the solution is uniformly distributed, and before the solution starts to dry, the liquid is completely scraped from the substarte surface using the second coverslip in a repeated squeegee motion. The slip is scraped until it appears to be a clean dry coverslip. By looking at the resulting coverslip under 50X high magnification using the Olympus microscope it is possible to see, for the most part, dispersed polymer spheres. Following sphere dispersal, a thin gold film (~20 nm thick) is vapor deposited over the combined substrate/sphere system. The polymer spheres are subsequently removed from the metal layer by briefly soaking the samples in solvent grade dichloromethane. Treatment with the common organic solvent ultimately yields a smooth nanoperforated metal film on a transparent glass support structure for NSOM tip characterization.

NSOM PROBE MOUNTING

After coating the fiber optic with aluminum and characterizing the tip aperture with a conventional microscope to ensure proper light throughput and the absence of pinholes, the fiber optic is ready to be affixed to a piezoelectric tuning fork. The tuning fork is a vital piece in the electronic feedback loop responsible for sufficient noncontact NSOM imaging. It is necessary to position the fiber in the groove on the metal bracket that connects the tuning fork to the small circuit chip. The tip apex should be then left to overhang the outer fork tine by a small amount. Once the fiber tips are positioned in the groove on the circuit board and on the oscillator tine it is necessary to adjust the tip overhang distance to 500 um using the calibrated eye piece divisions of the stereoscope. It is also imperative to ensure that the fiber rests against the fork tine and that it is not suspended above the tine surface. Once the tip is positioned the fiber is tacked in place using super glue at the end of the fork tine and at the intersection of the fiber and the first positioning groove. The adhesive is deposited at the end of the fork using a stripped fiber optic, while the glue can be applied to the groove much more generously using a coated fiber. The super glue should be bled off of the end of the application fiber slowly to ensure proper glue deposition. Once the super glue has been applied, the probe is allowed to dry under a 60 Watt light bulb for 30-45 minutes. Following the drying of the super glue, the two fiber/fork attachments are reinforced using temperature-cured epoxy (Torr-Seal Product# 9530001). The epoxy should be deposited directly over the superglue at the fork end and used to coat the entire fork bracket at the base of the circuit chip. At this stage, the

completed probe is temperature cured at 70 ^{o}C for at least two hours (preferably overnight) to adequately crosslink the epoxy and securely fasten the fiber to the quartz oscillator fork.

FIBER OPTIC PULLING

The Thor Labs fiber is used as received. The 40 um inner core optical fiber is stripped of the external protective polymer cladding using dichloromethane. After removal of ~3 inches of fiber cladding, the fiber is fastened into the two puller arms of the modified capillary pipette puller. The fiber is secured in the puller ensuring that the focused CO_2 laser spot will not hit the polymer cladding. This prevents burning of the cladding and the subsequent ablation of polymer material that will cause the laser optics to become coated with grime. If the fiber has been correctly loaded into the fiber puller, when the start button is pushed, the fiber will be heated and pulled within a two second delay. If the fiber has not been pulled after an additional two seconds, stop the pull and replace the fiber correctly in the fiber puller. As of this writing high throughput, small apex tips could be pulled using pulling program #70. The pulling parameters for this program are as follows and the pull time registered at the conclusion of the fiber pull should read 0.20 sec.

NSOM PROBE COATING

Tip coating was carried out in a high vacuum environment (10^{-6} torr) in a home built vacuum chamber equipped with a diffusion pump. The vacuum is necessary to reduce the partial pressure of oxygen available in the atmosphere, and prevent aluminum oxide formation. Aluminum oxide is more brittle than aluminum metal

and forms sites prone to pinholing in coated NSOM fibers. The best fibers are fabricated by tilting the tip rotors 34^{o} above the horizontal to prevent a proper shadow from the aluminum vapor source. The tips are subsequently rotated at ~120 RPM while aluminum is evaporated from below. The tip source separation is approximately 25 cm and provides adequate distance for unidirectional vapor deposition on to the exposed fibers. The metal is evaporated using a tungsten boat source. 99.999% aluminum was used and cleaned rigorously with acetone before being rolled into a small ball for placement in the tungsten boat. Resistive heating is incorporated to reach the 1800oC needed to vaporize the aluminum metal. Vapor is deposited as quickly as possible (~30 nm/sec) to yield a uniform, smooth aluminum coating with an 85 nm aperture exposed for the NSOM aperture.

CRYOSTAT WIRING DIAGRAM

The wiring diagram for the cryostat is provided here for future reference. All of the wiring leads have been identified and correlated to the different colored wires found in the cryostat cable. Caution must be taken when using the cryostat as the solid metal casing provides ample opportunity to short circuit any internal wiring. All of the leads should be checked with a multimeter to ensure that shorting through the case does not occur. One way to inadvertently short the leads of the cryostat wiring harness is to tighten the internal components too tightly. If the heater, or the thermocouple is tightened to severely it may cause a short through the insulating washers used to separate the circuits and cause great

confusion. All of the wiring information presented here is for a cryostat without any shorted leads but possessing good mechanical connections.

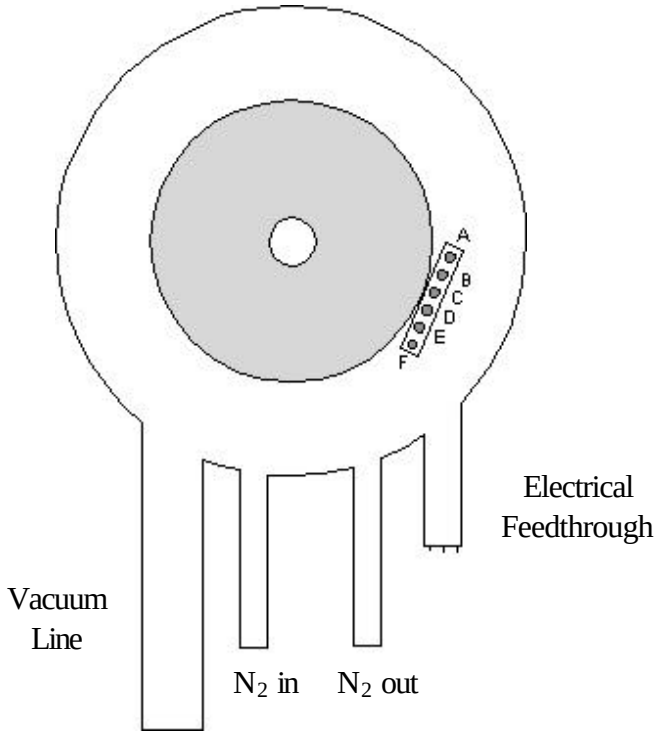

Figure A.1 Cryostat shown from the top view. Jumper posts used for internal wiring are labeled A-F.

The electrical connections to the cryostat feed through are connected to the jumper posts within the cryostat interior. Each individual electrical feedthrough is connected to a unique jumper post, making electrical work much easier.

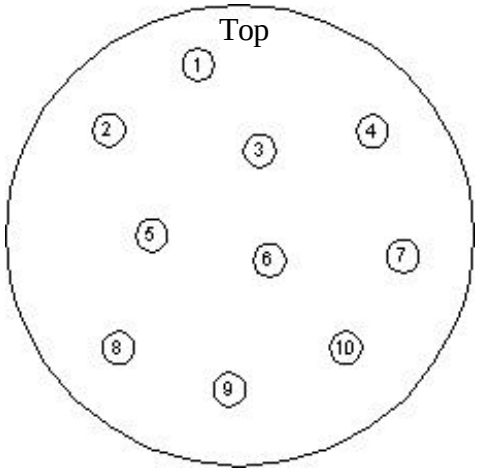

Figure A.2 Labeled cryostat wiring pins.

Each individual wiring pin is connected either to the jumper posts within the cryostat interior, or is used dedicated for thermocouple or heater operation. Below is the wiring key that designates each wiring pin on the electrical feedthrough to an interior jumper post.

Pin1→ Jumper Post E

Pin2→ Jumper Post F

Pin3→ Jumper Post D

Pin4→ Dedicated to thermocouple

Pin5→ Jumper Post C

Pin6→ Jumper Post B

Pin7→ Dedicated to thermocouple

Pin8→ Jumper Post A

Pin9→ Dedicated to heater

Pin10→ Dedicated to heater

Each wiring pin is, in turn, connected to a wire in the cryostat cable running to the control unit, or to a colored wire accessible for other external controls.

Pin1→ White

Pin2→ Black

Pin3→ Green

Pin4→ Control unit cable

Pin5→ Yellow

Pin6→ Blue

Pin7→ Control unit cable

Pin8→ Red

Pin9→ Control unit cable

Pin10→ Control unit cable

SANDWICH OLED FABRICATION

The information regarding ITO etching has been adapted from work conducted by Gage A. Brasher from 2001 to 2004 in the Vanden Bout research laboratory. With a glass substrate featuring an etched ITO electrode pattern, sandwich LED fabrication proceeds in a fairly straight forward manner. Following ITO etching in aqua regia solution, the resulting ITO-on-glass electrode pattern is further cleaned using an O_2 plasma cleaner for 5 min. The substrates are removed and placed directly in a methanol soak to prevent organic contamination on to the clean ITO surface. Immediately before fabricating and OLED, the ITO/glass substrate is removed from the methanol bath and dried in a

70^{o}C oven for 10 min. The chip is removed from the oven and ITO coated side of the substrate is identified by making a surface resistance measurement. The ITO coated surface should yield a short circuit using the digital multimeter. After identifying the correct side for LED fabrication, the chip is spin cast with 70 uL of the appropriate polymer solution (1 wt % MEHPPV in toluene or 0.5 wt% DPPE in chloroform) at 2000 RPM. The entire glass surface must be covered with polymer or the procedure must be restarted. Areas not cast will create short circuit regions during vapor deposition of the cathode. Following spin casting, the polymer films can be thermally annealed (or not) directly on the ITO coated glass surface. Next, the coated chips are placed face down on to a metal mask that will be used to create the correct shadow pattern of aluminum metal cathode structures to finish the LED sandwich. The pattern provides a matrix-addressable pattern of four LED structures per etched ITO substrate. Under high vacuum (~10^{-6} torr) the polymer surface of the substrates are coated with ~300 nm of aluminum via thermal vapor deposition. The metal is deposited as fast and as thoroughly as possible. Once the vapor deposition is complete the resulting LEDs can be removed from vacuum and connected to a voltage source. The positive terminal should be connected to the ITO electrode and the negative terminal connected, obviously, to the remaining aluminum cathode. If the device is connected in the wrong orientation, no light will be produced due to the diode behavior of the metal/poly/ITO junction.

POSITIVE RESIST PHOTOLITHOGRAPHY/GOLD ETCHING

Positive resist photolithography was carried out using equipment and clean-room space in the McDevitt Laboratory. The procedure for producing small structures on a gold/covered glass substrate is described step wise here. First it is necessary to have a gold-coated substrate on which to perform the lithography. A substrate is prepared through simple vapor deposition or plasma sputter coating. In particular, sputter coating appears to produce a gold film less prone to delamination than with vapor deposition. For this reason our samples are prepared using sputter coating. 100 nm of gold is applied to base-cleaned glass microscope slides at a deposition rate of ~1.0 nm/sec. Once the microscope slides are covered with gold, the substrates are cut into smaller pieces more easily handled for photolithography and more fitted to the dimensions of the given photo mask. Each individual substrate chip is subsequently cleared of residual dust using compressed air.

With the substrates prepared, each chip is spin cast (4000 RPM) with common positive exposure photoresist (Description of photoresist). The viscosity of the photoresist should be greater than that of water and two or three drops of solution should easily cast a substrate ? ” X 1” in area. The deposited photoresist is briefly cured on the chip using a drying oven (90^{o}C) for exactly 5 minutes. After initially curing the photoresist, the chosen photomask is placed securely over the chip substrate and clamped into place to prevent unwanted shadowing or movement of the photo mask. The photo mask/chip is then placed under an ultra violet exposure source (1000 W) for 10 minutes. At this point, the photo mask is

removed and the chip is briefly washed in photo resist developer solution for approximately 2 minutes; until the pattern of the photomask can be seen in the organic film left on the gold slide. When the pattern can be seen easily, the chip is removed from developer solution and rinsed with a distilled water wash. After rinsing, the chip is placed into a 120^{o}C oven for 5 minutes to hard-cure the remaining photo resist pattern. The chip is subsequently removed from the oven and allowed to cool to ambient temperature. Once the chip has returned to room temperature, it is submerged into concentrated KI solution. The chip is submerged with gentle agitation for 10-30 seconds to provide a gold pattern resembling that of the chosen photo mask. The chip is, again, rinsed with distilled water to remove the caustic etching solution and soaked in an acetone bath for 5 minutes to remove the remaining photo resist. At the completion of the procedure, the chip is left with a bare gold structure patterned using the desired gold photo mask.

USEFUL IGOR ROUTINES

Loading NSOM Images from SPM Software and Calculating Fluorescence Anisotropy

Macro for importing 200 x 200 pixel topographic images from SPM Software

```
macro importTOPO()
GBLoadWave/O/B/N=imaget/T={80,4}/S=3144/W=1 "G:"
Redimension/N=(200,200) imaget0
Display;AppendImage imaget0
Label bottom "x pixel"
Label left "y pixel"
end
```

Macro for importing 200 x 200 pixel images collected using detector 1 from SPM Software

```
macro importSNOMx()
GBLoadWave/O/B/N=imagex/T={80,4}/S=3144/W=1 "G:"
Redimension/N=(200,200) imagex0
Display;AppendImage imagex0
Label bottom "x pixel"
Label left "y pixel"
end
```

Macro for importing 200 x 200 pixel images collected using detector 2 from SPM Software

```
macro importSNOMy()
GBLoadWave/O/B/N=imagey/T={80,4}/S=3144/W=1 "G:"
Redimension/N=(200,200) imagey0
Display;AppendImage imagey0
Label bottom "x pixel"
Label left "y pixel"
end
```

Macro for calculating fluorescence anisotropy images after loading data from detector1 and detector 2

```
macro anis otropy()
wavestats imagex0
print V_avg
variable n
n=V_avg
wavestats imagey0
print V_avg
variable m
m=V_avg
variable q
q=n/m
print q
make/O/N=(200,200) imageynew
imageynew=imagey0*q
histogram imagex0,histogramx
histogram imageynew,histogramy
display histogramx,histogramy
ModifyGraph rgb(histogramx)=(0,0,52224)
make/O/N=(200,200) imagesum
imagesum=imagex0+imageynew
make/O/N=(200,200) imagedif
imagedif=imagex0-imageynew
make/O/N=(200,200) imageanis
imageanis=imagedif/imagesum
Display;AppendImage imageanis
ColorScale/C/N=text0 image=imageanis,lowTrip=0.001
```

```
ModifyGraph margin(left)=108
ColorScale/C/N=text0/F=0/S=1/D=0.1/A=MC side=2,image=imageanis
wavestats imageanis
print "sigma="
print V_sdev
Setscale x,V_min,V_max,M_Colors
ModifyImage imageanis cindex= M_colors
make/O/N=50 histogramanis
histogram imageanis,histogramanis
display histogramanis
ModifyGraph mode=5,toMode=1
End
```

Importing and Fitting Data from TCSPC Module

Loading TCSPC Data Collected on CNM Instrument

```
GBLoadWave/O/B/N=topo0116/T={2,80}/S=3144/W=1 "datafile.spc"
```

Single Exponential Fit

```
Function singlexp(w,x) : FitFunc
Wave w
Variable x
//CurveFitDialog/ These comments were created by the Curve Fitting dialog. Altering them will
//CurveFitDialog/ make the function less convenient to work with in the Curve Fitting dialog.
//CurveFitDialog/ Equation:
//CurveFitDialog/ f(x) = B+A1*e^(-(x)/t1)
//CurveFitDialog/ End of Equation
//CurveFitDialog/ Independent Variables 1
//CurveFitDialog/ x
//CurveFitDialog/ Coefficients 3
//CurveFitDialog/ w[0] = B
//CurveFitDialog/ w[1] = A1
//CurveFitDialog/ w[2] = t1
return w[0]+w[1]*e^(-(x)/w[2])
End
```

Double Exponential Fit

```
Function dbleexp(w,x) : FitFunc
Wave w
Variable x
//CurveFitDialog/ These comments were created by the Curve Fitting dialog. Altering them will
//CurveFitDialog/ make the function less convenient to work with in the Curve Fitting dialog.
//CurveFitDialog/ Equation:
//CurveFitDialog/ f(x) = B+A1*e^((-(x)/t1))+A2*e^((-(x)/t2))
//CurveFitDialog/ End of Equation
//CurveFitDialog/ Independent Variables 1
```

```
//CurveFitDialog/ x
//CurveFitDialog/ Coefficients 5
//CurveFitDialog/ w[0] = B
//CurveFitDialog/ w[1] = A1
//CurveFitDialog/ w[2] = t1
//CurveFitDialog/ w[3] = A2
//CurveFitDialog/ w[4] = t2
return w[0]+w[1]*e^((-(x)/w[2]))+w[3]*e^((-(x)/w[4]))
End
```

Triple Exponential Fit

```
Function tripleexp(w,x) : FitFunc
Wave w
Variable x
//CurveFitDialog/ These comments were created by the Curve Fitting dialog. Altering them will
//CurveFitDialog/ make the function less convenient to work with in the Curve Fitting dialog.
//CurveFitDialog/ Equation:
//CurveFitDialog/ f(x) = B+A1*e^((-(x)/t1))+A2*e^((-(x)/t2))+A3*e^((-(x)/t3))
//CurveFitDialog/ End of Equation
//CurveFitDialog/ Independent Variables 1
//CurveFitDialog/ x
//CurveFitDialog/ Coefficients 7
//CurveFitDialog/ w[0] = B
//CurveFitDialog/ w[1] = A1
//CurveFitDialog/ w[2] = t1
//CurveFitDialog/ w[3] = A2
//CurveFitDialog/ w[4] = t2
//CurveFitDialog/ w[5] = A3
//CurveFitDialog/ w[6] = t3
return w[0]+w[1]*e^((-(x)/w[2]))+w[3]*e^((-(x)/w[4]))+w[5]*e^((-(x)/w[6]))
End
```

Fluorescence Lifetime Imaging (FLI) NSOM Protocol

Constructs Total Fluorescence Image

```
//makes total intensity image from set of 1D linear lifetime data (slow)
macro FluorTotal1D(numberofpixels,pointsindecay)    //input # of pixels in image and # of points
in decay
variable numberofpixels                                    //sets # of pixels in NSOM scan
variable i=0
variable pointsindecay                          //sets # of points in time window for decay
print time()
Make/O/N=40000 sum1D
do
sum1D[i]=sum (masterwave,45+pointsindecay*i,pointsindecay*(i+1))    //sums counts in a given
time window
i+=1
```

```
while(i<numberofpixels)
redimension/N=(200,200) sum1D
print "done   "+time()
beep
end
```

Constructs Partial Intensity Image After Selected Time

```
//makes partial intensity image from set of 1D linear lifetime data (slow)
macro FluorPart1D(numberofpixels,pointsindecay)      //input # of pixels in image and # of points
in decay
variable numberofpixels                                    //sets # of pixels in NSOM scan
variable i=0
variable pointsindecay                          //sets # of points in time window for decay
print time()
Make/O/N=40000 part1D
do
part1D[i]=sum (masterwave,90+pointsindecay*i,pointsindecay*(i+1))     //sums counts in a given
time window after a delay time T
i+=1
while(i<numberofpixels)
redimension/N=(200,200) part1D
print "done   "+time()
beep
end
```

Constructs Intesity Image From One Time Point at Each Pixel

```
//makes total intensity image at a specified time from set of 1D linear data (slow)
macro DelayTime1D(numberofpixels,pointsindecay, timepoint)
variable timepoint
variable numberofpixels                                    // sets # of pixels in NSOM scan
variable i=0
variable pointsindecay                          //sets # of points in time window for decay
Make/O/N=40000 timesum1D
print time()
do
timesum1D[i]=sum (masterwave,timepoint+pointsindecay*i,pointsindecay*(i+1))
//sums counts at a specific time
i+=1
while(i<numberofpixels)
print "done   "+time()
beep
end
```

Constructs Fluorescence Image after Selected Time

```
//uses 1D linear masterwave to create a fluorescence image at every time (t) (really slow)
macro FluoImageTime1D(numberofpixels,pointsindecay)
variable t=0
variable numberofpixels                                    //sets # of pixels in NSOM scan
```

```
variable i=0
variable pointsindecay                    //sets # of points in time window for decay
string str1
string str2
print time()
do
i=0
str1="time"                                          //names sequential waves
str2=num2str(t)
Make/O/N=40000 $str1+str2
do
$str1+str2[i]=masterwave[(pointsindecay*i)+t]        //makes linear wave with counts at time t at
each point
i+=1
while(i<numberofpixels)
redimension/N=(200,200) $str1+str2                   //redimensions wave to 2D image
t+=1                                                          //goes to next t value
while(t<pointsindecay)
print "done   "+time()
beep
end
```

Redimensions 1D data to 3D and Calculates Fluorescence Decay at Every Point

```
//3D data cube is used to build a fluorescence decay at every NSOM pixel
Average lifetime of chosen area is also calculated
macro AvgDecayTime3D(startx,starty,endx,endy, rowlength)
variable startx                                      //sets start coordinate of lower left corner for
rectangular area
variable starty
variable endx                                        //sets end coordinate of upper right
corner for rectangular area
variable endy
variable rowlength                                   //sets width of rectangular box
string str1
str1="pixel"
string str2
str2="("
string str3
string str4
str4=","
string str5
string str6
str6=")"
Make/O/N=276 avg=0
display avg
print time()
do
do
str5=num2str(starty)
str3=num2str(startx)
```

```
Duplicate/O/R=[0,277][startx,startx][starty,starty] masterwave, $str1+str2+str3+str4+str5+str6
//creates wave and cuts 3D cube into pixel chunks
startx+=1                                                    //goes to next x value
redimension/N=(-1,0) $str1+str2+str3+str4+str5+str6          //redimensions matrix as a 1D wave
avg=avg+$str1+str2+str3+str4+str5+str6                       //sums decays at
evry point in specified area
Killwaves $str1+str2+str3+str4+str5+str6
while(startx<endx)
startx=endx-rowlength
starty+=1                                                    //goes to next row up
print starty
while(starty<endy)
wavestats/q avg
        //normalizes summed decays
avg=avg/V_max
print "done   "+time()
beep
end
```

Creates Averaged Fluorescence Decay in Each Column

```
//creates a group of waves representing the sum of all specified column y values for each x from
3D data cube
macro ColumnAvg3D(startx,starty,endx,endy,rowlength)
variable startx                                              //sets start coordinate of lower left
corner for rectangular area
variable starty
variable endx                                                //sets start coordinate of
upper right corner for rectangular area
variable endy
variable rowlength                                           //specifies column height
string str1
str1="pixel"
string str2
str2="("
string str3
string str4
str4=","
string str5
string str6
str6=")"
string str7
str7="colavg"
print time()
do
str3=num2str(startx)                                         //creates wave called 'colavgx'
Make/O/N=332 $str7+str3
do
str5=num2str(starty)
Duplicate/O/R=[0,332][startx,startx][starty,starty] masterwave, $str1+str2+str3+str4+str5+str6
```

```
$str7+str3=($str7+str3)+($str1+str2+str3+str4+str5+str6)          //sums each y value in the
column
starty+=1
while (starty<endy)
startx+=1
starty=starty-rowlength
while (startx<endx)
print "done   "+time()
beep
end
```

Calculates Average Fluorescence Decay for Select Region

```
//sums total fluorescence counts for averaged column decays
macro TotalLineCounts(startx,endx)                    //designates start and end of line scan
variable i=0
variable startx
variable endx
variable pointsindecay=332                            //# of points in decay to be added
string str1
string str2
string str3
str3="colavg"
Make/O/N=200 wavetotal
do
str1=num2str(i)
wavetotal[i]=sum ($str3+str1,79,332)                  //Makes wave where y values represent total
emitted photons in time window
i+=1
while(i<endx)
display wavetotal
end
```

Calculates Denominator for Fluorescence Lifetime Calculation

```
//takes specified portion of decay to use as denominator in lifetime calculation
macro PartialLineCounts(startx,endx)
variable i=0
variable startx
variable endx
variable pointsindecay=332
string str1
string str2
string str3
str3="colavg"
Make/O/N=200 wavenumerator
do
str1=num2str(i)
wavenumerator[i]=sum ($str3+str1,100,332)  //sums counts from a fluorescence delay time to the
end of the decay
i+=1
```

```
while(i<endx)
display wavenumerator
end
```

Creates Linescan of Fluorescence Lifetimes Across the Horizontal

```
//Creates lifetime line scan for averaged horizontal area
macro LifeTimeLineScan()
Make/O/N=200 lifetimewave
lifetimewave=-4/(ln(wavenumerator/wavetotal))  //must input cutoff T
display lifetimewave
end
```

Vita

Joseph Michael Imhof was born in Mt. Vernon, WA on July 17, 1977 to Joseph M. and Lynn E. Imhof. As a child he moved with his mother, step-father, and sister throughout western Washington State and attended many elementary schools. In 1991 he moved with his family to Edison, WA. He later graduated from Burlington-Edison High School as a presidential scholar in 1995 and received numerous academic awards in chemistry, calculus, English, and history. Joseph graduated Cum Laude from Gonzaga University in Spokane, WA in 1999 and was awarded the Outstanding Senior Chemistry Student Award. Upon completion of his undergraduate degree, he moved to Austin, TX to persue a doctoral degree in chemistry at the University of Texas. He was married in October of 2003 to Jerri Lea Trahan and they make their permanent home in Austin.

Permanent address: 2209 Hancock Drive #30, Austin, TX 78756

This dissertation was typed by Joseph M. Imhof.